Holographic interferometry and its application in visualizing particle movements in continuous flow

A thesis presented

by

Stian Magnussen

to

The Department of Physics and Technology

in partial fulfilment of the requirements

for the degree of

Candidatus Scientiarum

in Applied Optics

UNIVERSITY OF BERGEN

Norway

October 2004

Abstract

This thesis presents the work performed at the Department of Physics and Technology at the University of Bergen during a collaborative project funded by Statoil. The parties in this collaboration were the University of Bergen, Rogaland Research (RF) and the University College of Stavanger The overall project objective was to visualize and quantify particle motion in continuous flow.

At the Department of Physics and Technology we have built a closed-loop tank system consisting of three glass tanks. These tanks were positioned at different heights to provide the required pressure. The fluid streamed from an upper reservoir through an inspection tank and to a lower reservoir. The tanks were interconnected by Teflon coated pipes to enable the use of a fluid consisting of two chemical solvents. The fluid was designed to match the refractive index of a selection of 2 mm glass particles at a specific wavelength to improve our investigation possibilities. This index matching enabled marked particles to be identified inside an almost invisible moving mass.

Holography is proposed as a new way of investigating the lower, slow moving, particle layers in sand dune transportation. Our thesis constitutes the theoretical background for holography and its more advanced interferometric techniques. We compare available double exposure theories with experimental holography for objects with various static movements.

We later advance to a more dynamic optical system. The study of a holographic recording medium called Bacteriorhodopsin is presented. A continuous observation of a changing object has never been tested at our Optics Group at the Department of Physics and Technology before. We introduce real time holography using a Bacteriorhodopsin film and perform holography with continuous flow in the tank system.

Faced with mechanical instabilities in the tank system, we found that the optical technique was too sensitive to these, and therefore not the most suitable method for examining particles in continuous flow in the built tank system. However, in general the real time holographic technique documented in this thesis is very promising and can readily be applied in numerous scientific areas.

i

Acknowledgements

Stian Magnussen
October the 1st, 2004

Contents:

1 Introduction

1.1 Introduction to the project

The purpose of this project is modelling of solid liquid flow in pipes and channels. An essential part is development of flow loops and experimental techniques. The project is a collaborative between the University of Bergen, Rogaland Research (RF), the University College of Stavanger and Statoil. A very important issue will be development of measurement techniques and visualization. Petroleum problems ranging from reservoir sedimentation to slurry transport in pipes may be studied, with the interaction of fluid and particles as the guiding issue. This work will focus on developing new experimental techniques and experiments that may widen the understanding of liquid and solid flow.

Two different flow loops will be built. At the University of Bergen we will build a closed, pressure driven flow loop with a rectangular, transparent tank to study the interaction of fluid and particles. We will focus on visualization of particle motion in an index-matched fluid. The motivation for the experimental work is a desire to visualize sand and residue particles and their movement inside pipes. A Ph.D student at the University College of Stavanger will build a larger circular tank for investigation of open flow.

The work performed at the University of Bergen would be a feasibility study, which other students and researchers involved in the project could benefit from. The closed tank system would be made at the engineering workshop at the Department of Physics and Technology following ideas of Dr. J. Petersen from RF, who acted as an external supervisor for both students involved on the project. The tank rig would later be transported to the University College of Stavanger for further studies of fluid-particle interactions.

Rogaland research is "an independent research institute with research and research related activities within Petroleum, Aquatic Environment, Social Science and Business Development" [http://www.rf.no, 27.02.04].

Oil companies work intensively to achieve higher recovery factors from their oil and gas fields. Success depends on the drilling systems ability to adequately remove residue particles from the hole [http://www.undergroundinfo.com/uceditorialarchive/June04/june04particles.pdf, 21.08.04]. Sand particles are normally separated along with water at the oil platforms in large separation tanks. Before reaching the separation system the sedimentary particles wear and tear inside the oil well, pipes and at the valves. If they are let to consolidate they will block parts of the flow [http://www.ipt.ntnu.no/~jsg/studenter/prosjekt/1995/henriksen.txt, 21.08.04]. We believe that large savings could be made by finding better techniques to remove these residues from the pipe systems. To do so, we need a better understanding on how residues are transported.

Granular flow can be modelled numerically. A two layer approach assumes a presence of a dense grain bed and a heterogeneous bed. A three layer model assumes a lower stationary bed, a moving bed and a heterogeneous bed [Rivkin and Shreiber 1999]. We will not examine these specific models but expect the upper layers to move according to sand dune transportation where particles slip into the flow when this is

strong enough to overcome friction and gravity. The student involved in process technology will study the transportation of these upper layers. The objective of his work is to guide the workshop in building the tank system and to use a high-speed digital video camera to monitor the fast moving particles [Lie, in preparation].

There exist little experimental information about the lower layers in particle transportation. Holographic techniques have been a major field of study at the Optics Group at the University of Bergen. This is a visualization technique that could help revealing more about the nature of the lower residue layers. These layers can be stationary or slowly moving, with so far unknown deflection or velocity. The optics student will study holography and how this technique can be used to visualize the particle mass in its three-dimensional form. In particular, slow movements will be of interest.

At the initiation of the project we expected that a few months would be needed to build and rig the tank system. We will use this time to study holography. Techniques using double exposure holography are of especially interest. These are expected to be the most promising holographic methods to detect small changes in or near an object. The project description stated that no complete analysis of the particle-fluid experiments was to be performed. The most important motivation was the detection of changes and an evaluation on whether holography is a suitable approach to the problem.

1.2 Introduction to Holography

Holography is a technique employed to make three-dimensional images. The size of the object can range from large cars to small particles on the micrometer scale. Holograms have a fascinating feature, called *parallax*, which allows the viewer to observe the virtual object from different perspectives in full 3D.

Holography originates from the work of the British/Hungarian researcher Dr. D. Gabor. He tried to improve the resolution of his electron microscope in 1947. Using a mercury arc lamp, the non-coherent light source resulted in distortions in his images. These images he called holograms after the Greek words "holos" meaning "whole" and "gamma" meaning "message". He realized that his images contained more information than a normal photograph, but also that his discoveries had taken place before the necessary technological equipment had been made. He tried to make his light source coherent by sending the light both through a pinhole and colour filters, but the quality of his first holograms were poor (http://www.holophile.com/history.htm, 18.04.04).

Lacking a proper coherent light source, the interest for holography faded until the invention of the laser by Dr. T.H. Maiman in 1960. The monochromatic (one wavelength) and coherent (light in phase) output from the laser made it possible to produce distortion free holograms of high quality. A new era erupted and the next ten years was the golden years of holography. New techniques and fields of applications were discovered. Full colour holograms were made in 1979 (http://www.holophile.com/about.htm, 18.04.04), which made the virtual images more real to the human eyes. Improved laser and film technology have made the technique generally available. Today it is possible to record your own holography at home by

buying a low cost laser diode and ordering a few holographic films on the World Wide Web (http://www.slavich.com, 20.04.04).

Technological applications that have been developed since the beginning include:

- Holography can be used with X-Rays, to form three dimensional images of both bones and organs (http://www.hololight.net/medical.html, 22.04.04).
- Holographic Data Storage (HDS), are techniques to store extremely large amount of data on small areas. "With HDS, you can store the entire contents of the Library of Congress in the area the size of a sugar cube." (http://www.holoworld.com/holo/quest6.html, 18.04.04).
- Non-destructive (no contact) testing of airplanes and cars can be accomplished by double exposure techniques, enabling the producer to find weak spots in their constructions.
- Pulse lasers can be used to make images of shock waves around a bullet in flight and other fast moving objects as illustrated in Figure 1.
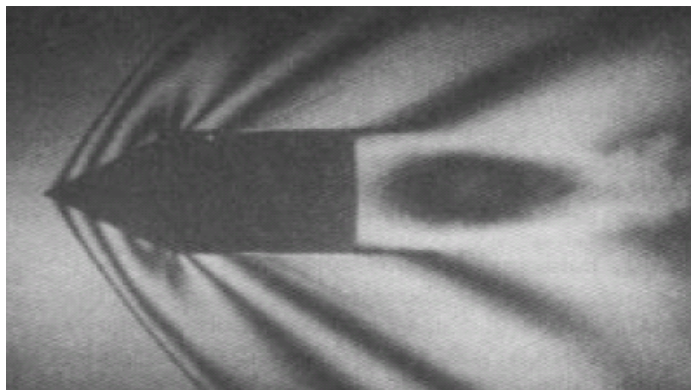
Figure 1 Double exposure hologram of bullet in flight, using a pulsar Q-switched ruby laser. Copied from (http://www.ph.ed.ac.uk/~wjh/teaching/mo/slides/holo-interferometry/holo-inter.pdf, 20.04.04).

- Holographic lenses are used in an aircraft "heads-up display". This allows a fighter pilot to see critical cockpit instruments while he looks straight through the windscreen. These systems will also appear in automobiles as similar systems are being researched (http://www.holophile.com/history.htm, 18.04.04).
- "Researchers at the University of Alabama in Huntsville are developing the sub- systems of a computerized holographic display. While the work focuses on providing control panels for remote driving, training simulators and command and control presentations, researchers believe that TV sets with 3-D images might be available for as little as $5,000 within the next ten years." (http://www.holophile.com/history.htm, 18.04.04).

Even artists have enjoyed the possibility that enable them to make live portraits of people and animals, not to mention the various "rainbow" holograms on today's Visa and Master cards. Today, more than 40 years later, holography is still finding new applications.

Figure 2 Portrait of Dizzy Gillespie, from (http://www.holo.com/gaz/dizzy.html, 21.04.04).

2 Theoretical background

2.1 Hologram Classification

There are a few characteristics, which are used to classify different types of holograms. These classifications are determined by the *recording geometry* (optical set-up), on how the reconstruction beam is *modulated* to diffract the image and it depends on the *thickness* of the holographic emulsion.

2.1.1 Recording geometry

The recording geometry decides whether the hologram will be classified as a transmission or a reflection hologram. If the two interfering waves (object and a reference beam) illuminate the emulsion from each side of the film, it is classified as a Lippman or reflection hologram. They are also called "white light" holograms, as they can be observed under ordinary white light conditions. These holograms should be seen as a light reflection from the film plate. It has its name due to the reflection of light from the film. The other type is called transmission hologram. The two recording waves illuminate the film from the same side, and due to the recorded structure in the emulsion these holograms must be viewed with a coherent light source (laser). To view the hologram, the reconstruction light source must illuminate the film from the opposite side of the observer, hence the illumination light will travel through the emulsion and recreate the object (and therefore its name). The geometrical set-up also determines whether the hologram is a Leith-Upatnieks (the first to use this technique) "off-axis" hologram or a Gabor "in-line" hologram. The difference between them are self-evident, as the in-line hologram use ~ 0° between the two interfering waves, and the off-axis holograms are all other recording geometries that use angles between the two interfering waves different from 0°. The last classification due to the recording geometry is a consequence of the curvature of the interfering wavefronts at the hologram plane. The curvature of the waves at the hologram, define where the minimas and maximas of the fringe pattern in the emulsion are created. The distance from object to film and the possible optical elements positioned between film and object, partly determine the name the respective recording receives. The different types are called "Image", "Fraunhofer", "Fresnel" and "Fourier" holograms. The recording geometry for the different holograms is shown in Figure 3.
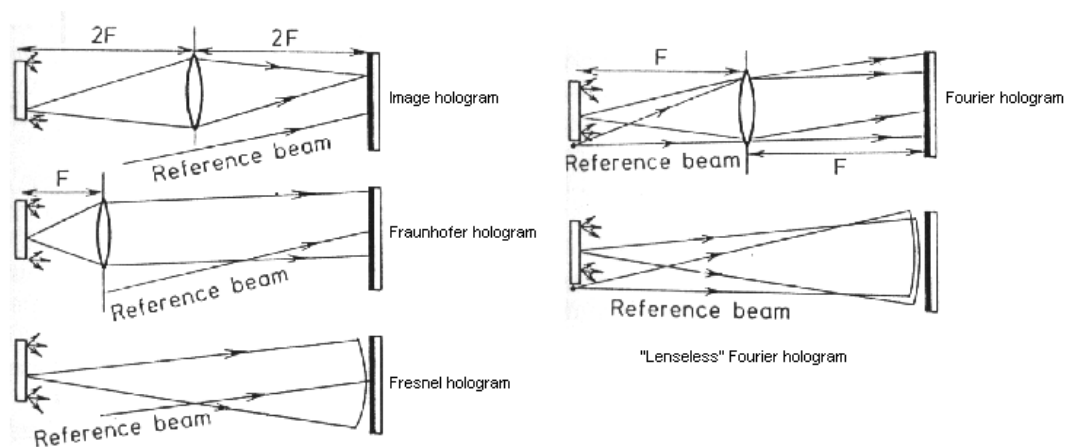
Figure 3 Holographic Recording Geometries, figure copied from Ostrvsky et al [1990]. 'F' represents the lens focal distance.

A hologram recorded at an infinite distance from the object (Fraunhofer diffraction region) or projected to be at an infinite distance (using a lens), is called a *Fraunhofer hologram*. The object wave is evolving as parallel light onto the holographic film. The far-field condition is fulfilled if the distance from the photographic plate to the object is large compared to the dimensions of the object, given by:

$$z_O >> \frac{\left(x_O^2 + y_O^2\right)}{\lambda}$$

(2-1)

Here x_o and y_o, represent the two dimensions of the surface of the object.

The common *Fresnel hologram* is formed when the object is in the near-field diffraction region. Generally, the field at the hologram plane is the Fresnel diffraction pattern if the object is reasonably close to the recording medium. Smith [1977] indicates this distance to be typically 10 times the object diameter or less from the film. If both waves lie at infinity, or have the same curvature of the wave front (lensless *Fourier hologram*), the complex amplitude of the waves at the hologram plane, are the Fourier transform of the original object and reference wave. This normally restricts the object to be of limited size or in a single plane. The *Fourier holograms* are usually produced, by placing the object and the spherical reference wave at the focal plane of a lens.

2.1.2 Modulation of the incident beam

The second classification of holograms depends on how the illuminated hologram modulates the diffracted beam that reconstructs the object. This classification reveals how the incident light is directed and modulated to form the virtual (or the real) image of the object. Holograms are put in two categories (dichotomized). The created structure within the emulsion can be a variation of the index of refraction (*phase recording*), or a variation of the medium's density/opacity (*amplitude recording*), or even both. In phase modulation materials, the refractive index is modulated throughout the emulsion due to the two interfering waves. After developing, a pure phase modulated material does not absorb any of the incident light and produce very bright images. The illumination wave is forming the virtual and real object image as a result of how different light rays are refracted through the emulsion. In the amplitude modulating materials the absorption constant changes as a result of the exposed light (exposure being 'I*t', intensity multiplied with time). On reconstruction, the film absorbs a considerable amount of the light, reducing the efficiency of the image. Many holographic materials can be transformed from a developed amplitude hologram to a phase hologram by a chemical bleaching procedure. The bleaching chemicals and the procedure is often different for each particular film.

2.1.3 Thickness of the film medium

There are thin and thick (volume) holograms, a classification that depends on the average spacing of interference fringes in the hologram to its thickness d. A Q parameter is used to separate the two regimes. If this parameter is larger than one for a specific film, it is considered to be a volume hologram. If it is less, then it corresponds to a thin hologram. These criteria are not always adequate, but see Hariaharan [1996] for more detail on this topic. The Q parameter is defined by equation (2-2):

$$Q = \frac{2\pi\lambda_O d}{n_O \Lambda^2}$$ (2-2)

where:
λ_o is the recording wavelength
d is thickness of the emulsion
n_o is the refractive index of the emulsion
Λ is the grating period (number of fringes per length)

The major difference between the two emulsion types is the depth of the reconstructed image. Very thin holograms (such as rainbow holograms on credit card) will provide little depth, while a thick hologram recreate the object with greater depth.

2.2 Holographic films

The most important properties of holographic materials are sensitivity, diffraction efficiency (modulation capability) and recyclability. The film should ideally be sensitive at all wavelengths of the electromagnetic spectrum to render recording by any light source. Such a material has yet not been made. Standard holographic films like Silver halide and Dichromatic gelatine has some but not all of these qualities. Silver halide materials can be made extremely light sensitive and dichromatic gelatine can obtain extreme diffraction efficiency, but neither of the films can be recycled nor sensitized at every wavelength (although the visible light spectrum can be covered with pan-chromatic film). Sensitivity and resolving power will be a trade-off with all films, as both depend on the photosensitive grain size in the emulsion (discussed in the next section). Another problem working with holography is that not all the different types of emulsion are commercialised. For our project, a few commercialised films were considered. These were; silver halide, dichromatic gelatin, thermoplastic and Bacteriorhodopsin film plates.

2.2.1 Silver-Halide in gelatin

Silver halide materials have been used for a hundred years. It is used in ordinary photographic as well as in holographic films to record all types of radiation. Photographers and holographers have more practical experience with this material than any other. The principal property that distinguishes a hologram from a conventional photograph is not to be found in the emulsion, but in the recording process. A hologram uses both the phase and amplitude information of the interfering light when two waves interfere in the emulsion. The key feature of the laser is the coherent light it emits, which makes it possible to record the phase of light, confer Kasap [2001] for more information on how a laser works.

Silver halide materials are versatile, commercially available in numerous sizes and qualities and they can be handled and processed with a minimum of equipment. These films are suitable for making both amplitude and phase holograms (not a mix of both, however), and possess a sensitivity unequalled by any other material. A typical peak sensitivity of a film from Slavich (type PFG-01 pr.2004-03-29) is 80μJ/cm^2 (this film has 3000 lines/mm). This film requires wet processing, which is a major drawback. This limits its practical applications to standard holography, frozen fringe and average-time holography. These techniques will be explained in greater detail in section 2.4. The most interesting technique to use on the tank project is real-time holography. This is a technique used to compare a hologram with the live object. The

problem with real-time holography using this film is the requirement for special developing equipment for in situ processing or extremely accurate re-positioning tools. A few μm displacement of the film from its original position would rule out the possibility of achieving interference patterns from the two objects (one live and one recorded). As the equipment would have taken a long time to complete, it was not investigated any further. Deelen & Nisenson [1969] have reported good results using in-situ equipment.

A Silver halide emulsion consists of microscopic crystals of silver halides, predominantly silver bromide (AgBr), encapsulated in gelatine. The index of refraction of gelatine is about 1.5, while AgBr is around 2.25.

In order to decrease scattering from the embedded crystals, the particles must be made much smaller than the wavelength of light (Rayleigh theory of scattering becomes applicable). Typical values of grain size in the emulsions intended for holographic use are in the order of 0.03 – 0.08 μm [Biedermann 1977]. Emulsions with larger grains yield the highest sensitivity, but have less spatial efficiency (resolution). Films made of small silver halide grains provide better spatial efficiency, but will lack some sensitivity and will require a longer exposure time. This will be a trade off between the film speed and the resolution.

During exposure, the absorption of a photon by a grain in the emulsion can free an electron in the following reaction:

$$Br^- + h\nu \rightarrow Br + e^-$$ (2-3)

This free electron can move through the crystal lattice. At one of the crystal imperfections, which have to be distributed suitably through the emulsion, it is trapped and attracts an interstitial silver ion, occupying holes between the larger metal atoms or ions in the crystal lattice:

$$e^- + Ag^+ \rightarrow Ag$$ (2-4)

Lifetime of this single silver atom is about 1 – 2s, but it will trap another liberated electron and keep increasing, repeating the process if offered more electrons during its lifetime. A larger silver speck of two or more atoms is stable, but to make a latent image it has to be a speck of at least three or four atoms. These silver specks are often referred to as the latent image, because they can be converted into a hologram by wet processing. Processing techniques using Silver halide recording materials are described in more detail by Singstad [1996].

Most commercial silver halide emulsions have a typical spatial frequency (resolving power) around 3000 - 5000 lines/mm, depending on sensitivity region. Agfa-Gevaert, which has been the largest manufacturer, has stopped producing their quality 8E75HD, which had about 5000 lines/mm with peak sensitivity in the red region. Eastman Kodak still produces their BB-640 (sensitivity region 580-650nm), which has the same spatial resolution, while Slavich produce PFG-03M (ultra-fine grain), which has more than 5000 lines/mm at spectral sensitivity range 600-680nm (2003). Silver halide films are produced both in selected sensitivity ranges and as pan chromatic plates (full visible spectrum). Good quality holograms have been made using products from all the three film producers, at the Department of Physics and Technology during the last years.

2.2.2 Dichromated gelatin (DCG)

Dichromatic gelatin and other dichromatic colloids are among the oldest photographic materials. Many different colloids have been used to make photosensitive layers; albumen, sodium, fish glue etc. Dichromated gelatin is an important holographic material due to its almost ideal properties for phase holograms. It record information either as variation of index of refraction or as a thickness variation, or as a combination of the two. The main reason that DCG have not been widely used, despite their promise, are the difficulty of obtaining reproducible results and problems related to the distortion of the photosensitive layer from exposure to developed image [Meyerhofer1977].

A colloid is defined as "a substance that consists of particles dispersed throughout another substance" [http://www.meriamwebster.com, 29.03.04].

This material can produce holograms with diffraction efficiency at almost the theoretical limit [Meyerhofer 1977]. It has low noise and good image quality. It has been one of the best materials to make holographic optical elements, like gratings and lenses. A disadvantage is the low sensitivity, which creates a need for a powerful light source. Currently Slavich offers DCG films designed to make phase recordings with a resolving power of more than 5000 lines/mm (2004-03-25). The sensitivity of the same material is between 100-250mJ/cm^2. This is $\sim 10^3$ times less sensitive than the silver halide materials.

DCG materials are unknown to us and have not been available at the Department of Physics and Technology. We did not apprehend any of these films for further testing, as they offered no new functionality compared to the silver halide films we already had.

2.2.3 Thermoplastic Recording

Due to the project objective of visualizing moving particle layers, a new material might be needed. The speed of the particles would probably exclude the normal holographic recording materials due to their required exposure times of several seconds (typically). Silver halide films presently lack the equipment to test real-time holography, which might be a better way to achieve information of moving particles. A normal hologram of an object in continuous motion will appear blurry and provide no qualitative results. Velocity and movement direction will not be possible to determine. However, if we could get a holographic recording material that enabled us to continuously monitor the changes, this would improve the holographic approach to the problem.

Thermoplastic (or "Photothermo-plastic") is a material that is recyclable, and which requires no wet processing. It is reasonable sensitive across the entire visible spectrum and can yield a fairly high diffraction efficiency. The film surface needs to be sensitized to light by applying a high voltage prior to exposure, as shown in Figure 4. This should be performed with a "corona device" which spray positive ions across the surface of the film. The film is now sensitized and all exposed light will change these charge carriers on the surface. An exposure to light will generate charge carriers in the photoconductor layer, and these will migrate to the oppositely charged carriers and neutralized these. This will reduce the surface potential. Another strong recharging of the film, additional charges are deposited wherever the exposure had resulted in a migration of charge resulting in a spatially varying electric field pattern. This

represents a latent image. The thermoplastic can now be heated near its softening temperature using a current passing through the material. This will deform the thermoplastic layer according to the electric field. It will be thicker in all unexposed areas and thinner in the illuminated areas. After cooling the film is relatively stable and is not further affected by light. The film can be heated again and illuminated by white light to erase all prior recordings.

Step 1

First charging

$+++++++++++++++++$ ← Thermoplastic

← Photoconductor

$-----------------$

Step 2

Exposure

$+++++++++++++++++$

$-$ $-----------$

$-------$

Step 3

Second charging

$+++++++$ $+$

$++++++++++++++++$

$-----------------$

Step 4

Development

Step 5

Erasure
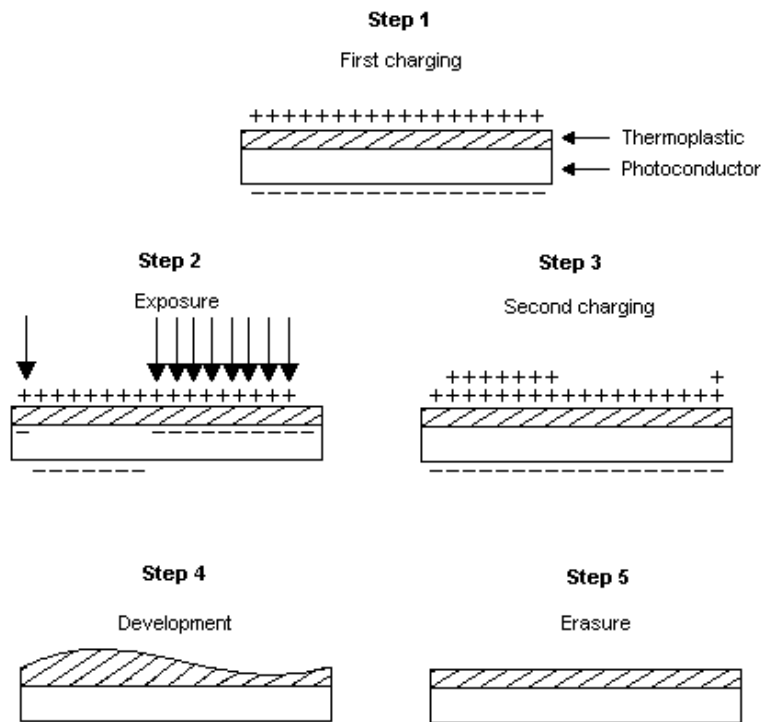
Figure 4 Record-erase cycle for photothermoplastic recording material [Lin & Beauchamp 1970].

According to Hariharan [1996] commercial Thermoplastics have a life time of more than 300 cycles but others [Urbach 1977] report much higher numbers like 50 000 cycles or even 80 000 in an inert atmosphere. Using a special substrate a diffraction efficiency of as high as 60% [Urbach 1977] has been reported. Its resolution can be 4000 lines/mm and it is reported to have a high sensitivity. The drawbacks of Thermoplastics are its need for complex apparatus to control the aforementioned charging (high voltage) and the development (strong current). It is sensitive to dust and abrasion and has a tendency to form ghost images due to charge trapping in the emulsion. We would also like to add that purchasing such a film and the necessary equipment especially the strong corona device is quite costly. It was too expensive for this project.

2.2.4 Bacteriorhodopsin

While studying recent publications dealing with real-time holography, we discovered a material we had not used before. It is called Bacteriorhodopsin (BR) and is a living organic medium. According to the only commercial vendor of these films (Munich Innovative Biomaterials GmbH – MIB 2003) a BR film can be rewritten as many as

10^6 times without any degradation of quality. MIB list on their website [http://www.mib-biotech.de, 26.03.04] that the BR films are especially well suited for applications in high performance data processing, holographic recording, data recording, volumetric optical memories, etc. It has a good resolution, typically >5000 lines/mm and a large damage threshold. See Table 1 and Table 2 for further specifications given by MIB.

Key-Properties of Bacteriorhodopsin-Films	
Spectral Range	400 – 650 nm
Achievable Resolution	≥ 5000 lines/mm
Light Sensitivity	1 – 80 mJ/cm² (B-type recording) 30 mJ/cm² (M-type recording)
Reversibility	> 10⁶ write/erase cycles
Photochemical Bleaching	> 95% in selected films
Diffraction Efficiency	1 – 3%
Polarization Recording	possible

Table 1 Key properties of Bacteriorhodopsin films [http://www.mib-biotech.de, 26.03.04].

Typical thermal relaxation characteristics		
RTR	Wild-type	Variant D96N
N	0.3 – 1 sec	1 – 2 sec
S	20 – 30 sec	40 – 80 sec

Table 2 Thermal relaxation properties of Bacteriorhodopsin films [http://www.mib-biotech.de, 26.03.04].

For our purpose it appeared to posses all the qualities the project needed but one, namely the light sensitivity. According to an article published by Seitz and Hampp [2000] the BR film has a sensitivity suitable to generate a full holographic modulation with $100\mu W/cm^2$ of light, but the article does not mention the length of exposure. Nevertheless the same authors used a frequency doubled ND-YVO$_4$ at 532nm at 2W power to perform their experiments. If a BR film worked at this low sensitivity our lasers could produce holograms, but the exposure times would be tens of seconds. A nice explanation for how the bacteriorhodopsin molecules are affected by light is explained by the Board on Army Science and Technology [2001]:

Scientists using bacteriorhodopsin for bioelectronic devices exploit the fact that the protein cycles through a series of spectrally distinct intermediates upon absorption of light. A light-absorbing group (called chromophores) embedded in the protein matrix converts light energy into a complex series of

molecular events that store energy. This complex series of thermal reactions causes dramatic changes in the optical and electronic properties of the protein. The excellent holographic properties of bacteriorhodopsin derive from the large change in refractive index that occurs following light activation. Furthermore, bacteriorhodopsin converts light into a refractive index change with remarkable efficiency (approximately 65 percent). The protein is 10 times smaller than the wavelength of light, which means that the resolution of the thin film is determined by the diffraction limit of the optical geometry rather than the "graininess" of the film.

The optical properties of the material change in response to the incident light. The BR molecules undergo a transition through a series of molecular states upon absorbing a photon. This photocycle can be simplified as there are mainly two states in which bacteriorhodopsin occupy for any length of time. An advanced photocycle is illustrated in Figure 5.
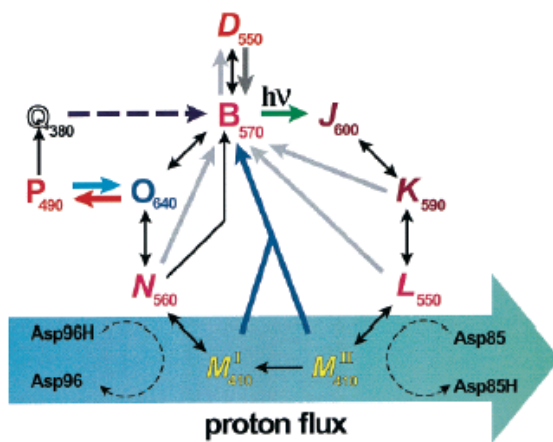
Figure 5 Bacteriorhodopsin photocycle, [Hampp 2000].

To make holograms with a BR film one uses the simplified photocycle in Figure 6, and never think more of the complex biological transitions. The B-state is the initial and M the excited state for B-type recording, and the opposite for M-type recording. According to the outlined theory developed by Seitz and Hampp [2000], there are five parameters that characterize the photoresponse of a BR film. These are the optical density (OD), light sensitivity, bleaching ratio and the thermal decay time. The OD describes the number of light sensitive molecules per area, and how much absorption to expect at different wavelengths. Light sensitivity is a dynamic variable describing how the OD change according to the light exposed. Bleaching ratio is a parameter describing the absorption changes to the initial OD, i.e. how many molecules have been converted from either B to M-state or the opposite direction. The last parameter thermal decay time is a chosen time limit. It can be the time required to thermally convert 50% [Seitz and Hampp 2000] or 63% (MIB) from the excited M-state back to ground state. The complex derivations of these will not be included in this thesis. Expressions for all of these parameters exist [Seitz and Hampp 2000] and can be used for a theoretical approach if this will be of interest at a later stage.
A typical absorption spectrum of bacteriorhodopsin is shown in Figure 6.
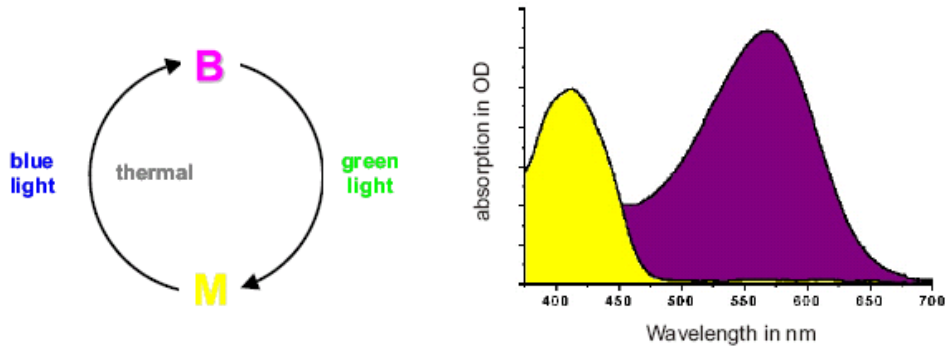
Figure 6 Simplified photochemical cycle and absorption spectrum for Bacteriorhodopsin [http://www.mib-biotech.de, 26.03.04].

This absorption spectrum for the MIB films indicates that there are two absorption regions at which the film should be addressed. The peak sensitivity of these regions is at 568 nm for molecules in the initial B-state and 412 nm for molecules in the M-state. By illuminating the film with light at a wavelength within these two distinct regions, a hologram can be recorded at one wavelength and erased with light within the other sensitivity region. Recording with light between 500 – 650 nm has so far been the most common, as the prices for laser sources in the 400 – 450 nm region have been quite expensive. The inverse approach is to first photochemically induce the molecules to the M-state using one light source within the 500 – 650 nm region, and then use a laser source in the 400 – 450 nm region to make the hologram (M-type recording, due to the initial M-state).

If a film of this recording material was to be purchased, we would have lasers available to experiment with B-type recording. A light source to photochemically convert the excited molecules back to the ground state would have to be acquired.

2.2.5 Digital Holography

Digital holography is quite different to standard optical holography. This technique was studied to see if it could be used in our project. It involves digitally reconstructing the object wave from a digital picture. Using this technique we could maybe have 3D televisions in our homes one day [http://home.earthlink.net/~digitalholography/, 11.09.04]. The definition of digital holography is not standardized and the classification of it varies with research groups. Some define it as ESPI (electronic speckle pattern interferometry) [Skarman 1994], while others [Schnars and Juptner 2002] will claim and use the term for digital recording and numerical reconstruction of holograms on a computer. We adopt the latter definition. In recent years, digital holography has been used and improved in various applications. Examples of such are deformation analysis and shape measurement [Osten et al. 2001], particle tracking [Adam et al. 1999], microscopy, [Kebbel et al. 2001] and measurement of refractive index distributions within transparent media [Dubois et al. 1999]. Most of the scientific work has been done on transparent medias and digital holography under microgravity conditions, i.e. in space. The last is a technology that has been wanted onboard the International Space Station for experiments for the Fluid Science Laboratory (FSL) under the European Space Agency (ESA). They write about digital holography on their web site:

It provides a refocusing capability of small objects in the experimental volume regardless to the focus plane of the optical set up. By this way, tracers in a fluid physics experiment could be tracked in the liquid volume giving rise to potential 3D-velocimetry map determination. [http://www.ulb.ac.be/polytech/mrc/Instruments_Design/FSL_en.html, 10.01.04]

Note that making holograms in space compared to normal gravity experiments is very different. Under microgravity conditions the tracing particles will be extremely slow and the exposure time can be increased without the problem of generating bad images. A short digression is that the German mission HOLOP-D2 used a thermoplastic film camera from Steinbichler Optotechnik Gmbh to achieve real-time recordings under microgravity in mid 90's. It is unknown to us whether they also used numerical reconstruction techniques. Today (09.01.2004) they offer digital holographic services [http://www.steinbichler.de, 09.01.04].

Digital holography differs from traditional holography, by substituting the holographic film for an electronic recording medium. There are no wet processing (silver-halide emulsions) or need for a high voltage source (order of thousand volts for a thermoplastic material). The recording medium used in digital holography is typically a scientific CCD camera, which stores the hologram electronically. It depends on budget and application which CCD camera to choose. Key specifications are wavelength sensitivity/region, the needed sensitivity level (bright objects or single photons), pixel resolution and frame-rate required. The most important specifications for the application of tracking moving particles will be lighting level and frame-rate. These are coupled in the sense that enough light must reach and illuminate the CCD-array to obtain a quality picture. If the tracer particles have moved a large distance during the recording of one picture, the image will be diffuse/blurry and difficult to retrieve information from.

2.2.5.1   Optical set-up

The common schematics of digital holography are in-line (typical Mach-Zender) and the standard off-axis hologram (Leith and Upatniks), both shown in Figure 7.
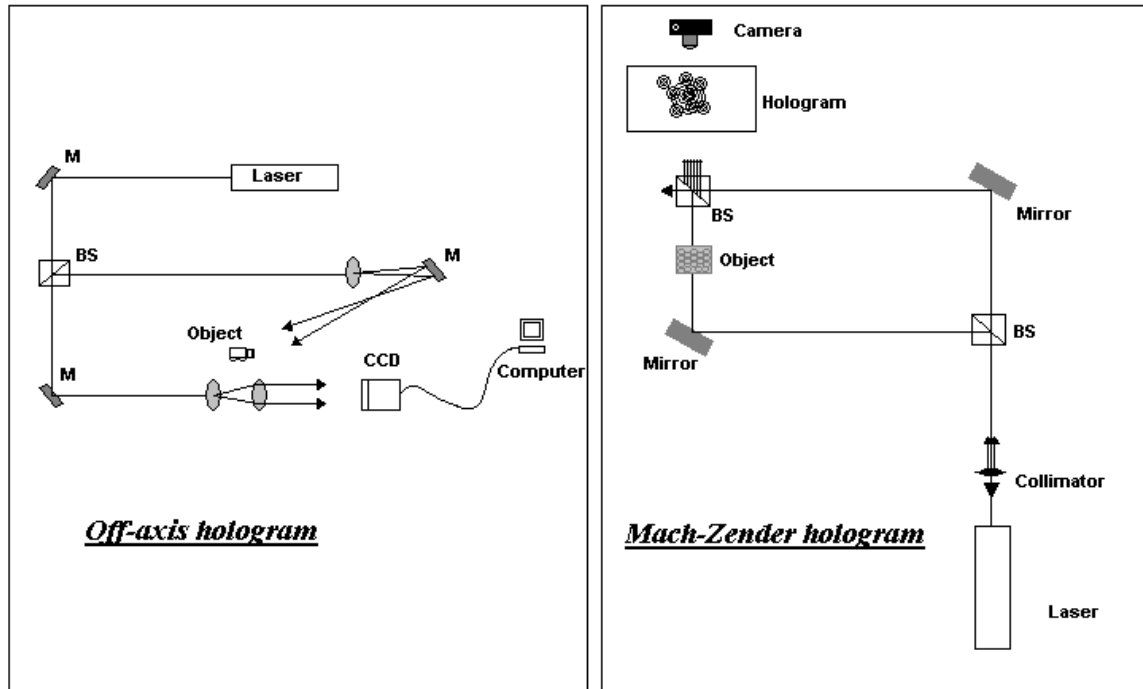
Figure 7 The most common set-ups using digital holography.

There are two major differences between these methods. The first is that the resolution (lines/mm) is much greater for an off-axis set-up. The in-line hologram will also have a problem of separating the zero order term and the twin image from the real image, just as traditional (Gabor) in-line holograms. The zero-order wave and twin image will be discussed later.

2.2.5.2 Camera resolution

The spatial frequency f, or number of lines per length of film, is determined by the angle between the object and reference wave to the normal of the film emulsion. The formula is:

$$d = \frac{\lambda}{\sin(\varphi_{object}) + \sin(\varphi_{reference})}$$ (2-5)

$$f = \frac{1}{d}$$ (2-6)

Here d is the distance between fringes, which again is the inverse of the spatial frequency. If the angle is equal for both waves, the spatial frequency becomes:

$$f = \frac{1}{d} = \frac{2\sin\varphi}{\lambda} = \frac{2}{\lambda}\sin(\frac{\theta}{2})$$ (2-7)

Now the angle is written as θ to express the total angle of both waves, as this is how most writers prefer to use it in textbooks.

For the in-line hologram this angle is small, typically below 1°. This is due to the low spatial frequency obtainable in the CCD camera. The light sensitive material must resolve the interference pattern resulting from the reference and scattered object wave. The formula for spatial frequency must hence be compared to the maximum resolvable spatial frequency of the camera, which is limited by the distance between adjacent pixels on the CCD. The maximum spatial frequency for the CCD array is given by:

$$f_{max} = \frac{1}{2\Delta x} \qquad (2-8)$$

Here Δx is the distance between neighbouring pixels. Typically the distance Δx is an order of 10 µm, indicating a maximum of ~ 50 lines/mm obtainable. This number is increasing on a daily basis, but should be compared to a silver-halide emulsion with more than 5000 lines/mm and an unlimited recording angle (between object and reference wave).

Comparing this limit with the formula for spatial frequency for the interfering set-up (and assuming a small angle $\theta \leq$ few degrees):

$$\sin\theta \approx \theta \qquad (2-9)$$

$$f_{max} = \frac{1}{2\Delta x} = \frac{2}{\lambda}\frac{\theta_{max}}{2} \qquad (2-10)$$

$$\theta_{max} = \frac{\lambda}{2\Delta x} \qquad (2-11)$$

Considering a laser source of less than one µm and separation distance between pixels of 10 µm, then the maximum resolvable angle becomes less than 0,05°. This should explain why digital holography is most often described with a Mach-Zender set-up. Then both waves can be adjusted to be almost parallel, and the angle as small as desired. Using the off-axis set-up, one would need to position the film at large distance from the object to make the angle small enough.

2.2.5.3 Reconstruction of a digital recording

Numerical reconstruction of holograms was initiated already in the 1970s by Konrad, Yaroslavski and Merzlyakov, by sampling enlarged parts of in-line hologram on a photographic plate. In the start of 1990s, Schnars and Juptner were probably the first to develop direct recording of Fresnel holograms with CCD-arrays. This removed the need for photographic films, and enabled full digital recording and processing of holograms. These holograms offered a new possibility. Traditional (optical) holographic materials record an interferometric pattern made of both phase and amplitude, but reconstruct only the amplitude at different locations in space. The digital holograms made it possible to also calculate the phase of the light waves directly from the stored information. The phase information can be filtered numerically for the object in different states, and for example used to plot deformation fields of the object surface.

The experimental set-up will determine the numerical reconstruction algorithm needed to evaluate the diffracted object wave. Articles by Schnars and Juptner [1994a,b] are good examples of how to perform the numerical reconstruction.

2.2.5.3.1 Advantages using digital holography
With digital holography, one can easily achieve exposure times of the order of 10^{-4}s, with a few milliwatts of laser power. The sensitivity and shutter speed of the camera set the limit for how fast an exposure can be. The short shutter times would have allowed the particles in our tank system to have a high velocity.

2.3 Fundamentals of Holography
To make a hologram one needs at least two electromagnetic waves to interfere in a light sensitive material. More waves will, depending on waveform and phase, construct additional interference. The most common holographic technique is to use one reference wave containing the original phase information and one modulated object wave. When these waves interfere they will make a grating inside the film emulsion. After processing, the emulsion will modulate and diffract the incoming wave and display your object, (or more correctly, the object wave). When recreating this virtual object, the film can phase modulate, amplitude modulate or use a combination of both to transform the incident light to form an image.

2.3.1 Holographic set-up techniques
An off-axis optical system is a good example of a holographic set-up, as it is the most widely used today. The first hologram was however proposed by Dr. Gabor as early as in 1948. He made an "in-line" hologram, which have some disadvantages compared to the later developed off-axis system. Among the most severe disadvantages that follow these holograms are:

- an out-of-focus conjugate twin image will coexist "on top" of the virtual image
- the virtual image will appear on a strong background illumination (zero order wave)

Both mentioned drawbacks were successfully removed when the off-axis system was introduced. As the name reveals it is based upon a separate reference wave derived from the same coherent light source to record the hologram. Most of the preceding theory is following Hariharan [1996].

The reference wave is incident on the holographic film at an offset angle θ to the object wave. To simplify the derivations, it is assumed that the reference wave be a collimated beam of uniform intensity (which is often the case). Therefore, only the phase of this wave vary across the recording material (amplitude is constant). The reference wave at the holographic film, can be expressed as an amplitude r and a $e^{i2\pi\xi x}$ phase term given by:

$$r(x, y) = re^{[i2\pi\xi_r x]}$$

(2-12)

$$\xi_r = \frac{\sin\theta}{\lambda} \tag{2-13}$$

while the object wave will vary in both phase $\phi(x,y)$ and amplitude $|o(x,y)|$ according to:

$$o(x, y) = |o(x, y)|e^{-i\phi(x,y)} \tag{2-14}$$

The resultant intensity at the photographic plate will be the absolute value of the squared waves:

$$I(x, y) = |o(x, y) + r(x, y)|^2 = (o(x, y) + r(x, y))(o*(x, y) + r*(x, y))$$

$$I(x, y) = |o(x, y)|^2 + |r(x, y)|^2 + r|o(x, y)|e^{-i\phi(x,y)}e^{-i2\pi\xi_r x}$$

$$+ r|o(x, y)|e^{i\phi(x,y)}e^{i2\pi\xi_r x} \tag{2-15}$$

$$I(x, y) = |r(x, y)|^2 + |o(x, y)|^2 + 2r(x, y)|o(x, y)|\cos[2\pi\xi_r x + \phi(x, y)]$$

The amplitude and the phase of the object wave will modulate the intensity across the holographic emulsion (interfering with the reference wave), creating interference fringes equivalent to a carrier with a spatial frequency ξ_r.

If the resultant amplitude transmittance of the holographic material, is assumed to be linearly related to the intensity in the interference pattern (indicating an absorption hologram), then the amplitude transmittance $t(x,y)$ of the hologram can be written as:

$$\vec{t}(x, y) = \vec{t}_0 + \beta T I(x, y) \tag{2-16}$$

$$\vec{t}(x, y) = \vec{t}_0 + \beta T \left\{ \begin{array}{l} |o(x, y)|^2 + |r(x, y)|^2 + r(x, y)|o(x, y)|e^{[-i\phi(x,y)]}e^{[-i2\pi\xi_r x]} + \\ r(x, y)|o(x, y)|e^{[i\phi(x,y)]}e^{[i2\pi\xi_r x]} \end{array} \right\} \tag{2-17}$$

where β is a parameter determined by the photographic material and the processing conditions. β defines a slope of the amplitude transmittance versus the exposure characteristics of the photographic material. It tells whether the material darkens after being exposed by light (negative recording) or brightens (positive recording). It can be further assumed that it gives the rate of change. T is exposure time and t_0 is a constant background transmittance.

After processing the emulsion the latent image has been developed. To reconstruct the object, the hologram is illuminated with the original reference wave (not necessary, but improves image quality). The complex amplitude $u(x,y)$ of the transmitted wave, will be the sum of the four terms of the transmittance multiplied with the reconstruction wave. In the following, the original reference wave is used to simplify the derivations.

$$u(x, y) = r(x, y)t(x, y) \tag{2-18}$$

$$u(x, y) = u_1(x, y) + u_2(x, y) + u_3(x, y) + u_4(x, y) \tag{2-19}$$

where

$$u_1(x, y) = \left(t_0 + r^2\right)re^{i2\pi\xi_r x}$$

$$u_2(x, y) = \beta Tr|o(x, y)|^2 e^{i2\pi\xi_r x}$$

$$u_3(x, y) = \beta Tr^2 o(x, y) \tag{2-20}$$

$$u_4(x, y) = \beta Tr^2 o*(x, y)e^{i4\pi\xi_r x}$$

u_1:   Attenuated zero-order, reference wave, directly transmitted

u_2:   Weak halo around the directly transmitted wave

u_3:   Original object wave. This reconstructs a virtual image of the object, in its original position. Therefore it will make an angle θ with the directly transmitted beam.

u_4:   Conjugate image. The factor $exp(i4\pi\xi_r x)$ indicates that the conjugate image is deflected twice the angle from the z-axis as the reference wave making it. This real image can be shown on a screen, as any real image.

The third term in equation (2-20), $u_3(x,y)$, describes the object wave reconstructed by the hologram (positive first-order wave). The fourth term describes the negative first-order wave of the object. The film needs to be illuminated with a wave conjugate to the reference wave *r**, to reconstruct the real image. Hence the wave should propagate in the opposite direction or one could rotate the film 180°. An equal wave front in magnitude and curvature will provide the maximum efficiency and minimum distortion in the hologram.

2.4 Experimental interferometry techniques

The objective of this thesis has been to visualize particle motion. In order to do so, several holographic techniques have been tried. An ordinary hologram alone does not uncover anything special, although it is a 3D image of the object scene. To uncover movements or changes in or near the object more advanced interferometric techniques would have to be used. If any of these techniques could reveal and display small changes that had occurred during a period of time, then it would be worth testing them out. One of the most interesting systems in interferometry is the "two-wave system" (frozen or live fringes). It has been tested extensively during this thesis. An ordinary hologram represents a three-dimensional image but the following section will introduce us to a four-dimensional space, according to Abrahamson [1981]. The forth dimension can be represented by a displacement, a deformation or a vibration. To visualize the fourth dimension we record a hologram with interference fringes covering the three-dimensional object. These fringes display the displacement of the object at any point of its observable surface. Another interferometric technique is the "time average" holography. Its applications are mainly directed to systems that have regular small displacement like vibrations, and not translation. An example is an oscillating loudspeaker. Time average holography will not be discussed further, but note that it has been investigated at the Department of Physics and Technology a few years back [Jaising 1998].

2.4.1 Two-wave holographic system

The two-wave holographic system is the most common holographic set-up for evaluating surface displacement, stress and distortion. There are two major types depending on the photographic film and technique. If the film needs to be processed (wet or dry) before the image can be reconstructed it is a so-called frozen fringe hologram. The other type is a live fringe hologram. The film then needs to have a master hologram already recorded in the emulsion, which then can interferometrically be compared to the illuminated live object. There are different methods of making the master hologram and keeping the hologram in its exact same location. To our knowledge there are three ways to accomplish this. The film can be processed and replaced in the same position (extremely sensitive to mis-alignment) by making a ultra-stable holder to reposition the film, it can be processed in-situ (using a mono-bath developing solution or other processing tools), or the film can be of a material that simply does not require processing and therefore does not need to be moved. In all three cases the master hologram can be compared to a second exposure, which is the key feature of the live fringe holograms. If the material does not need processing it will be continuously sensitive to light, and the interference pattern will last until the first image has vanished. All three methods are called real time holography due the nature of the interferometric system.

2.4.1.1   Frozen fringe hologram

One image is first recorded with the object is in its unstressed or its original state. This makes a latent image in the emulsion. After applying a load on the object or moving it, a consecutive exposure is made. It is important that the reference wave is unchanged. Now the interference structure in the emulsion is made of both exposures, and after processing the film it becomes a so-called frozen fringe (or double exposure) hologram. Illuminating the film will reconstruct the object with an interference pattern across its surface. This pattern reveals the changes that have taken place. Note that this will be equal to real-time holograms, as this too consists of two object waves (where one will be live from the object).

The frozen fringe technique is very useful to discover a discrete change in the object surface. It can also reveal a change when the object is in continuous movement. This requires a strong pulse laser to keep the exposure times extremely short. It will be as if the film has seen the object in two discrete positions. This technique has successfully been applied to visualize e.g. the pressure waves around a bullet in flight, the rotating turbine blades in a jet engine, and other fast moving objects [http://ph.ed.ac.uk/~wjh/teaching/mo/slides/holo-interferometry/holo-inter.pdf, 20.04.04].

Our laboratory is not supplied with a pulsed laser for the time being and is therefore restricted to slower moving objects. The following theory will be evaluating the two-exposure method as described in by Ostrvsky et al. [1990]. This theory will continue on the interference chapter on a single exposure hologram, but now there will be two recorded exposures, which simultaneously recreate the virtual object.

The complex object waves from the two states are given by:

$$o_1(x, y) = |o(x, y)|e^{-i\phi}$$

(2-21)

$$o_2(x, y) = |o(x, y)|e^{-i(\phi+\delta)}$$

(2-22)

The deformation or translation is assumed to only change the phase of the object wave, i.e. the extra phase term δ. Writing the reference wave as previous, but using the parameter φ for its phase:

$$r(x, y) = re^{-i\varphi}$$

(2-23)

The resulting intensity I, after the waves have interfered in the hologram plane for duration T_1 and T_2, respectively:

$$I = |o_1 + r|^2 + |o_2 + r|^2$$

(2-24)

and the corresponding exposure:

$$E = IT = T_1|o_1 + r|^2 + T_2|o_2 + r|^2$$

(2-25)

Simplifying by equal time exposure T, the total exposure becomes:

$$E = |o_1 + r|^2 T + |o_2 + r|^2 T$$

(2-26)

$$E = T\left\{|o_1|^2 + |r|^2 + o_1 * r + o_1 r * + |o_2|^2 + |r|^2 + o_2 * r + o_2 r *\right\}$$

(2-27)

$$E = T\left\{\begin{array}{l} 2\left(r^2 + |o(x, y)|^2\right) + r|o(x, y)|e^{i\varphi}\left[e^{-i\phi} + e^{-i(\phi+\delta)}\right] \\ + r|o(x, y)|e^{-i\varphi}\left[e^{i\phi} + e^{i(\phi+\delta)}\right] \end{array}\right\}$$

(2-28)

Assuming the same linear (here; scalar) relation between transmittance and exposure as before:

$$t = t_0 + \beta E$$

(2-29)

Illuminating the double-exposed hologram (after processing) with the reference wave, will give rise to a transmitted complex reconstruction wave A:

$$A = tr^{-i\varphi}$$

(2-30)

$$A = (t_0 + \beta E)r^{-i\varphi}$$

(2-31)

$$A = r^{-i\varphi}\left(t_0 + \beta T \left\{ \begin{matrix} 2\!\left(r^2 + |o(x,y)|^2\right) + r|o(x,y)|e^{i\varphi}\left[e^{-i\phi} + e^{-i(\phi+\delta)}\right] + \\ r|o(x,y)|e^{-i\varphi}\left[e^{i\phi} + e^{i(\phi+\delta)}\right] \end{matrix} \right\} \right) \tag{2-32}$$

$$A = \left\{ \begin{matrix} \underbrace{\left[t_0 + 2\beta T\!\left(r^2 + |o(x,y)|^2\right)\right]r^{-i\varphi}}_{1} + \underbrace{\beta T r^2 |o(x,y)|\left[e^{-i\phi} + e^{-i(\phi+\delta)}\right]}_{2} + \\ \underbrace{\beta T r^2 |o(x,y)|\left[e^{i\phi} + e^{i(\phi+\delta)}\right]e^{-i2\varphi}}_{3} \end{matrix} \right\} \tag{2-33}$$

The first term in equation (2-33) represent the zero order wave. It is the illumination wave that traverses directly through the hologram and is only amplitude modulated by a constant factor.

The second term differs from what has been derived earlier for a single exposure hologram, by reconstructing two object waves with slightly different phases. It will be forming two virtual objects, factorised by some parametric constants.

The third term describes two distorted (by the exponential factor) conjugate, real images. Note that by illuminating the film with the conjugate reference wave ($re^{i\varphi}$), the reconstructed image will be the correct (non distorted) conjugate objects, as the exponential factor reduces to the original reference wave. The conjugate image will be identical to the virtual image, although it must be transposed on a sheet of paper to be observed.

To find the intensity distribution of the virtual image, the reconstructed virtual wave is squared:

$$I_M = \left| \beta T r^2 |o(x,y)|\left[e^{-i\phi} + e^{-i(\phi+\delta)}\right] \right|^2 \tag{2-34}$$

$$I_M = \beta^2 T^2 r^4 o^2 \left| e^{-i\phi} + e^{-i(\phi+\delta)} \right|^2 = \beta^2 T^2 r^4 o^2 \left[1 + 1 + e^{i\phi}e^{-i(\phi+\delta)} + e^{-i\phi}e^{i(\phi+\delta)} \right] \tag{2-35}$$

$$I_M = \beta^2 T^2 r^4 o^2 \left[2 + e^{-i\delta} + e^{i\delta} \right] = \beta^2 T^2 r^4 o^2 \left[2 + 2\cos(\delta) \right] \tag{2-36}$$

$$I_M = 4\beta^2 T^2 r^4 o^2 \left[\cos^2\!\left(\frac{\delta}{2}\right) \right] \tag{2-37}$$

The intensity varies as a squared cosine function across the image dependent on the second wave phase difference δ. A double-exposure hologram of a metal plate is shown in Figure 8. The figure is taken from later experiments and can be found as Figure 17 under section 2.4.3.
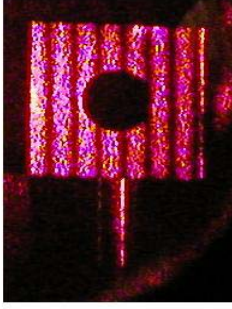
Figure 8 Example of a double exposure hologram. Object translation has been parallel to the film.

Note that equation (2-37) also predicts the intensity of live fringes. For real-time holograms the phase difference $\delta(t)$, and the amplitude of the live-object wave will be time-dependent. The two virtual object waves will be:

$$o_1(x, y) = \beta T r^2 |o(x, y| e^{-i\phi} \tag{2-38}$$

$$o_2(x, y) = \chi |o(x, y| e^{-i(\phi+\delta)} \tag{2-39}$$

The factor χ is an attenuation coefficient for the wave modulation through the hologram emulsion. If the exposure parameter β is positive, then the previous derivations hold and the interference stripes will be bright. If β is negative (darkening the film according to exposure), the interfering object waves will be out of phase resulting in dark zero-order fringes. The derivation of the intensity of the object image will result in a squared sine distribution:

$$I_M = I_O \left[\sin^2 \left(\frac{\delta(t)}{2} \right) \right] \tag{2-40}$$

where I_O represent the parametric factors.

2.4.2 Simplified theory for double exposure holograms

For our experimental purposes, we wanted a theory that could readily be employed to practical measurements. We knew to expect a squared sine or cosine distribution of stripes across the object, due to an in-plane translation or rotation, but to derive an expression for the distance between stripes we chose to follow the theory of an educational article published for an optics course by Hossack [2003] at the Department of Physics, Edinburgh University.

The theory describes a rigid object that moves between exposures. It can be applied to either frozen or live fringes. The two surface points P and Q will move according to the object displacement vector **a** as shown in Figure 9. Note that the unit vectors $\hat{r}$ and $\hat{s}$ are assumed equal for the two points P, P'. The illumination unit vector $\hat{r}$ will be equal since it is a collimated wave, while the observation unit vector is assumed equal due to the large distance to the hologram plane and the small displacement |**a**|.

The point P and Q are assumed equally far from the hologram plane in $\hat{z}$ direction, due to the small distance between them (as shown in Figure 10). The derivations for points P-P' is equivalent to that for Q-Q', and will therefore only be shown for the first case.
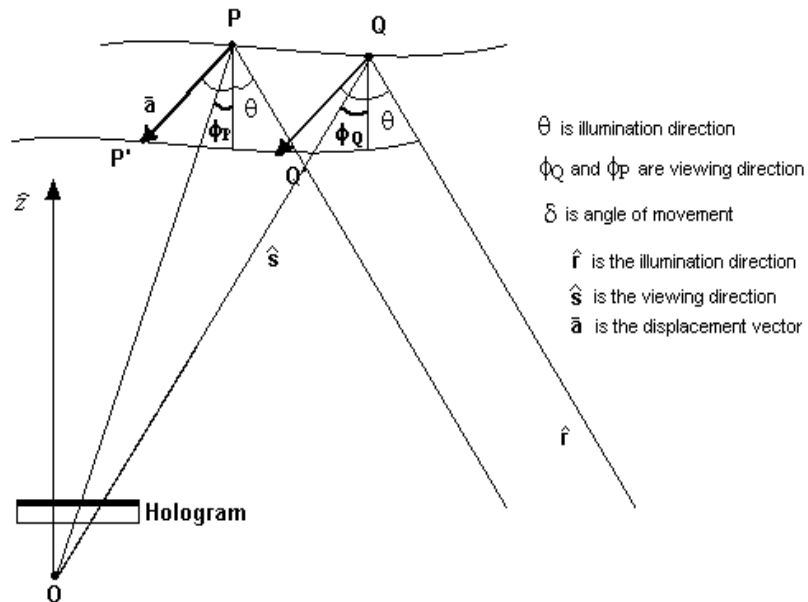

Figure 9 Schematics for the theoretical derivations of surface displacement.

The parameters are:
$\hat{r} - illu\min ation\_unit\_vector$

$\hat{s} - observation\_unit\_vector$

$\bar{a} - displacement\_vector$

$\delta - angle\_of\_movement$

$\theta - angle\_of\_illu\min ation$
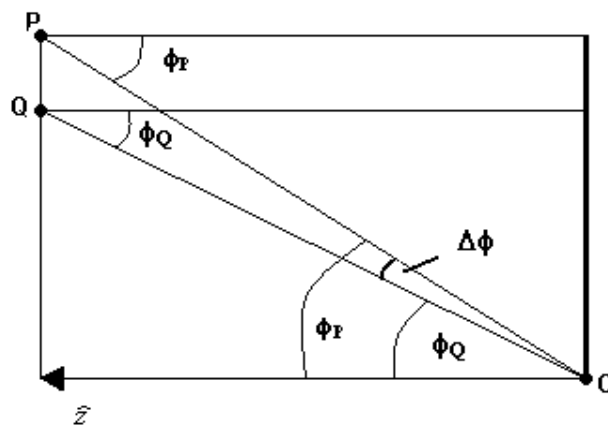
$\phi - angle\_of\_observation$

Figure 10 Angles used in the derivations.

The difference in optical path length between the first and second exposure (P and P') is:

$$\Delta = \vec{a} \cdot \hat{r} + \vec{a} \cdot \hat{s} = \vec{a} \cdot (\hat{r} + \hat{s}) \tag{2-41}$$

This is displacement in **r**-direction and in **s**-direction.

This path difference can also be expressed as:

$$\vec{a} \cdot (\hat{r} + \hat{s}) = a\cos(\theta + \delta) + a\cos(\phi_P - \delta) \tag{2-42}$$

The rays from the object at P and P' will interfere at the hologram point O. The condition for a constructive interference or "bright fringe" is that the optical path difference be equal to an integer of the wavelength:

$$\vec{a} \cdot (\hat{r} + \hat{s}) = \pm n\lambda \tag{2-43}$$

By equating the condition for a bright fringe at P and the next at Q, then the path difference can be expressed by:

$$\vec{a} \cdot (\hat{r} + \hat{s}) = a\cos(\theta + \delta) + a\cos(\phi_P - \delta) = n\lambda \qquad \textbf{(2-44)}$$

$$\vec{a} \cdot (\hat{r} + \hat{s}) = a\cos(\theta + \delta) + a\cos(\phi_Q - \delta) = (n+1)\lambda \tag{2-45}$$

By subtracting the equations:

$$a\cos(\phi_P - \delta) - a\cos(\phi_Q - \delta) = n\lambda - (n+1)\lambda \tag{2-46}$$

$$\cos(\phi_P - \delta) - \cos(\phi_Q - \delta) = \frac{-\lambda}{a} \tag{2-47}$$

To simplify the equations, we introduced some geometric parameters:

$$\phi = \phi_P \tag{2-48}$$

$$\phi_Q = \phi_P - \Delta\phi = \phi - \Delta\phi \tag{2-49}$$

$$\alpha = \phi_P - \delta = \phi - \delta \tag{2-50}$$

Inserting these parameters we get:

$$\cos(\phi_P - \delta) - \cos(\phi_Q - \delta) = -\frac{\lambda}{a} \Rightarrow \cos(\alpha) - \cos(\phi - \Delta\phi - \delta) = -\frac{\lambda}{a} \tag{2-51}$$

$$\cos(\alpha) - \cos(\alpha - \Delta\phi) = -\frac{\lambda}{a} \tag{2-52}$$

$$\cos(\alpha - \Delta\phi) - \cos(\alpha) = \frac{\lambda}{a} \tag{2-53}$$

$$[\cos(a \pm b) = \cos a \cos b \mp \sin a \sin b] \tag{2-54}$$

$$\cos(\alpha)\cos(\Delta\phi) + \sin(\alpha)\sin(\Delta\phi) - \cos(\alpha) = \frac{\lambda}{a} \tag{2-55}$$

The object displacement |**a**| is small compared to the illumination length |**s**|, indicating that the angle $\Delta\phi$ is small. Therefore the expression can be approximated by:

$$\cos(\Delta\phi) \approx 1 \tag{2-56}$$

$$\sin(\Delta\phi) \approx \Delta\phi \tag{2-57}$$

Hence:

$$\cos(\alpha)\cos(\Delta\phi) + \sin(\alpha)\sin(\Delta\phi) - \cos(\alpha) = \frac{\lambda}{a} \tag{2-58}$$

Can be simplified to:

$$\cos(\alpha) + \sin(\alpha)\Delta\phi - \cos(\alpha) \approx \frac{\lambda}{a} \tag{2-59}$$

$$\sin(\alpha)\Delta\phi \approx \frac{\lambda}{a} \Rightarrow \Delta\phi \approx \frac{\lambda}{a\sin(\alpha)} = \frac{\lambda}{a\sin(\phi - \delta)} \tag{2-60}$$

The separation D between the bright fringes then can be found from the scalar distance R from the observation point to the second bright fringe at Q as shown in Figure 11.
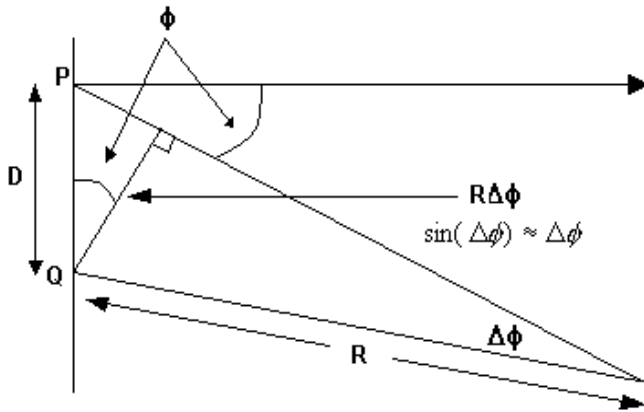

Figure 11 Geometrical distance D, between bright fringes in a double exposure hologram.

The separation distance between bright fringes D, is given by:

$$D = \frac{R\Delta\phi}{\cos(\phi)} \approx \frac{R\lambda}{a\cos(\phi)\sin(\phi - \delta)} \tag{2-61}$$

Equation (2-61) tells us about the scalar distance between two bright interference fringes on the object. It does not inform us of the direction of the lines, and is only valid for displacements in the plane of incidence given by the unit vectors $\hat{r}$ and $\hat{s}$. Information between exposures is lost. Note that this theory makes use of a collimated reference wave, which simplifies the derivations.

2.4.2.1   Applied theory for double exposure holograms

Although the previous chapter makes quite a lot of assumptions and approximations, equation (2-61) reveals some of the nature of two-wave theory for simple displacements. It would be interesting to do some tests to check its validity. We used a few silver halide films (649-F) from Kodak, which have good exposure characteristics. These films can obtain more than 3000 lines/mm and consist of large silver grains to ensure fast development. Confer to Blom [2002] for more details on holographic emulsions.

The recording specifications to make a transmission hologram was in agreement to Singstad [1996], and the set-up is shown in Figure 12.
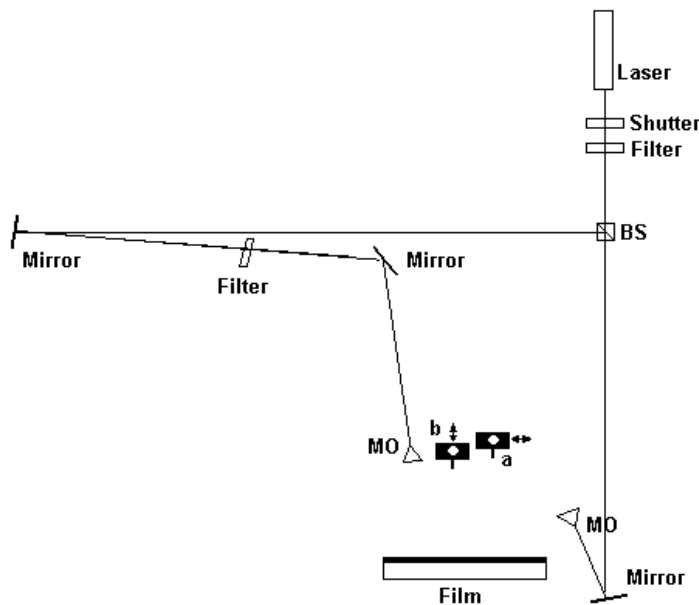
Figure 12 Set-up for double exposure holograms.

BS   - beamsplitter
MO   - microscope objective

Using this set-up we obtained experimental data to compare measurements with theory. The measured values diverged from the predicted linear theoretical values, as seen in Figure 13 and Figure 14. The experimental data plotted in these two figures will also be used later. The data is also given in Table 3.
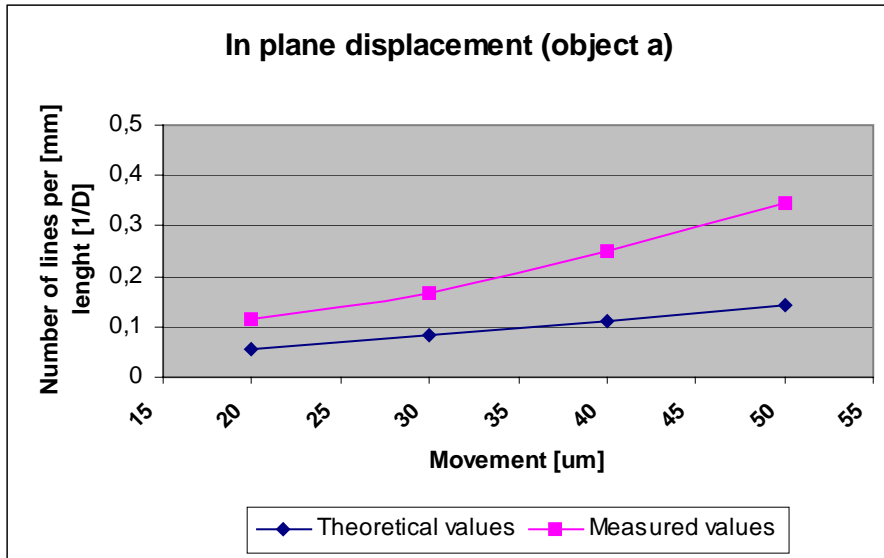
Figure 13 Fringes per length, across the object surface. The metal object moves parallel to the film plane. Comparison of experimental and theoretical data.

In Figure 13 equation (2-61) has been used, but note that for in-plane translations equation (2-61) can for small angles of observation, φ, be roughly simplified to include only scalar sizes. For in-plane translations the angle of movement, δ, is 90°, hence the separation distance between fringes can be written:

$$D \approx \frac{R\lambda}{a\cos(\phi)\sin(\phi-\delta)} \approx \frac{R\lambda}{a\cos^2(\phi)} \approx \frac{R\lambda}{a} \tag{2-62}$$

Figure 14 Fringes per length, across the object surface. The metal object moves out of the film plane. Comparison of experimental and theoretical data.

Discussion

The experimental results do not show a linear relation between the separation distance and the displacement. Translation parallel to the hologram plate, have a linear appea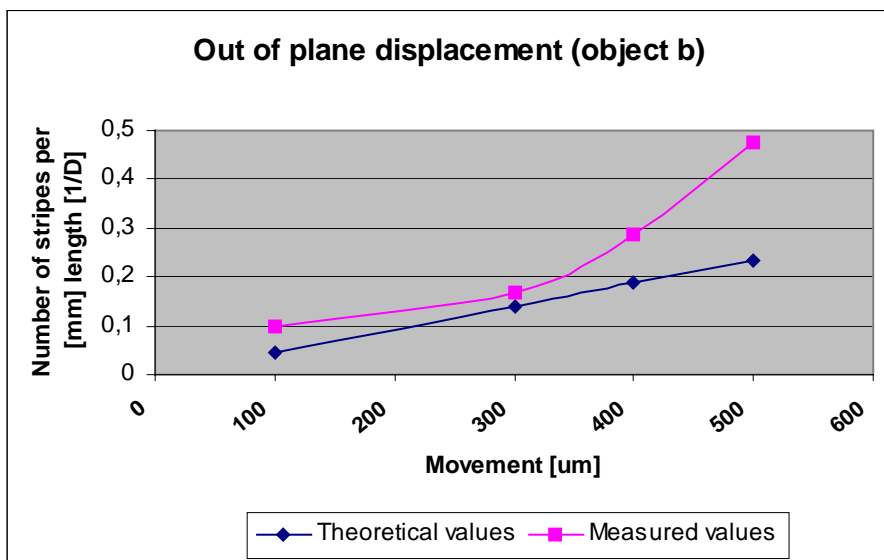rance but also some non-linear effects. These effects could be the consequence of translations not perfectly parallel to the hologram plane. The theory for the translation normal to the surface of the hologram plane does not appear to be adequate. The measured values show a distinct second order property. It is also apparent that the interference patterns arising from these displacements will be concentric circles with the centre shifted along the x-axis. The fringes will move around in front of the object and change depending on the observation point. The derived theory indicates a constant separation distance for a given set-up, which does not fit the translation normal to the hologram plane. From the holograms it is obvious that the fringe separation distance decreases further from the fringe centre. The theory lacks the parameter concerning this fringe order. This was the motivation for a more advanced theoretical approach.

2.4.3 A more advanced theory for double exposure holography

The following theoretical derivation is mainly following Hecht et al. [1973]. This theory is very similar to the simplified holographic interferometry chapter, but is more thorough using vector derivation for the optical path length difference. To include the entire theory would be too much, so only the basic figures, the applied assumptions and the most useful formulas will be shown here.

It is assumed an observer having an observation vector 'O_1' to a point on the object and that the laser expander (from the microscope objective) have an illumination vector 'I_1'. The vector from the chosen origin '0' in the centre of the specimen, on the surface of the specimen, to point 1, is called 't' vector. When the specimen is displaced, point 1 will move according to the displacement vector 'D', to point 2, as shown in Figure 15.
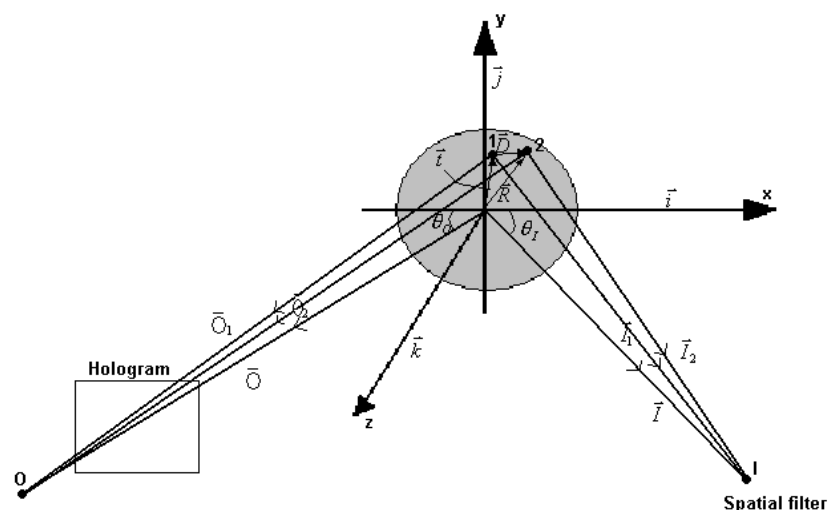

Figure 15 Angles and distances used in the derivations, from Hect et al. [1973].

The total optical path length difference from an observer at O, via the object and back to the illumination source at I, can be shown to be:

$$L = \left[\left(O_2 - O_1\right) + \left(I_2 - I_1\right)\right] \tag{2-63}$$

$$L \approx \underbrace{\left[\frac{O+I}{OI}\right]\left[\vec{t}\cdot\vec{D} + \frac{D^2}{2}\right] - \vec{D}\cdot\left[\frac{\vec{O}}{O} + \frac{\vec{I}}{I}\right]}_{1.st.order}$$

$$+ \left\{\frac{O}{8}\left[\frac{2\left(\vec{t}\cdot\vec{O}\right)}{O^2} - \frac{t^2}{O^2}\right]^2 - \frac{O}{8}\left[\frac{2\left(\vec{t}\cdot\vec{O}\right)}{O^2} + \frac{2\left(\vec{D}\cdot\vec{O}\right)}{O^2} - \frac{t^2}{O^2} - \frac{D^2}{O^2} - \frac{2\left(\vec{t}\cdot\vec{D}\right)}{O^2}\right]^2 + \frac{I}{8}\left[\frac{2\left(\vec{t}\cdot\vec{I}\right)}{I^2} - \frac{t^2}{I^2}\right]^2 \right. \tag{2-64}$$

$$\left. - \frac{I}{8}\left[\frac{2\left(\vec{t}\cdot\vec{I}\right)}{I^2} + \frac{2\left(\vec{D}\cdot\vec{I}\right)}{I^2} - \frac{t^2}{I^2} - \frac{D^2}{I^2} - \frac{2\left(\vec{t}\cdot\vec{D}\right)}{I^2}\right]^2 + ... \underbrace{}_{3.rdorder} + ...\right\}$$

$$\vec{t} = x\vec{i} + y\vec{j} \tag{2-65}$$

Only two approximations are used so far. The most important is a binomial expansion of the roots used to find the optical path length O_1, O_2, I_1 and I_2. This approximation is qualitatively very useful since second order and higher term of the expansion in equation (2-64) do not have to be evaluated except for translation in the out-of-plane direction along the z-axis. This is due to the less strength of the higher order terms [Hecht 1972]. So for translation in x and y directions, only first order terms of the formula will be compared to the measured values. The other approximation is that the object surface, or object plane, lies in the x, y plane as described by the **t** vector. This does not apply to our experiments. To avoid specular reflection from the bright metal objects to the hologram, they were turned around the y-axis, and therefore the derivation should include z-components. Although this small rotation will contribute to the system, it was believed that it would not change the expression for the separation of fringes to the displacement. This deviation in experimental set-up can be represented by a rotation in the x-z plane (hence a rotation of the angles of illumination and observation) and altering the movement vector **D** to include a z-displacement. This rotation around the y-axis has been measured to be 18,7° for the object that is displaced out of plane (z-direction), and 10,9° for the object that moves parallel to the hologram. This issue will be discussed further after the derivation of out-of plane movement.

The displacements used in our tests are discrete and translational. It is further assumed that the plane defined by the laser *I*, origin on the object surface *0* and the observation point *O*, lie in the x-z plane of the coordinate system, and is horizontal. Then the unit observation and illumination vectors, and the total optical path length change become:

$$\frac{\vec{O}}{O} = -\cos\theta_O\vec{i} + \sin\theta_O\vec{k} \tag{2-66}$$

$$\frac{\vec{I}}{I} = \cos\theta_I\vec{i} + \sin\theta_I\vec{k} \tag{2-67}$$

30

$$L \approx \left[\frac{O+I}{O*I}\right]\left[\vec{t} \cdot \vec{D} + \frac{D^2}{2}\right] - \vec{D} \cdot \left[(\cos\theta_I - \cos\theta_O)\vec{i} + (\sin\theta_I + \sin\theta_O)\vec{k}\right] \qquad (2\text{-}68)$$

This approximation will be valid in our experimental set-up. All optical elements on the optical table are adjusted to follow the laser beam's height above the table surface. This had been carefully adjusted to be horizontal. The only comment that needs to be added is that observation should be in the centre of the hologram to match the same height. For translation in the x, y directions the fringes will focus behind the object, while z-translation results in fringes focused in front of the specimen. Hence the observation position becomes more important in the out of plane (z-direction) displacement, were fringes will move around in front of the object as the observation direction is altered.

For pure displacements in the x and y direction the total optical path length change become:

$$\vec{D} = D\vec{i} \Rightarrow L_x \approx \left[\frac{O+I}{OI}\right]\left[D\left(x + \frac{D}{2}\right)\right] - D(\cos\theta_I - \cos\theta_O) \qquad (2\text{-}69)$$

$$\vec{D} = D\vec{j} \Rightarrow L_y \approx \left[\frac{O+I}{OI}\right]\left[D\left(y + \frac{D}{2}\right)\right] \qquad (2\text{-}70)$$

Here one should note the first factor in the brackets, which will prove to be a significant difference in the two derived theories (simplified and advanced displacement theories). This will be explained in more detail later.

Since equation (2-69) is only dependent on *x* and not *y* and *z*, translations along the x-axis will produce vertical fringes (either in front or behind the object).

Equation (2-70) is only dependent on *y* and not *x* and *z*, and therefore translations along the x-axis will produce horizontal fringes. For translation along the x-axis, we needed to find an expression for the separation of the fringes for different displacements *D*. Note that the derivations have been performed to evaluate the optical path length change to the dark fringes by an *integer number of wavelength*. An expression for the x-position of the fringes can be found.

$$L_x \approx \left[\frac{O+I}{OI}\right]\left[D\left(x + \frac{D}{2}\right)\right] - D(\cos\theta_I - \cos\theta_O) = (2n-1)\frac{\lambda}{2} \qquad (2\text{-}71)$$

$$x = \frac{\left[D(\cos\theta_I - \cos\theta_O) + (2n-1)\frac{\lambda}{2}\right]}{D\left[\frac{O+I}{OI}\right]} - \frac{D}{2} \qquad (2\text{-}72)$$

Notice that fringes will be aligned in parallel to the y-axis, since the only parameter describing the localization of the fringes is the x-value. The difference in x-position between fringes can be found by:

$$\Delta x = \frac{\left[D(\cos\theta_I - \cos\theta_O) + (2(n+1)-1)\frac{\lambda}{2}\right]}{D\left[\frac{O+I}{OI}\right]} - \frac{D}{2} - \left\{\frac{\left[D(\cos\theta_I - \cos\theta_O) + (2(n+1)-1)\frac{\lambda}{2}\right]}{D\left[\frac{O+I}{OI}\right]} - \frac{D}{2}\right\} \qquad (2\text{-}73)$$

$$\boxed{\Delta x = \frac{\lambda}{D\left[\frac{O+I}{OI}\right]} = \frac{O\lambda}{D}\left[\frac{I}{(O+I)}\right]} \qquad (2\text{-}74)$$

Discussion

Equation (2-74) is identical to the earlier derived equation (2-62) except for the factor in the parenthesis. It reveals the factor ~ 0,5, that has been missing earlier, as seen in Figure 13. The explanation for this difference, arise from an important change in assumptions. The first theory assumed a plane collimated illumination wave, while the second theory does not. Only the first double-exposure experiment that was taken in our laboratory used a collimated illumination wave. The first test showed some bad exposure characteristics, and the experiment was redone at a later time. During the second experiment both reference and illumination waves were spherical. The approximations used in deriving the theory then failed. To evaluate the last theory for a collimated illumination wave, the distance 'I' from the pinhole has to be evaluated as infinite. Then the formula becomes identical:

$$\Delta x = \lim_{I \to \infty}\left\{\frac{O\lambda}{D}\left[\frac{I/I}{(O/I + I/I)}\right]\right\} \qquad (2\text{-}75)$$

$$\Delta x = \frac{O\lambda}{D} \qquad (2\text{-}76)$$

2.4.3.1   In plane displacements

The measured values for separation of fringes due to displacement along x and z-direction are listed in Table 3. These are the same values as used in Figure 13.

	Number of stripes N	Separation distance D	Fringe-separation	Projected image length	Real separation D
1a (20μm)	7	8,6 [mm]			
2a (30μm)	10	6,0 [mm]			
3a (40μm)	15	4,0 [mm]			
4a (50μm)	21	2,9 [mm]			
1b (100μm)			3,8 [mm]	31 [mm]	7,4 [mm]
2b (300μm)			3 [mm]	29,1 [mm]	6,2 [mm]
3b (400μm)			1,5 [mm]	30 [mm]	3,0 [mm]
4b (500μm)			1,5 [mm]	55 [mm]	1,6 [mm]

Table 3 Measured and calculated values for the separation of fringes for in-plane and out-of plane displacements.

Note. Object length is 60mm.

The plotted parameters for the in-plane translations are:

Object *a*				THEORY				MEASURED	
Distance:	**O**	0,522	m.		Movement D	L [m]	L [mm]	1/L	L [mm]	1/L
Distance	**I**	0,450	m.	1 - a	2,00E-05	7,65E-03	7,646	0,131	8,6	0,12
Wavelength	λ	632,8	nm	2 - a	3,00E-05	5,10E-03	5,098	0,196	6,0	0,17
Observation angle	**θo**	1,307	rad	3 - a	4,00E-05	3,82E-03	3,823	0,262	4,0	0,25
Illumination angle	**θI**	1,365	rad	4 - a	5,00E-05	3,06E-03	3,059	0,327	2,9	0,35

Table 4 Table illustrating the plotted values in Figure 16.

All measurements have been taken from the real image transposed onto a semi-transparent sheet of paper. The fringe separation is equal for different n-orders for translation along the x-axis as seen in Figure 17, and the most practical technique to find it was to count the total number of fringes. The length of the object could then be divided by the number of fringes to find the separation distance, *D* with an accuracy of about 0,1mm.
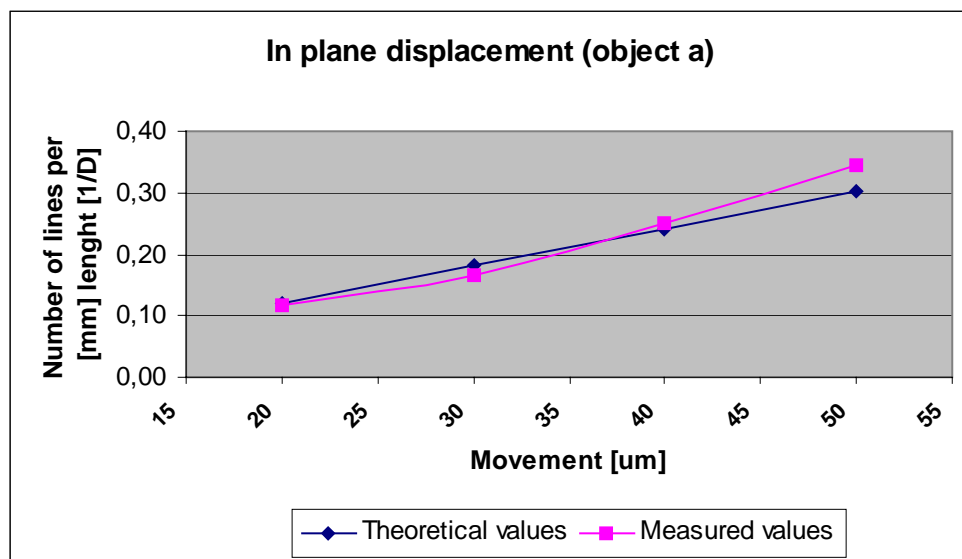
Figure 16 In plane translations.

<u>Discussion</u>
Finding the missing factor (~ 0,5), and realizing the importance of the curvature of the reference wave, the theory seems to fit the measured values. The figure indicates some second order behaviour, but this can possibly be a consequence of mis-alignment in the set-up.

2.4.3.2   Out of plane displacements
The theory for displacement out of plane is in fact very interesting. In addition to the previous derivation it includes second order terms from equation (2-64).

$$\vec{D} = D\vec{k} \tag{2-77}$$

$$\vec{t} = x\vec{i} + y\vec{j} \tag{2-78}$$

$$
\begin{aligned}
L \approx & \frac{D^2}{2}\left[\frac{O+I}{OI}\right] - D(\sin\theta_O + \sin\theta_I) - \frac{O^3+I^3}{2(OI)^3}\left[\frac{D^4}{4} + \frac{D^2(x^2+y^2)}{2}\right] + \frac{D(x^2+y^2)}{2}\left[\frac{\sin\theta_I}{I^2} + \frac{\sin\theta_O}{O^2}\right] \\
& + \frac{D^3}{2}\left[\frac{\sin\theta_I}{I^2} + \frac{\sin\theta_O}{O^2}\right] + xD\left[\frac{\cos\theta_O\sin\theta_O}{O} - \frac{\cos\theta_I\sin\theta_I}{I}\right] \\
& - \frac{D^2}{2}\left[\frac{\sin^2\theta_I}{I} + \frac{\sin^2\theta_O}{O}\right] + \frac{xD^2}{2}\left[\frac{\cos\theta_O}{O^2} - \frac{\cos\theta_I}{I^2}\right]
\end{aligned} \tag{2-79}
$$

Solved for x and y and setting it equal to an integer number of wavelength, it shows the equation of a displaced circle depending on the n'th order fringe:

$$
\begin{aligned}
& \left(x^2+y^2\right)\underbrace{\left\{\frac{D}{2}\left[\frac{\sin\theta_I}{I^2} + \frac{\sin\theta_O}{O^2}\right] - \frac{D^2}{2}\left[\frac{O^3+I^3}{2(OI)^3}\right]\right\}}_{a} \\
& + x\underbrace{\left\{D\left[\frac{\cos\theta_O\sin\theta_O}{O} - \frac{\cos\theta_I\sin\theta_I}{I}\right] + \frac{D^2}{2}\left[\frac{\cos\theta_O}{O^2} - \frac{\cos\theta_I}{I^2}\right]\right\}}_{b} \\
& + \underbrace{\left\{\begin{matrix} \frac{D^2}{2}\left[\frac{O+I}{OI}\right] - D(\sin\theta_O + \sin\theta_I) - \frac{D^4}{4}\left[\frac{O^3+I^3}{2(OI)^3}\right] + \frac{D^3}{2}\left[\frac{\sin^2\theta_I}{I} + \frac{\sin^2\theta_O}{O}\right] \\ -\frac{D^2}{2}\left[\frac{\sin^2\theta_I}{I} + \frac{\sin^2\theta_O}{O}\right] - n\lambda + \frac{\lambda}{2} \end{matrix}\right\}}_{c} = 0
\end{aligned} \tag{2-80}
$$

The circle is displaced along the x-axis by an amount of –b/2a. This is about 4,3 cm for a displacement of 100 μm in our experimental set-up, and made it impossible to see the fringe centre. This centre of fringes was also partly displaced in the vertical direction as shown in the figure below. The reason for this is probably that the centre of the object illumination source (i.e the pinhole) has been at a slightly higher position than the object. The size of the displacement along the horizontal direction is held constant for different movements D, while the number of fringes per length increases for larger translations.

$$
\begin{aligned}
& Circle: \\
& (x-h)^2 + (y-k)^2 = r^2
\end{aligned} \tag{2-81}
$$

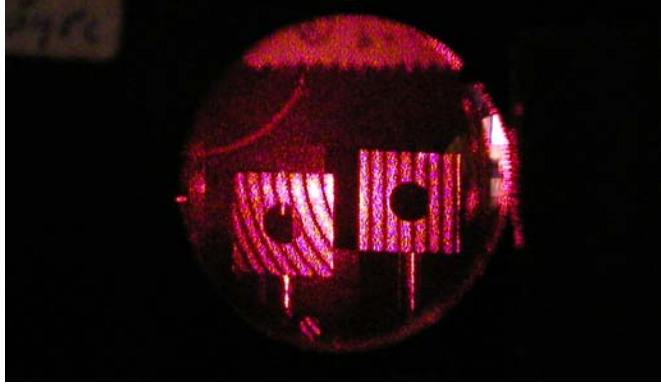*For a circle displaced 'h' in x-direction and 'k' in the y-direction.*

Figure 17 A hologram showing the two objects in the tests. Object *b* to the left is moved out of plane, while object *a* is translated parallel to the hologram plane.

For z-movement (object b) the distance between fringes are decreasing for increasing distance from the displaced centre of the fringe circles, as shown in Figure 17. The separation distance is therefore depending on the fringe order. To find the separation, it was necessary to choose a fixed point on the object and measure this location each time. Due to the centre of the fringes being displaced the fringe order could not be counted to ensure the exact same observation position. The total displacement from first to last translation was assumed not to change the fringe order significantly. The separation distance between adjacent fringes was measured and adjusted with the "projected/real object length" to find the separation in the correct scale. The projected image had to be larger than the object to best find the separation distance for large displacements when the fringes were close. For larger movements the fringes got closer and closer together. Both theory and measured values indicate this. To find an expression for the spacing between two n'th fringes, equation (2-80) was differentiated with respect to the x position on the axis:

$$\alpha\left(x^2 + y^2\right) + x\beta + \delta = 0 \tag{2-83}$$

$$\left[\frac{\partial n}{\partial x}\right]^{-1} = \frac{\partial x}{\partial n} = \frac{\lambda}{2x\alpha + \beta} \tag{2-84}$$

$$\frac{\partial x}{\partial n} = \frac{\lambda}{2x\left\{\frac{D}{2}\left[\frac{\sin\theta_I}{I^2} + \frac{\sin\theta_O}{O^2}\right] - \frac{D^2}{2}\left[\frac{O^3 + I^3}{2(OI)^3}\right]\right\} + \left\{D\left[\frac{\cos\theta_O \sin\theta_O}{O} - \frac{\cos\theta_I \sin\theta_I}{I}\right] + \frac{D^2}{2}\left[\frac{\cos\theta_O}{O^2} - \frac{\cos\theta_I}{I^2}\right]\right\}}$$

(2-85)

Choosing the x-position to be at 1cm along the x-axis gave the values listed Table 5. The calculated spacing at the centre is also plotted in Figure 18.

Object b				THEORY			MEASURED	
Distance	O	5,10E-01	m		Movement D	1/L (for x=0)	1/L (for x=1cm)	L [med mer]	1 / L
Distance	I	4,50E-01	m	1 - b	1,00E-04	0,047	0,036	7,4	0,135
Wavelength	λ	6,33E-07	m	2 - b	3,00E-04	0,141	0,108	6,2	0,161
Observation angle	θo	1,431	rad	3 - b	4,00E-04	0,188	0,144	3	0,333
Illumination angle	θI	1,340	rad	4 - b	5,00E-04	0,235	0,181	1,6	0,625

Table 5 Measured and theoretical values for out of plane translations in double exposure holograms.
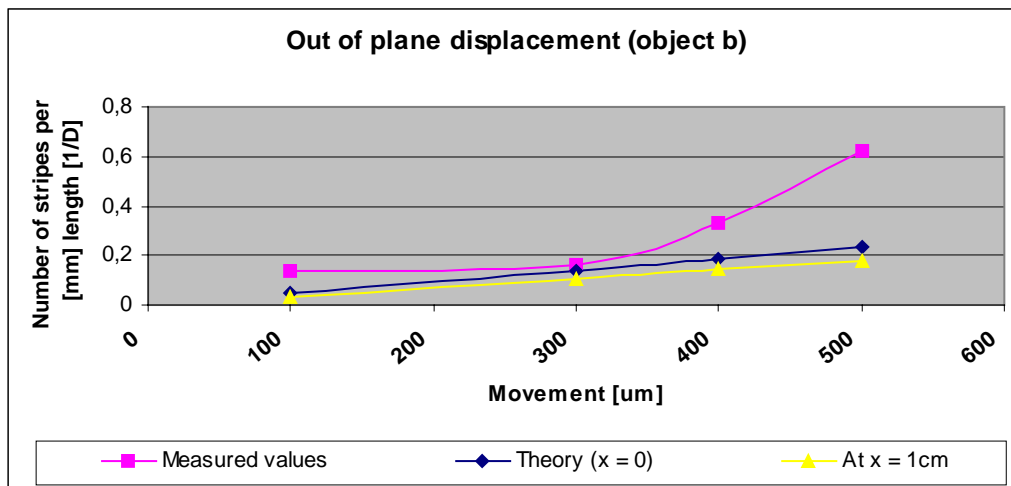
Figure 18 Out of plane translation, double exposure holograms.

Discussion

The measured diagram does not show a linear nature. The effect resulting from the rotation of the objects around the y-axis is not obvious. To compensate for this change one can use the aforementioned approach to rotate the coordinate system (changing the illumination and object angle) and replace the movement vector with one that include a movement in both x and z-direction, or do the derivation with the '**t**' vector having all three axis components (x, y and z) and keeping the movement as a pure x or z-translation. Both approaches result in a complicated mathematical expression. If the movement has an out-of plane component, one should include the second order term of equation (2-64), and the expression for optical path length difference grows big. It is believed that this does not cause the largest deviations between theory and measured values, but it might contribute.

The most important reason for why the measured values show a second order deviation is due to measuring different fringe orders. It appears as if we have measured different fringe orders as the displacement was increased. As mentioned in section 2.4.3.2 all fringe separation measurements were performed at a fixed point on the object. The separation of fringes decrease for higher fringe orders as can readily be seen in Figure 17. If we measured a higher fringe order for each new displacement, this has contributed to a decreasing separation distance, in addition to the decreased separation distance caused by the increased displacement. The problem is that there is no way of knowing which fringe order we have observed, as the fringe centre is not shown. Adjusting the set-up with a repositioned object *a* moving perpendicular to the film could have solved the problem. The centre of fringes had then been shown. This was not done as the purpose of these tests was to get acquainted with some of the nature of interferometry. Further mathematical evaluation will not be pursued.

<u>An important note</u> is that we did not know how much the fringe order changed until the real-time experiments were performed later in the project. At the time these double exposure tests were carried out we only had information revealing the change between two discrete states. We had no continuous information about the fringe order.

This further emphasizes the value of continuous information, which real-time holography yields.

2.5 Evaluation of the glass particles and the index matched fluid

Some important work had already been completed when we took part in the project, and therefore some of the premises for the experimental work were already laid. The glass particles that would be used inside the inspection tank had been selected, and the index-matching fluid had been matched with these glass beads (particles) at 594nm. The reason for matching the fluid to the glass particles was to visualize the movement of a few painted individuals inside the total particle mass by a fast video camera. The tank would be several particles in depth (between the glass walls), hence the index matching would also reduce light diffraction from each layer and make it easier to holograph the particle mass. Two tanks would be built, one with inner dimension of 20mm and one 10mm wide. Please read Lie [in preparation] for more information about the tank specifications. The index matching fluid would enable us to send light through the tank medium without much distortion (from walls or particles) and monitor the opaque particles. This would be far better than imaging only the reflected light from the outer side of a mass of non-transparent particles. We should be able to see inside the volume of particles that were moving.

The refractive index of glass is wavelength dependent. Some of the reasons for choosing particles made of glass were; easy to apprehend, transparent within the visible light spectrum and it is chemical inert. They would match well with the refractive index of the walls of the inspection tank, which would be made of window glass due to its transparency and accessibility. This was also an advantage for optical measurements.

Particles with a diameter of 0,5 and 1mm had been evaluated and discarded due to the presence of too much air bubbles and other imperfections. Larger particles with a diameter of 2mm were chosen instead (Figure 19). While the smaller glass beads had a lot of air inside, the beads with 2mm diameter had only a few air bubbles on the surface. The 2mm beads had a better circular curvature than the discarded ones.

Figure 19 Two particles types that was evaluated for use in the experiment. Left particle is 2mm and the one to the right is 0,5mm in diameter.

The fluid had been tested to match the refractive index of one of the particle of 2mm at a wavelength of 594nm. This wavelength had been chosen earlier, and a laser with

this wavelength had been apprehended. The matching fluid consisted of a mix of two chemicals delivered by the German company Sigma-Aldrich Chemie Gmbh. The two chemicals were

20 l Benzaldehyde (extra pure)
      Formula C_7H_6O
Refractive index 1.544 – 1.546 (higher than glass)
"Colourless, air sensitive, a component of odor of cherries, almonds",
[http://chemfinder.cambridgesoft.com 03.04]
"Moderately toxic",.Prof..T.Barth, Chemistry Department, University of Bergen;

10 l Cyclohexanon (extra pure)
Formula $C_6H_{10}O$
Refractive index 1.424 (lower than glass)
"Flammable"   [http://chemfinder.cambridgesoft.com 03.04]

The basic idea on how to find an appropriate combination of the two chemicals to obtain an index match between fluid and the glass pearls is illustrated in Figure 20. A single glass particle was positioned inside a fluid sample, on top of a metal screw.
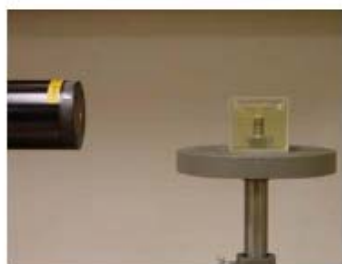
Figure 20 Laser beam hitting one particle in an index matching fluid.

The collimated output from a yellow laser was adjusted to illuminate the edge of the particle and then illuminated a sheet of paper. The transmitted image could hence be evaluated. If the transmitted beam was spread diffusively across a large area, see Figure 21, this meant that the fluid's index of refraction was different from the pearl inside. Our external supervisor Dr. Petersen, tested a lot of different mixing rates and found the best ratio to match the refractive index of the fluid to the glass beads.
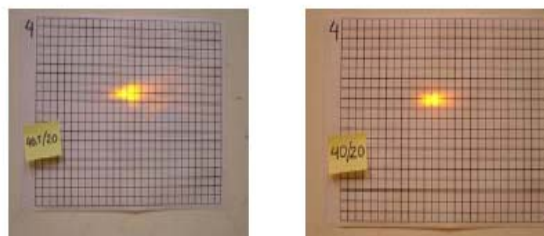
Figure 21 Diffracted beam from the laser hitting the edge of one particle in an index matched fluid.

The specific ratio of Benzaldehyd to Cyclohexanon was noted and the refractive index of the fluid was later measured at the Chemistry department at the University of Bergen by Dr. Petersen, with a high degree of accuracy to be
$1,5122 \pm 0,001$

This number represents with good precision the refractive index of the fluid measured. The same mixing rate would be used in all later experiments, but the uncertainty of the index matching will naturally be larger due to variations in particle quality. It is interesting to note that the refractive index of the particles $n_{particles}$ is found to be 1,51. The particles could therefore be made of "Zinc crown" glass, which has approximately the same refractive index around 589nm, as seen in the table below. The index of refraction for Nitrogen is also included in the table below. This gas will be used instead of air, as the flow in the tank would be a closed loop due to the fluid's sensitivity to oxygen. The fluid crystallized quickly in air, so pure Nitrogen gas would be pumped into the system to remove as much oxygen as possible before the experiments started. Gases arising during oxidation would be unhealthy, and our laboratory is not equipped with enough ventilation for hazardous gases. If the system would not prove properly airtight to these solvent fluids, the duration time of the experiments would have to be reconsidered.

	0,434 μm	0,486 μm	0,589 μm (Na)	0,656 μm
Zinc crown	1,528	1,523	1,520	1,517
Quartz glass			1,544	
Flint glass			1,62	
Nitrogen	1,000	1,000	1,000	1,000

Table 6 Refractive indexes of different glass types at different wavelengths [Weast 1985].

2.5.1 Recording a hologram with particles in fluid

The glass particles came without any documentation, as they had not been applied in scientific research before. Irregularities existed among the 2 mm pearls, and not all of them could be used as the problem with air bubbles made some particles white (diffuse light in all directions) and non-transparent. To see how much scattering in different directions we could expect, a glass container was filled with particles and the index-matched fluid, and photographed as seen in Figure 22.


Figure 22 Transmitted and scattered light through particles in fluid, seen from above to the left. A glass container in white light conditions (notice the black tape behind it) is displayed in the image to the right.

As the figure shows, there was quite a lot of scattered light. The fact that one could see all the particles was not positive either. Too much diffraction due to a large refractive index difference between particles and fluid would reduce transmitted intensity (object wave) and make it more difficult to do observations inside the particle mass.

The idea behind the index-matching fluid was to eliminate most of the scattering of light from the glass pearls. By painting some "tracking" glass particles and making these non-transparent, these could be visualized inside the "mass transportation" of glass particles moving along the flow. It would be interesting to make a hologram of the light scattered from the side of the container. Only the scattered light, arising from single or multiple scattering inside the glass container would be imaged. The collimated output of a laser at 594nm was directed parallel to the hologram film, through the container as shown in Figure 23.

Some parameters of the set-up are listed below:
Laser   He-Ne at 594nm
                     Reference beam ~ 0,70 [μW/cm^2]
(Adjusted to be ~ 4 times as strong as object beam)
                     Object beam ~ 0,18 [μW/cm^2] (estimated from object)

Film   BB640 (pan chromatic)
                     With bleaching, the film require ~ 100 [μJ] exposure
Exposure time ~ 2 min (Required exposure / tot. intensity ~ 112 seconds)
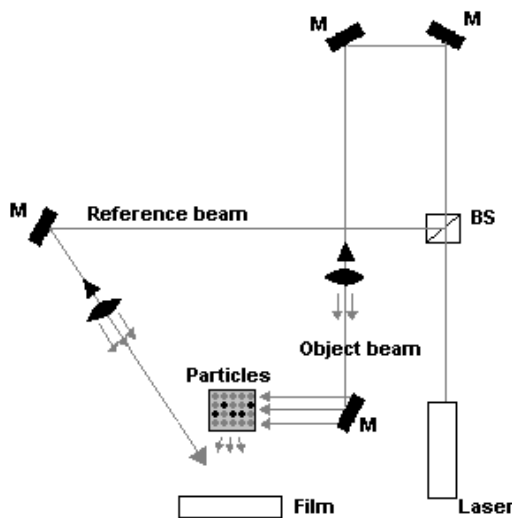
Figure 23 Set-up for making an off axis transmission hologram of particles.

M – mirror
ES - Electric shutter
MS – Microscope objective
BS – Beam splitter

The film was processed and resulted in an good hologram, although the unmarked beads were partly visible. An image of the hologram is shown in Figure 24.
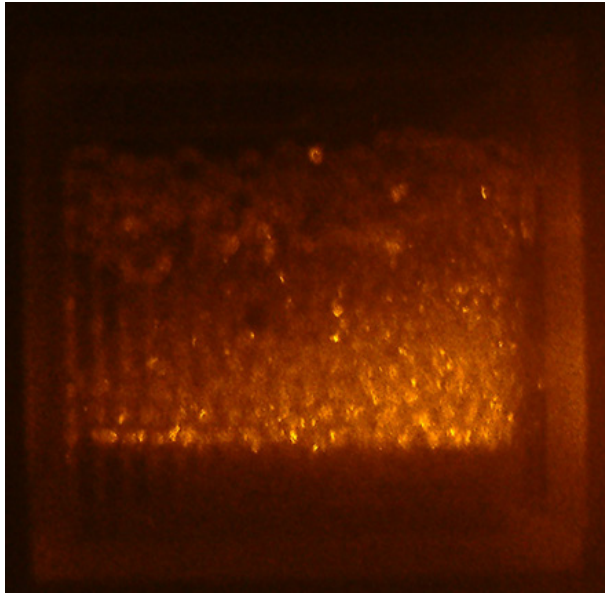
Figure 24 A hologram of glass beads in index matching fluid. Recorded and imaged with a laser at 594nm for best transparency.

Discussion

The glass container was not entirely filled with index matched fluid at the time this hologram was recorded and therefore the uppermost particles were exposed to air. The difference in refractive index between these particles and their surroundings are therefore larger than the ones in fluid. Notice that the beads at the top seem larger and are more visible. The fact that one can see the surface of each particle would later be used to visualize the different layers. The recorded hologram appeared bright and with good depth, but unfortunately this picture does not fully reflect this quality.

3 Preliminary experimental work

3.1 Bacteriorhodopsin

In April 2003, we decided to purchase a BR film from Munich Innovative Biomaterials Gmbh (MIB). The decision was easy to make, as they were the only company that sold BR films on the open market. Other groups researching or studying Bacteriorhodopsin properties have joined up with biochemical companies or biomaterial research organizations who can supply them directly with their biological material. For real-time holography purposes a BR films was the best option for us. It was reasonable to purchase, we needed no extra equipment and we did not have to make a C++ program, as was the case with digital holography. The film we acquired had the following specifications:

Article No.	V11S3.5
Description	D96N, 3.5 Slow
Refractive index	1.45 – 1.55 [Wolperdinger 2004]
BR layer	80μm - 100μm
Price	662 Euro

The specifications tell us that it has an optical density (OD) of 3,5, which is very dense. It means that the emulsion is packed with light sensitive molecules and therefore can contain high level of information. This was also the reason for choosing this particular film instead of less optically dense materials of the type D96N. Bacteriorhodopsin films are available with OD ranging from 1 to 5 at increments of 0,5, depending on the thickness of the Bacteriorhodopsin layer (30 – 100 μm). The downside of an optical dense media is that it requires an increased amount of laser power. This later proved to be unfavourable as our project has a limited amount of lasers (the strongest being a 20 mW 633 nm He-Ne). The optical density of 3.5 is in its initial form, and is valid for a specific wavelength within the 450-650 nm range. Probably it is given for the maximum absorption wavelength at 570 nm.

The transmission T, would then be:

$$D = \log\left(\frac{1}{T}\right) \Rightarrow T = \frac{1}{10^{3,5}} \approx 0,03\%$$

A test beam were applied to the film, giving a suggestion of its density at 633nm:

$$I_i = 2,05mW$$
$$I_o = 0,016mW$$

At normal incidence the reflection from air to glass at the front of the film and glass to air at the back plane of the film, is given by Fresnel's equation:

$$\Re_{front} = \left(\frac{n_1 - n_2}{n_1 + n_2}\right)^2 \approx \left(\frac{1,0 - 1,5}{1,0 + 1,5}\right)^2 = 4\%$$

$$\Re_{back} = \left(\frac{n_1 - n_2}{n_1 + n_2}\right)^2 \approx \left(\frac{1,5 - 1,0}{1,5 + 1,0}\right)^2 = 4\%$$

Subtracting 7,8% reflection loss ($0,96*0,96 \approx 0,9216$) from the two sides, an approximate OD becomes:

$$I_i = 2,05 * 0,92 = 1,89 mW$$

$$T = \frac{0,016 mW}{1,95 mW} \approx 0,85\%$$

$$OD = \log\left(\frac{1}{8,5*10^{-3}}\right) \approx 2,1$$

This shows that the film have an optical density of about 2,1 at 633 nm. It was also tested for yellow light at 594 nm with a lux-meter. This resulted in an OD of:

$$I_i = 0,92 * 2,0*10^3 lux \approx 1,84*10^3 lux$$

$$I_o = 1,2 lux$$

$$T \approx \frac{1,2}{1,84*10^3} \approx 6,5*10^{-4}$$

$$\Rightarrow OD \approx \log\left(\frac{1}{6,5*10^{-4}}\right) \approx 3,2$$

This is in general accordance with the absorption spectrum listed in Figure 6 by MIB. The BR film has a higher absorption coefficient at the yellow wavelength than at the red wavelength. The slow response time for the wattmeter LCD display and the lux-meter, made the uncertainty in these experiments quite large (5 - 10%), but the values indicate that the film would need high intensity in the yellow - green region to produce a hologram. It would however record a hologram faster in the emulsion at the yellow wavelength than at the red wavelengths.

MIB offer mainly two types of BR films (April 2003), Wildtype and D96N. The major difference, besides Wildtype being less expensive, is the "relaxation time range" (RTR). Both are produced in two types, Normal and Slow. These different types can presumable be made by adjusting the water content in the emulsion. The company use the "RTR" term as an estimate for the thermal back-conversion time, when 63% (1/e) of the molecules have returned to the initial state. The Wildtype BR has a typical RTR of a less than a second (Normal type) and about 20-30 seconds for the slow type. The D96N has a RTR of twice these numbers. In other words, it can hold the image for a longer time. This was also a good reason to purchase it. As the description indicates, we went for a slow version listed with a RTR of 40-80 seconds.

The RTR would also be tested in a few experiments. A first exercise showed that it could hold an image for quite some time, see Figure 26. The set-up consisted of two collimated beams of approximately equal strength illuminating the film from two sides (angles ~ 30°). One of the beams was then shut off, letting the hologram in the Bacteriorhodopsin film recreate it like diffraction from a grid. Both beams are illuminating a white screen after the BR film, as seen in Figure 25. It would be interesting to test the BR film with two of the lasers available, and hence both lasers were mounted on the optical table at the same time.
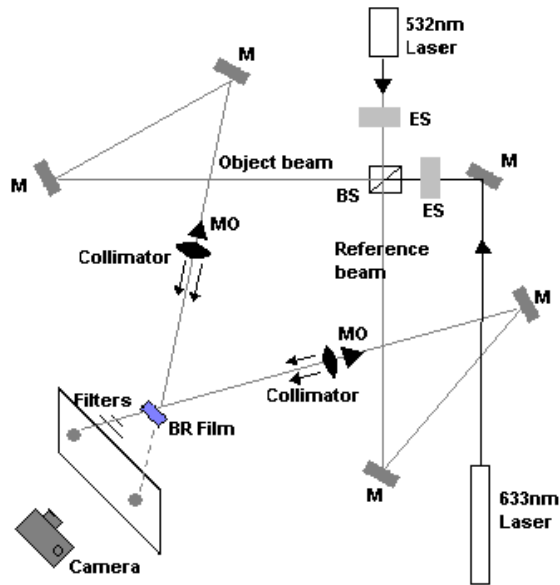
Figure 25 Set-up for making a transmission hologram using a BR film. In this set-up only the two waves are recorded (not any object).

Note that the recreated object beam is the one on the right, and that it is getting weaker with time. The reference beam is filtered to 0,125% to enable the camera to take the picture of both beams at the same time. The beam's evolution in time was illustrated by merging the different pictures in Adobe Photoshop.

Figure 26 The virtual images (holograms) are the ones to the right. These disappear gradually, due to thermal back-conversion. The reduced reference beam is the one to the left for both lasers.

Discussion

The figures suggest a different RTR for the exposure at 532 nm, than the one at 633 nm. This is not the case. If both exposures E (at the two wavelengths) had been optimal, and both holograms had been illuminated with a read-out beam of the same intensity and wavelength, then the hologram would have lasted equally long. What we can learn from these images is that the green read-out beam is faster to erase the hologram, as the BR film is more sensitive to this colour. The set up had to be adjusted to fit each laser, and the intensities for each experiment were also different.

A distinct feature of the green laser revealed itself during the test. A master student in experimental optics at our group had also discovered the same property two years before [Blom 2002]. The virtual object beam consists of interference fringes, as the pictures of the green diffraction shows. The film had only been exposed once, so this was unexpected. The reason for it is a troublesome mode-hopping feature of the laser. Of course this was very unfortunate, as it is the strongest laser our optics group possess (adjustable up to 50mW). The mode-hopping property implicates that it transmits light at two or more wavelengths. Thus the hologram will consist of two or more images, interfering and creating fringes. A multi exposure feature, actually, that shows that the film can handle successive exposures. This was a good start, as our goal was to use it in real-time holography (confer to section 2.4).

More information about the film's properties was needed. How fast did it react to light and what was the best way to erase the previous image before making another hologram. The film did not come with any supplemental information other than what can be found on the company's home page [http://www.mib-biotech.de, 04.02.04]. The BR films sold from MIB seem to be intended for research and business purposes that already know what they purchase and how to implement it. We needed more information about our BR film such as; bleaching rates, diffraction properties and violet light sensitivity (erasure light). Knowing these properties would help finding optimal exposure times and contribute to us making better holograms.

3.1.1 Exposure characteristics

The BR film's time response to different intensities was tested with the green 532nm laser. It was a simple set-up, with the wattmeter positioned straight behind the film to measure the transmitted intensity. From the graphs in Figure 27 it was obvious that the stronger the write beams were, the better. The objective for the thesis is an investigation of hologram techniques to visualize particles in flow. Then it would be of great importance to keep the exposure times as low as possible. From the graphs it can be seen that high intensities bleach the film much faster to a higher modulation level. Other research groups report using pulse-lasers [Bouevitch and Lewis 1995] and very strong argon-ion lasers (84 mW/cm^2 at 514,5nm after collimating) [Downie et al. 1996] to benefit this quality of the medium. A strong laser source yields fast imaging and improved quality.
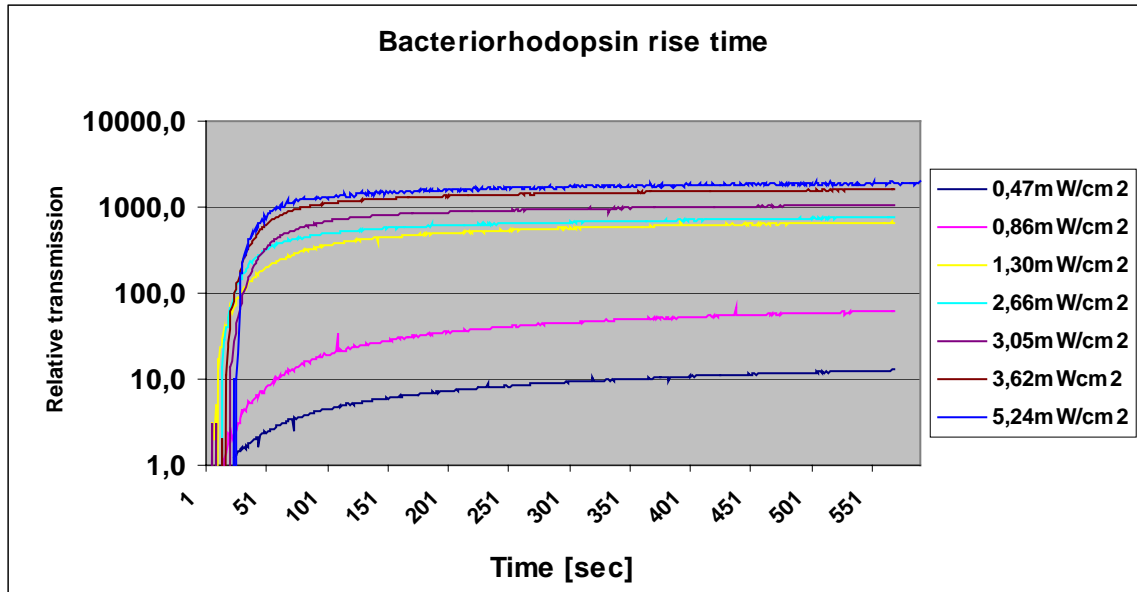
Figure 27 Exposure characteristics for a BR film of type V11S3,5 from MIB.

3.1.2 Thermal back conversion

The second feature to be quantified was the thermal back-conversion. It describes how the molecules behave after exposure to a strong laser and thermally return to the initial B-state. Two lasers where used. The output from the our green laser at 532 nm was tuneable and functioned as a bleaching/write beam at different intensities, while a collimated beam from the yellow laser at 594 nm was used as a read-out beam at a weak and constant intensity. The read beam was illuminating the film from a different angle than the write/bleaching beam and could be separately focused at a wattmeter, so its transmitted intensity could be logged. The read beam was almost completely absorbed when the film is in its B-state. Illuminating the film with the strong green bleaching light will then photochemically induce a transition of molecules where more and more molecules go from B to M-state making the film more transparent for all light at these wavelengths (less absorption). The film was exposed for a minimum 3 minutes of bleaching beam at different intensities before the green laser was cut off. The yellow read out beam would then display how more and more molecules returned to the ground state, absorbing more of the yellow beam as a function of time. The parameters were:

Yellow laser
I_{read} = 0,109 [mW]
$A = \pi*(1,2cm/2)\wedge2 = 1,13$ [cm^2]
I/A = 96,4 [μW/ cm^2]
Green laser
On > 3 min before logging
I_{write} = 35,2 / 28,16 / 6,30 / 2,70 [mW]
$A = \pi*(1,9cm/2)\wedge2 = 2,84$ [cm^2]
I/A = 12,4 / 9,9 / 2,2 / 1,0 [mW/ cm^2]
Wattmeter
20 [μW]
Picolog
2000 samples
every 100 [ms]

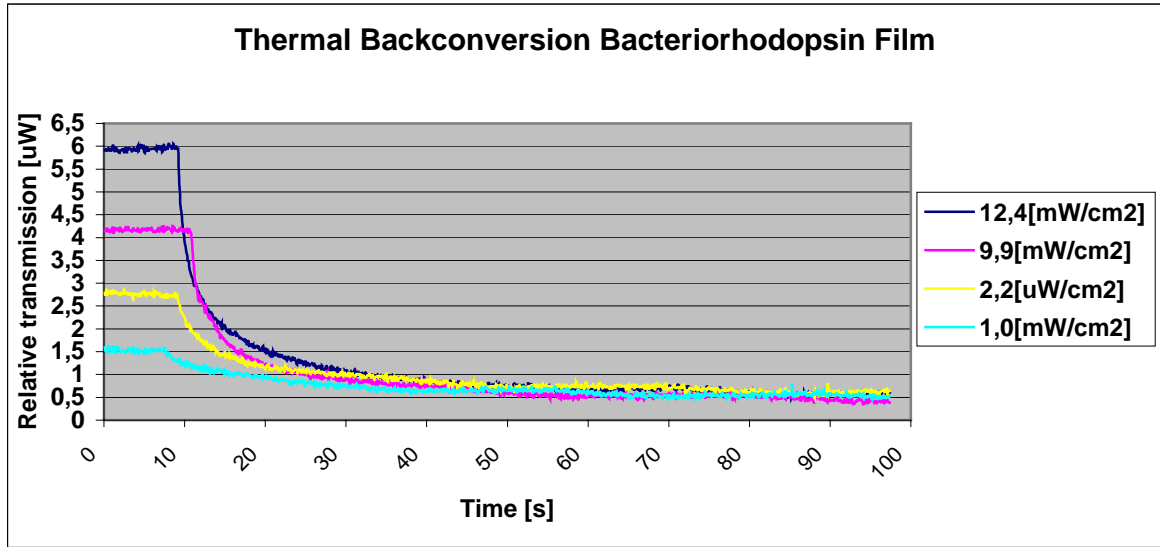A plot of the film's characteristic is shown below.

Figure 28 Thermal back conversion from M to B state for our Bacteriorhodopsin film.

The film has a relative short relaxation time, compared to the listed values of 40-80 seconds. By then 63% (or 1/e) percentage of the molecules should have returned to the initial state and ready to absorb yellow, red and green light. From the graph it can be seen that this only takes about 10-15 seconds after the strongest write beam, while the same reduction first occur after 50 seconds with the low intensity (1,0 [mW/cm^2]) exposure. All curves should descend towards the zero line with time, but instead they all approach an asymptotic level larger than zero. This indicates that, ideally, a weaker read beam should be applied. The nature of the film and another important result was acquired nevertheless; a light source to erase the image would prove useful if we should benefit from low intensity recordings. This source would hopefully enable us to erase the previous image completely and also faster. A light used to erase a hologram would need to transmit light only in the 400 – 450nm region according to Figure 6. The violet light source would not need to be a coherent laser, as it's only purpose would be to photochemically convert the BR molecules back to the ground state.

3.2 Violet light source

The spectral radiation from a light source will to the most extent be given by the burning arc's temperature by Planck's law:

$$u(f,T) = \frac{8\pi h f^3}{c^3}\left(\frac{1}{e^{\frac{hf}{k_B T}} - 1}\right)$$

(3-1)

Higher arc temperature increase the peak emission frequency f_{max}, and therefore lower the emission wavelengths $\lambda = c/f$, according to Wien's Displacement law:

$$f_{max} \propto T \Leftrightarrow \lambda_{max} \propto \frac{1}{T} \qquad\qquad (3\text{-}2)$$

Stefan's Law of Radiation also tells us that the power radiated goes as:

$$P = \sigma T^4 \qquad\qquad (3\text{-}3)$$

These formulas were in the back of our minds while searching for possible low-cost violet light sources. Different sources were tried. Most of them were short misadventures, and could not be used for our purposes. The following sections are included as they can be informative reading.

3.2.1.1   Halogen light sources

A halogen lamp was tried as violet light source. The output was filtered at 419nm to convert the BR molecules to the B-state. As the halogen source is reasonably hot and the violet filter does not tolerate much heat before it is destroyed, an IR filter was positioned in front of the 419nm filter. The two tested halogen lamps were:

Luminance Quadrostar Halogen Spot max20W, type QR-CB 35 (Philips bulb at 35W)
Luminance Quadrostar Halogen Spot max35W, type QR-CB 35 (Decostar 35S bulb at 35W)

Filters:
Blue filter provided by Balzers
        419nm B-40 9
IR filter provided by Melles Griot
Heat absorbing mirror type KG 1
Prod nr. 03 FCG 163

We used the 20W halogen lamp as an erasure source and tried to establish the diffraction characteristics of the BR film. During these experiments it became clear that the film did not return to its initial B-state after exposure to our violet erasure light. None of the measurements could be reproduced after some time, due to high saturation. Focusing the transmitted violet light onto the film plate was not enough. The intensity was too weak. The erasure time being more than 30 seconds was already too long. A light spectrum was taken, as shown in Figure 29. The filter works as it should, but the halogen output at the required wavelength is not high enough.
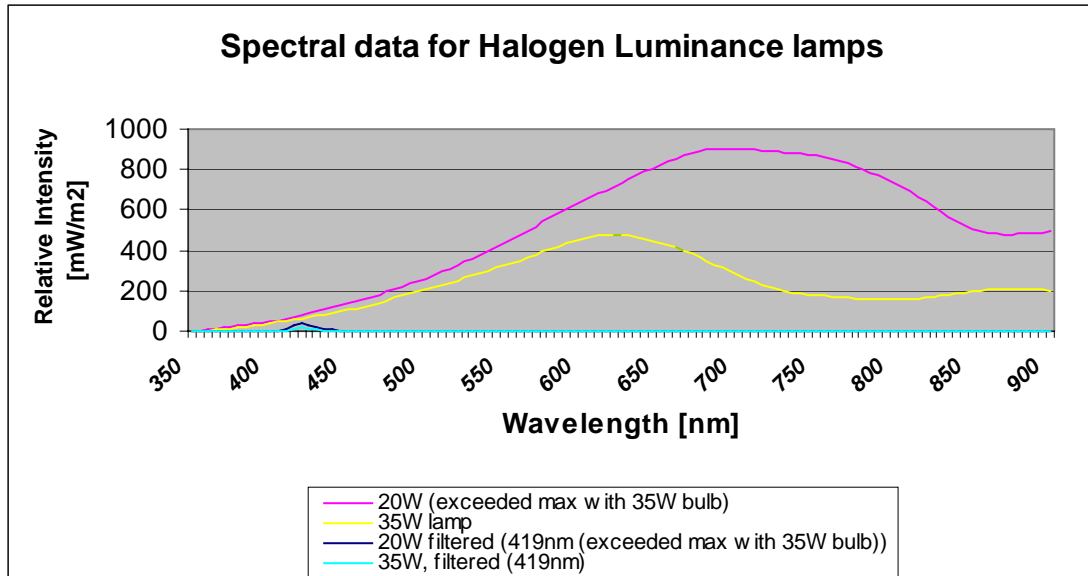
All spectral measurements were performed with:
Trios Optical Sensor
Type   RAMSES-VIS
Serial-no#   010-03-810C
Sensitivity   5 [nm]

Spectral data for Halogen Luminance lamps

Legend:
- 20W (exceeded max with 35W bulb)
- 35W lamp
- 20W filtered (419nm (exceeded max with 35W bulb))
- 35W, filtered (419nm)

Figure 29 Intensity measurements for two different Halogen sources.

The project did not have an alternative light source available, and the only Xenon lamp at the optics group was in use. A Xenon lamp would have been a powerful source, but it was too expensive to purchase a new one.

3.2.1.2   Comparison of filtered light sources

Car lights can be pretty inexpensive. Some of these have a brightly bluish appearance to the human eye and were thought maybe to also radiate in the violet spectral range, which is not more than ~30 nm apart. Probably they are of the Xenon gas discharge type, which is quite expensive but can provide "up to 300% more light than ordinary halogen" [http://www.torgersenbil.no/Xenon.pdf, 11.02.04]. These lamps will also require additional electronics to work, due to the high voltage needed to ignite the Xenon gas inside the bulb. The alternative bluish car lights are the specially made white and blue halogen types. Of the latter, two types were acquired for testing. The data were

"Cool blue" OSRAM halogen bulb
        60/55W (far/driving light) 12V
+10% blue (4000K) Bilux H4
        Price: 198 Nok/pc

"Mega blue" halogen bulb from Biltema
        60/55W (far/driving light) 12V
        Art. No#   35-556
        Price: 98 Nok/2 pcs

Since these bulbs are intended for automobile use inside a light reflector, a basic reflector was made. The weak power output of the halogen sources was still in mind. As much light intensity as possible should be focused at the film. The reflector was made from a steel tube and worked quite well. It was mounted to fit onto our optical table. A picture of the lamp is shown in Figure 30.

Figure 30 The design for a reflector made of a metal tube, to converge the light beam and prevent stray light.

At the same time, a Radium 75W blacklight was tested. This bulb is intended for entertainment purposes, and emit at or near the UV wavelength. Its main purpose is to excite fluorescent materials. The tested lamp was only a "fake" blacklight, meaning it has a normal light bulb but use a filter to absorb all wavelengths above UV. The emitted light spectre might still have some intensity around 415 nm, although it seemed pretty weak when we visually inspected it through the 419 nm filter. The spectral emissions from these light sources after filtering with the 419nm are shown in the figure below.
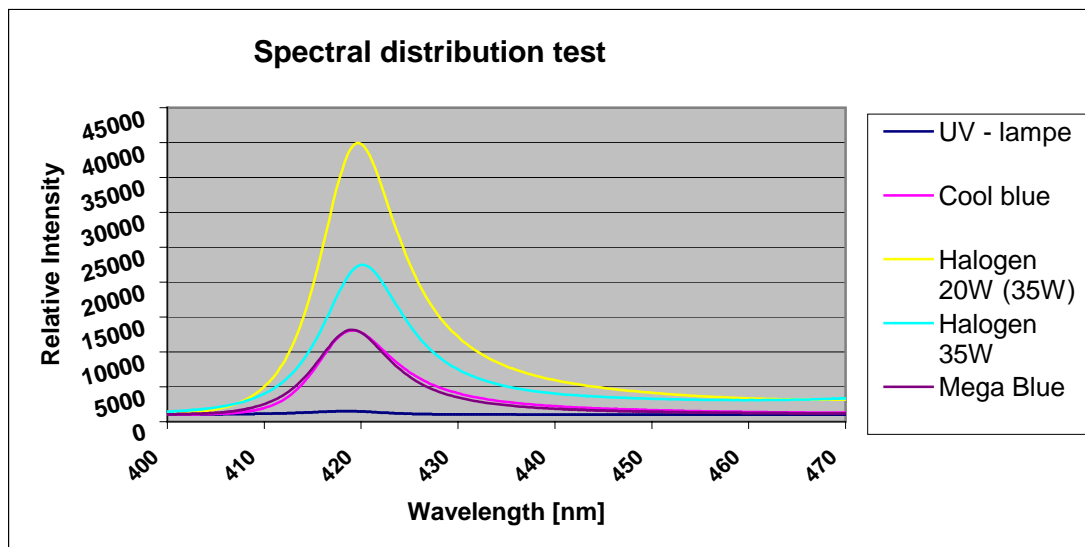
Figure 31 Intensity distributions for five filtered light sources at 419nm.

Discussion

The graph shows that the strongest of all light sources are the halogen lamps. The best appear to be the "boosted" 20W halogen lamp with a 35W bulb. This was bad news for the two front lights for cars. They could not be used. It reflects the problems using your eye as an objective tool. The eye is definitely not objective, it follows its own logic. The rods and cones in our eyes have followed evolution to make us see better in the centre of the visible spectrum. The different colour sensitive cones in the retina of

the eye are red (64%), green (32%) and blue (2%), according to C. R. Nave [http://hyperphysics.phy-astr.gsu.edu/hbase/vision/colcon.html#c1, 10.02.04]. The blue sensitive cones are more light sensitive than the two others but less in numbers, hence our eyes have peak sensitivity at the yellow-green wavelength of 555 nm (also the main wavelength of light emitted by our sun). This explains why car lights do not need a lot of intensity in the blue wavelength range to appear bluish to our eyes.
In addition a small, but very important comment was missed on the package of the Osram halogen bulb. It said "UV stop". This implies basically that the glass has been coated with a filter to stop most of the light probably up to 400 nm. As filters seldom have an absolute cut-off transmission response, this implied that most of the wanted violet light also had been removed.

3.2.1.3   Light emitting diodes

A time consuming search for light emitting diodes (LEDs) begun. Diodes are commercial available in a wide range of wavelengths, and they emit in narrow bands of light. It seemed very suitable as an erasing light source. Searching for diodes around 400 – 420 nm revealed that this is a specialized market. Most available products are in the red, green, blue or white category. They all emit in a very narrow bandwidth and could not be used for our purposes. The strong blue and white LEDs are the newest on the market. An American company called ETG was found. They sell (Nov. -03) relatively strong LEDs at 420 nm, which should work for us. Please refer to Figure 6 for the film sensitivity at this wavelength. The specifications for the diodes were

Type   ETG-5AX-420-15
Material   Ga(i)N
Price   50$ for 30pcs

At 20mA the typical characteristics are:
Power dissipation   120mW
Peak emission wavelength   420nm
Forward Voltage   3.6 – 4,0 V
Luminous Intensity   1000 mcd
Viewing angle   15 deg

3.2.1.3.1 Diode circuit design
While the LEDs were being shipped an electronic circuit that could use 9 diodes was designed. 9 LEDs was an appropriate number of diodes to mount in close vicinity, as they all would most likely hit the 1,9 cm circular film plate instead of illuminating other parts of the room. The diodes had a very narrow illumination angle, a feature that was appreciated. The design of the electronic circuit was based on a fixed supply voltage at 5V. To supply 9 diodes with ~ 5V, the circuit would have to be a parallel connection. This means that all diodes will have the same voltage across its junctions, but the current may be slightly different. The LEDs will therefore emit at slightly different intensities. This was not a problem as our objective was the total intensity. We did not possess a power supply with an output of ~45V as a serial connection would require. A resistor to specify the current was calculated. This had the value (using Ohm's law)

$$R = \frac{U}{I} = \frac{E - V_{LED}}{I_{parallel}} = \frac{5V - 3{,}8V}{20*10^{-3}A} = 60\Omega$$

A standard resistor of $62\Omega \pm 2\%$ was applied.

Per Heradstveit at our Department of Physics and Technology drew the paths for the circuitboard using Orcad software being provided a drawing from us, and soldered the LEDs and resistors on a circuit board. He also provided a tuneable power supply, which made the output from the LEDs adjustable. The circuit is shown in Figure 32.
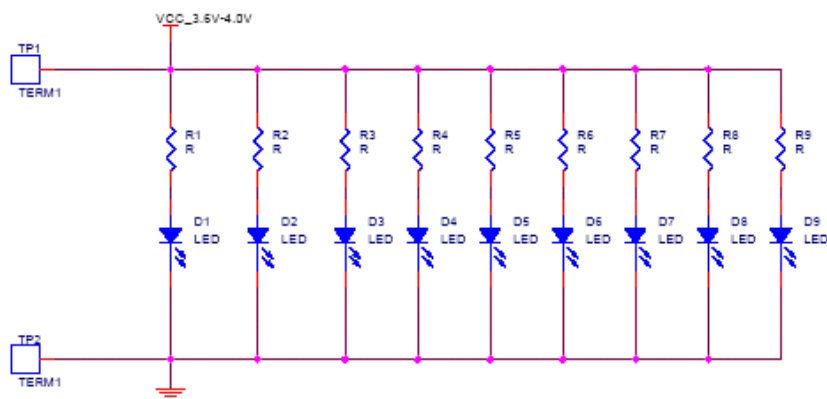

Figure 32 Circuit design for the diode LEDs.

The first LEDs to arrive had the wrong specifications. The cause of this is unknown, but maybe ETG supplied us with another type of their products (ETG-5AX-440-15) by a mistake. The measured peak emission from these diodes was about 445 ±5 nm (see Figure 33), and would have photochemically induced BR molecules to both the B and M state as both have absorption at this wavelength.
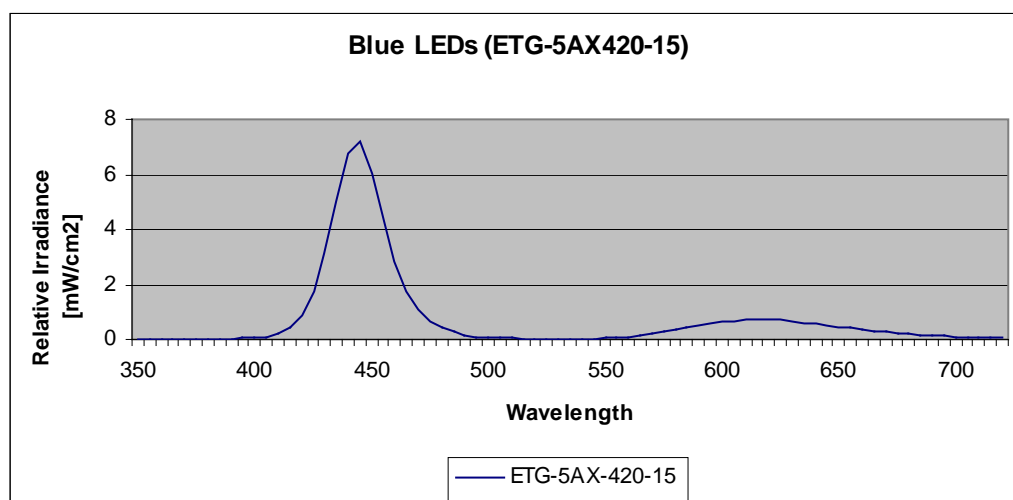

Figure 33 Spectral irradiance distribution for ETG-5AX420-15.

Some weeks later the correct shipment came in. These diodes had a peak emission at 410 nm, but were not provided with any datasheet or listed on the ETG's website

[http://www.etgtech.com/products.htm, 01.01.04]. They could still be implemented in the diode circuit, as the supply voltage was tuneable. The spectral emission at 410 nm as seen in Figure 34 from these diodes, was much more appropriate for our experiments.
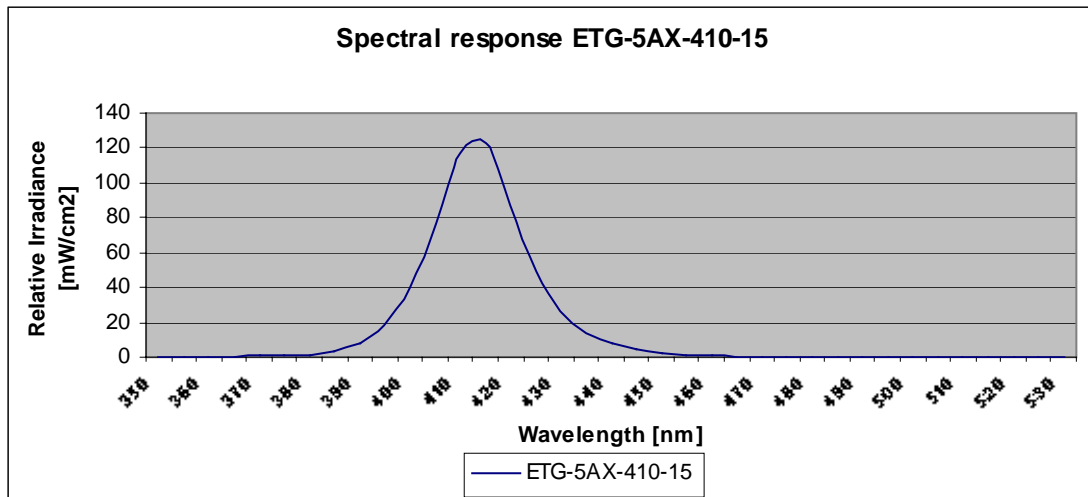

Figure 34 The spectral emission from correct diodes, with listed peak emission at 410nm.

3.2.1.4   Final comparison of violet light sources

To evaluate the new diodes versus the first shipment (5AX-420-15) and the halogen spotlights, an irradiance measurement was taken. This was only to get a conversion factor, which is given in the table below. Weighting the spectral distributions that had been taken earlier would yield an approximate comparison to see if the new diodes were the better ones. The factor was measured in luminous flux. The halogen spot was filtered (no applied IR filter) at 419 nm before illuminating the lux-meter. Some parameters were:

Distance to sensor   10cm
Sensor   UDT Optical Power Meter 371

	Peak emission	**Measured [lux]**	**Conversion factor [lux/rel.Intensity]**
5AX-410-15	122,8921	131	1,065
5AX-420-15	7,2114	120	16,64
20W Lamp:	708,4278	354	0,499

Table 7 Conversion ratios for the different light sources.

The conversion factor was multiplied with the measured values from before and a spectral distribution for the leds and the halogen source with highest intensity could be plotted. This is illustrated in Figure 35.
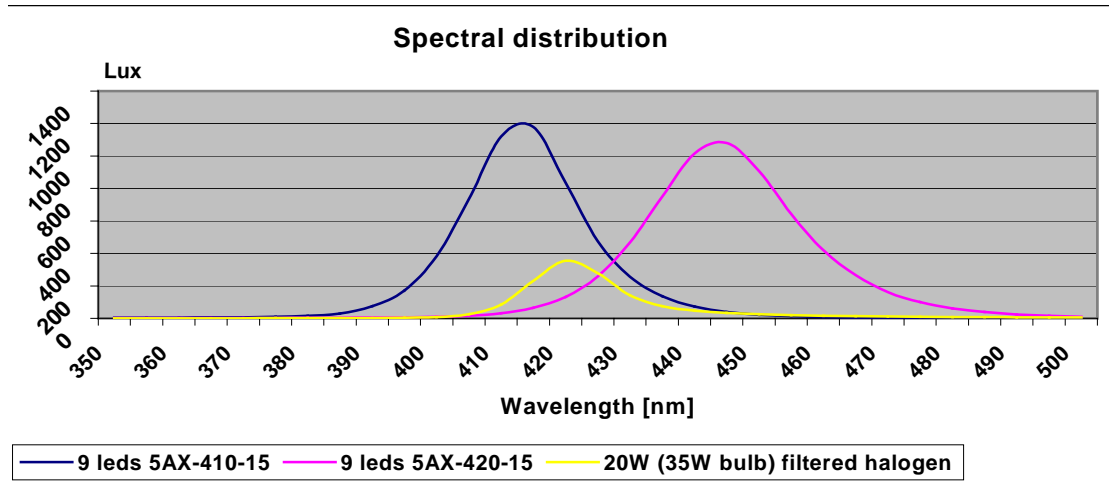
Figure 35 Diode lamp (9 leds) intensity compared to halogen source.

Note that the halogen lamp has a larger viewing angle than the diodes, and were not focused at the lux-meter (as it was tried in the BR set-up earlier). This would have provided a bit more intensity. However, the irradiance sensor is less sensitive to light at 410 nm than to light at higher wavelengths while the BR film is more sensitive to a light source at 410 nm. In addition, the diodes at 410 nm proved to emit at a higher intensity, as shown in Figure 35. The conclusion was that the new diodes were the better ones.

3.2.2 Thermal decay vs. diode erasure light

To compare the new diode lamp with earlier measurements, the exact same test that had been applied to find the RTR times was used. The yellow read beam was filtered to emit the same irradiance, ~ 96 $\mu W/cm^2$, and the same two lasers were used. The decay responses measured earlier were now compared to an exposure where a violet erasure light was turned on at the same time as the green bleaching beam was turned off (marked with "VIOLET" in the diagram). Note that the two higher saturation measurements have been shifted along the time scale to make it easier to compare the back conversion. The graph is shown in Figure 36.
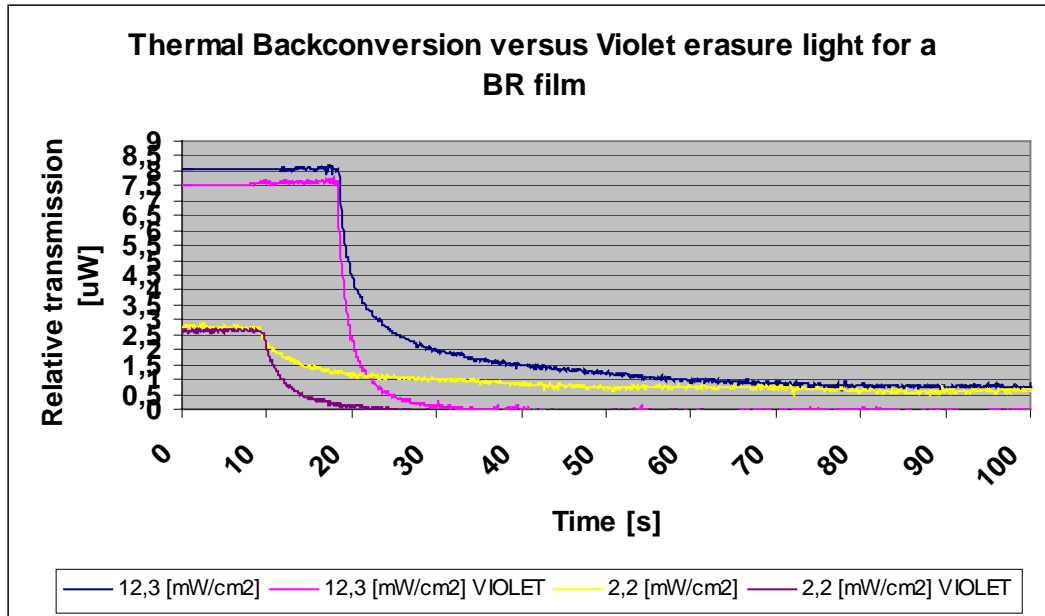
Figure 36 The effect of violet diode source, after saturating the BR film at two different bleaching ratios.

Discussion

The blue erase light makes the molecules return to the initial state faster than it would have done thermally and manage to suppress the read beam completely. This proves that the violet source is strong enough for our purpose. The RTR is still a bit long compared to the listed <50ms, but 2-3 seconds (purple line, called violet light) is much better than the 22-23 seconds for a 63% back conversion at the similar exposure with 2,2 mW/cm^2 (yellow line). For the higher saturation level, there was less reduction of RTR time by using violet erase light. The RTR time went from typically 4,8 seconds to 1,4 seconds for 63% to convert to the ground state. The erase light was still an improvement. Note that holograms can still be viewed although 63% of the molecules have returned to the ground state. Experiments performed at later times revealed that holograms normally lasted a minute or more. This depended on the read-out intensity as well as the BR RTR time.

3.2.2.1   Diode output

The damage threshold of the BR film is typical ~ 0,5-1 W/cm^2. To estimate the luminous intensity from the lamp (9 diodes in total), it was necessary to convert the listed 1000 mcd to watt. First, one can convert candela to lumen, then one can convert lumen to watt by conversion tables. Lumen is a "luminous strength" that has been weighted to the human eye's sensitivity so 1 lumen is equally bright at all wavelengths. Candela is defined as lumen per steradian solid angle.

$$[cd] = \frac{[lm]}{[sr]}$$ (3-4)

To find the solid angle it is necessary to use the listed total angle 15° (0,2617 radians), to calculate the number of steradians, w. Solid angle is defined as area, A, divided by the square radius, r^2.

$$dw = \frac{dA}{r^2}$$

(3-5)

$$w = \frac{\int\limits_{0}^{2\pi}\int\limits_{0}^{0,2617} r^2 \sin\theta d\theta d\phi}{r^2} = \int\limits_{0}^{2\pi}\int\limits_{0}^{0,2617} \sin\theta d\theta d\phi = 2\pi(\cos(0) - \cos(0,2617)) \approx 0,214[sr]$$

The luminous intensity for 9 diodes can be found:

$$I = 9*1[cd]*0,214[sr] \approx 1,93[lm]$$

To get an estimate for the intensity in watts, a conversion factor between lumen and watt is required. A table of these conversion factors is given below, and also plotted in Figure 37.

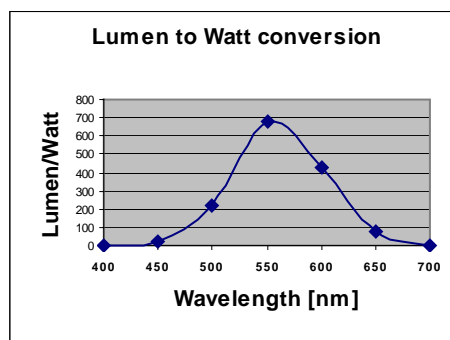| Wavelength [nm]	Factor [lm/W]
400	0,27
450	26
500	220
550	680
600	430
650	73
700	2,8

Figure 37 Lumen to Watt conversion.

The conversion numbers were taken from [www.photo.net/learn/optics/lensTutorial, 02.01.04]. As an estimate for our diode lamp, a conversion factor of 1,0 lm/W would be used. The power in watt was then given as:

$$I \approx \frac{1,93[lm]}{1,0\left[\frac{lm}{W}\right]} = 1,93[W]$$

If all intensity of the lamp hit within a circle of diameter 2 cm, the luminous flux [W/cm²] would approximately be:

$$\frac{I}{A} \approx \frac{1,93[W]}{\pi(\frac{2,0}{2})^2[cm^2]} \approx 0,61\left[\frac{W}{cm^2}\right]$$

This is very approximate value, and probably a bit large as well. The film has a damage threshold of ~ 0,5-1 W/cm^2, so some caution would be necessary. During the experimental work the lamp was never positioned closer to the film than 10 cm. At 10 cm distance to the emulsion the beam diverged enough to also illuminate the film holder.

3.2.3 Diffraction characteristics of the BR film

The most essential characteristic of a hologram concerning the brightness of the reconstructed image is the diffraction efficiency. To some degree it has been discussed in chapter 2.4. It represents the ratio of light flux in the reconstructed image to that of the incoming light on the film emulsion. For an ordinary hologram this property is fairly easy to test, since the emulsion layer has been developed and should therefore (ideally) not be sensitive to light any longer. The BR film will is light sensitive at all times. It would be a challenge to test our film in a proper manner.

The set up for the diffraction experiment is shown in Figure 38. Two beams interfere on the film from approximately the same angle (reference beam at ~ 33° and object beam at ~ 36°). The microscope objective has been positioned in front of the cubic beam splitter to increase the laser effect reaching the film. By avoiding one microscope objective for each beam in front of the film, there is less optic components in the set up, and less intensity loss (less reflected and diverged light). This is also the reason for the simple set up. After exposing the film with a chosen intensity, the "object" beam that is focused at the wattmeter is shut off by placing an aperture in its path. The reference wave will continue to illuminate the emulsion, now reconstructing the original object wave like it does in a normal hologram.
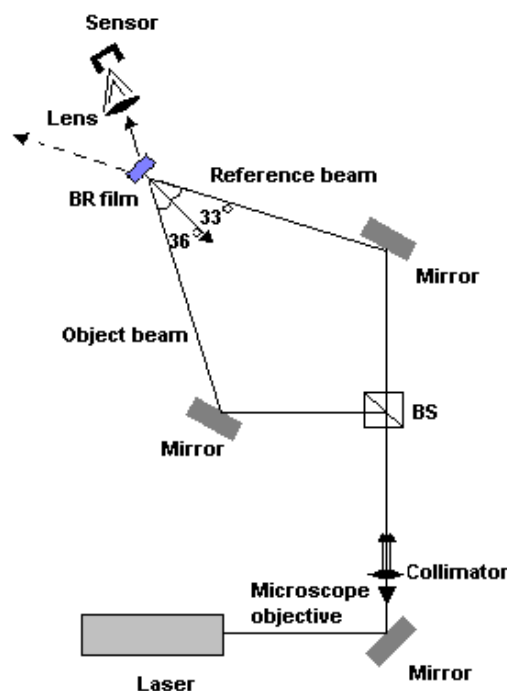

Figure 38 Set-up for the diffraction experiments (BR).

A manual read-out of the set up was tested first. It proved useless as the values on the LCD panel of the wattmeter changed to fast. Therefore, a logging software was implemented to measure the output of the wattmeter during a long session of testing. It will measure the diffracted intensity and save it for later analysis. The intensity measured by the wattmeter will be significantly different between bleaching (mW range) procedure and measuring the diffracted hologram (μW range). Only the diffracted intensity is of interest in this experiment, and therefore the power meter is adjusted to measure the diffracted light in a low intensity range (typically 20μW or 200μW). The logged values will therefore be saturated during exposure and suddenly drop when the object beam is turned off. Knowing the time interval between logging values will make it easy to predict the total exposure time, counting the number of saturated values. The crucial thing will be to evaluate the logged values at shut off time, as the film is in constant change in response to the incident light. The film emulsion will continue to bleach due to the strong reference wave, and the diffracted intensity will alter with it. The first logged values should, regardless of this dynamic behaviour, indicate a maximum diffraction at each exposure value (I*t), if the equipment is sampling correctly. The optical components used in these experiments are:

Laser   Melles Griot
          He-Ne   <30mW at 632,8nm
          Model   05-LHP
          Serial No.   03728J
Electronic shutter (use manual switch, open/closed)
Microscope objective:
Lens: Ealing, *10, focal length 16mm (0.17 NA)
Pinhole: ~15 μm
Collimator lens, focal length 50mm
Cubic beam splitter, 1,5 cm (non-polarizing)
Mirrors
Apertures
Double convex lens, focal length 17,5 cm
Metrologic Laser Power Meter (20μW / 200μW / 2mW / 20mW)
          Modell no. 45-540
          Serial no. 1437
Picolog logging software
          (Each sampling takes 30μs and is averaged)

3.2.3.1   The logging software

First diffraction experiments showed that the specifications for the Metrologic Laser Power Meter had to be found. The logged values proved to lag behind the diffracted input and had an exponential descend towards more stable values. All equipment has a certain transfer function, so this behaviour is normal. A few experiments were performed to find out how long time the output was lagging from the saturation condition, before reaching the new input value from the sensor. Almost the same set up as before could be used. By reducing the object beam and changing the film for a beam splitter, it was possible to log a saturated value that could cut to a low value in the μW range. The values used to test the equipment were approximately in the same range as the values to be measured later in the diffraction experiments. The stabilization times proved to be a bit different for different sampling times. These are

illustrated in the table below. Three different "drops" for 20 ms sampling time are shown in Figure 39 to illustrate the behaviour. The sensor was first saturated by a strong (mW) signal, then cut to be ~12 µW (200 µW range).

Sampling time	10 [ms]	20 [ms]	50 [ms]
Output stabilized in	150 [ms]	180 [ms]	450 [ms]

Table 8 Stabilization times for different sampling times using Picolog software.
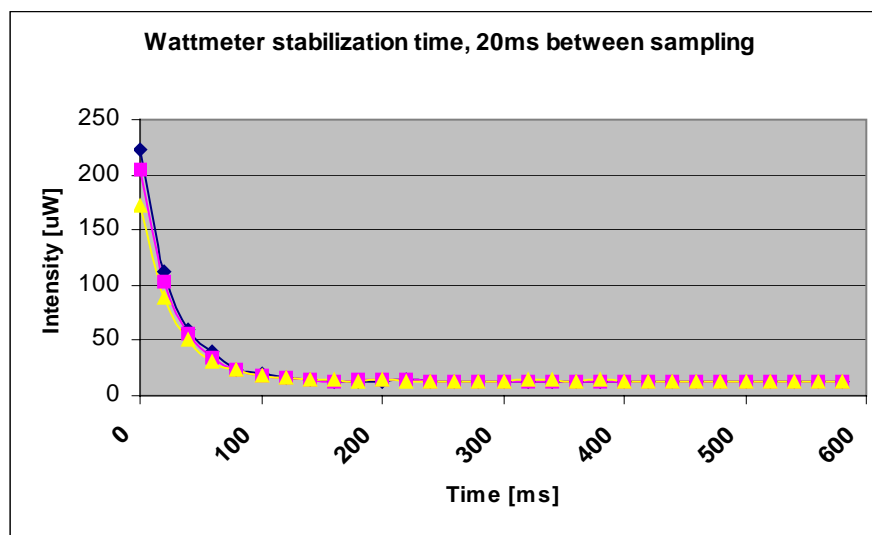
Figure 39 Check for the stabilization time of the wattmeter (20ms sampling). Three identical tests are displayed.

3.2.3.2 Bacteriorhodopsin diffraction experiments

Knowing how to choose a representative value from the logged values, the diffraction properties of the Bacteriorhodopsin film could be tested. The measurements were performed with these parameters:

Total number of sampling	30 000
Sampling rate	20ms
Wattmeter range	200 µW
Blue erase light	0,8 – 1,1 mW (measured inside film holder)
on for	>30s
Total write intensity	13mW / 5,8mW / 2,8mW
Beam diameter	1,3 cm
Beam area, A	$\approx 1,33$ cm^2
Filters	46,9%, 23,1%

Three different intensities were tested. The total intensity of both the reference and object beam was 13mW (full power), 6mW (48% filter) and 2,48mW (23% filter). It was expected that the film should have a diffraction peak at a shorter time for a stronger bleaching power. The diffracted intensity should then decrease towards saturation when increasingly more molecules approached the M-state. After some time it should have reached a steady state, when the thermal back-conversion matched the bleaching. The optimal exposure time should be dependent on the writing intensity. A large number of measurements were taken.

3.2.3.2.1 Theoretical considerations

To calculate the diffraction efficiency one need to know the percentage of light diffracted relative to the incoming read-out intensity. Instead of finding intensity loss for the read-out beam and the diffracted beam, the beams experienced almost the same optical conditions before they were measured. All measured diffracted intensities were focused through a convex lens before hitting the wattmeter, demonstrated in Figure 38. By focusing the reference (read-out) beam onto the wattmeter with the same lens, before starting the measurements, this intensity would represent the correct value, if only the reflected loss from the BR film front and backside were subtracted. To find this loss one can use the Fresnel equations. The loss at the boundary of air to glass at the surface of the BR film would be complicated to calculate due to the polarization direction of the laser was turned ~ 60° (to the vertical) in the set up used. The reason for turning the laser was to get an appropriate intensity ratio of the reference beam to the object beam. The non-polarizing beam splitter divides a different amount of intensity in the two directions (reference and object beam) depending on the polarization direction of the laser beam. The total intensity loss can be found as the reflectance R from the boundary, by the sum of the transverse electric (TE) and transverse magnetic (TM) component. Each reflectance has to be weighted by a sine and cosine factor (squared) to match the polarization angle α^i (60° in this case):

$$\Re = \Re^{TM} \cos^2 \alpha^i + \Re^{TE} \sin^2 \alpha^i \tag{3-6}$$

where each component can be found by:

$$\Re^{TM} = \frac{\tan^2\left(\theta^i - \theta^t\right)}{\tan^2\left(\theta^i + \theta^t\right)} \tag{3-7}$$

$$\Re^{TE} = \frac{\sin^2\left(\theta^i - \theta^t\right)}{\sin^2\left(\theta^i + \theta^t\right)} \tag{3-8}$$

The refracted beam angle being θ^t and the incident angle being θ^i respectively. The refractive angle can be found using Snell's law for refraction for a light wave travelling across a boundary of two different refractive indexes n. Also see Figure 40, where an incident ray of light is reflected and refracted by a boundary between air ($n_1 \approx 1,0$) and glass ($n_1 \approx 1,5$):

$$n_1 \sin \theta^i = n_2 \sin \theta^t \tag{3-9}$$

$$\theta^t = \frac{n_1 \sin \theta^i}{n_2} \approx \sin^{-1}\left(\frac{1,0 * \sin 32,99°}{1,5}\right) \approx 21,3°$$
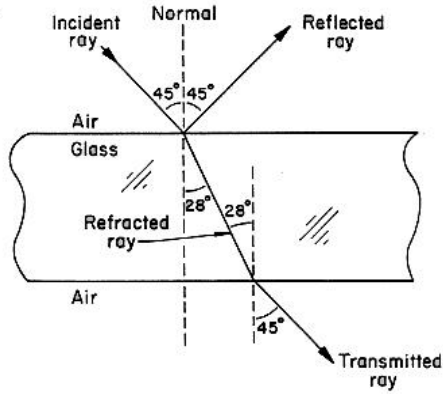
Figure 40 Light transmission and reflectance through a dense medium.

The reflectance component were:

$$\Re^{TM} = \frac{\tan^2[32,99° - 21,3°]}{\tan^2[32,99° + 21,3°]} \approx 2,15 * 10^{-2}$$

$$\Re^{TE} = \frac{\sin^2[32,99° - 21,3°]}{\sin^2[32,99° + 21,3°]} \approx 6,23 * 10^{-2}$$

This results in a total loss from the front glass of:

$$\Re = \Re^{TM} \cos^2 \alpha^i + \Re^{TE} \sin^2 \alpha^i$$

$$\Re \approx 2,15 * 10^{-2} * \cos^2 60° + 6,23 * 10^{-2} * \sin^2 60°$$

$$\Re \approx 0,54 * 10^{-2} + 4,67 * 10^{-2} \approx 5,21\%$$

The reflectance loss from the boundary of glass and Bacteriorhodopsin layer inside the film will be small, due to their similar refractive indexes, which both are around 1,5. A reduction factor for the measured read-out beam will therefore be roughly 5,2%.

3.2.3.3   Diffraction results
The measured intensities were plotted and an estimate for the maximum diffraction efficiency could be calculated. These values are lower than values listed by MIB.
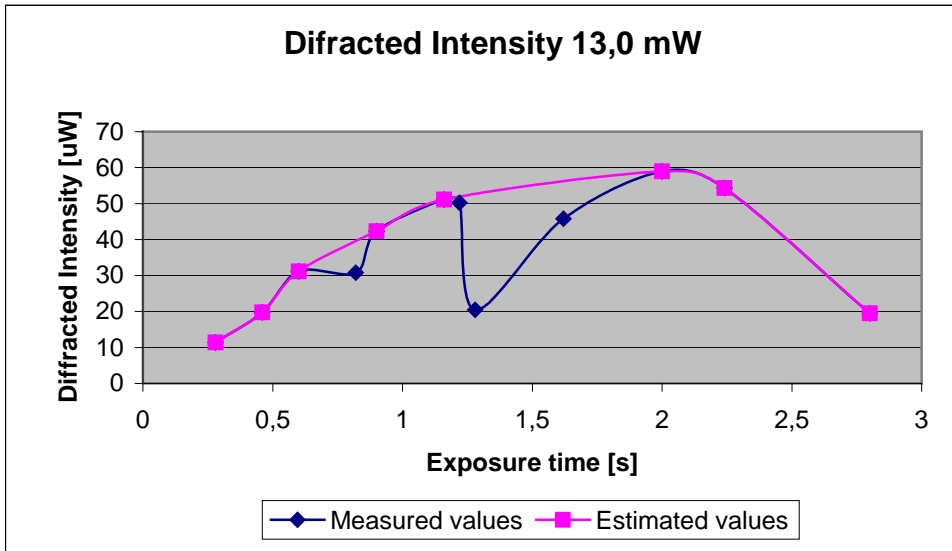
3.2.3.3.1

Figure 41 Diffraction efficiency at 632,8 nm for different exposure times.

Total light flux = $(I_{obj} + I_{ref})/A \approx (6,8 + 6,2)/1,33$ [mW/cm^2] $\approx 9,8$ [mW/cm^2].
Read out intensity I(i) = 6,2 [mW]
Reduced by reflection from front glass film I(i) $\approx 5,9$ [mW]
Measured maximum diffraction efficiency η_{max}:

$$\eta_{max} = \frac{I_{diff}}{I_{read-out}} \approx \frac{51,1e^{-6}}{5,9e^{-3}} \times 100\% = 0,9\%$$

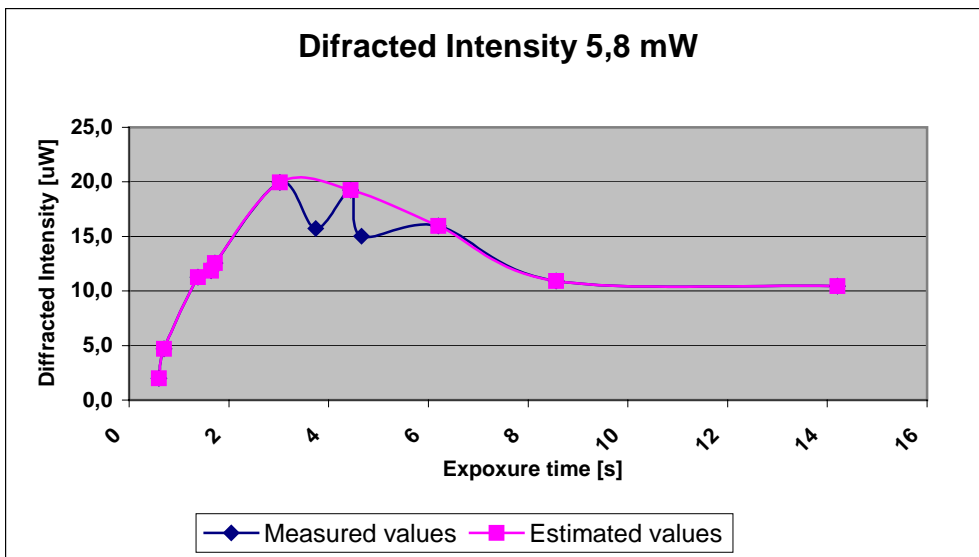### 3.2.3.3.2 Diffraction efficiency measurements using 5,8 mW total power

Figure 42 Diffraction efficiency at 632,8 nm for different exposure times.

Total light flux = $(I_{obj} + I_{ref})/A \approx (3,0 + 2,8)/1,33$ [mW/cm^2] $\approx 4,4$ [mW/cm^2].

Read out intensity I(i) = 2,8 [mW]

Reduced by reflection from front glass film I(i) ≈ 2,7 [mW]

Measured maximum diffraction efficiency η_{max}:

$$\eta_{max} = \frac{I_{diff}}{I_{read-out}} \approx \frac{20,0e^{-6}}{2,7e^{-3}} \times 100\% = 0,8\%$$

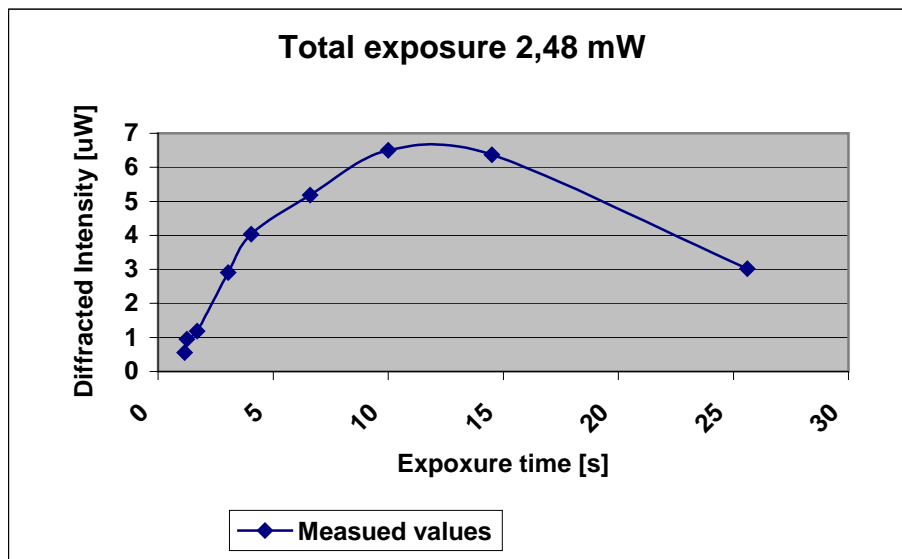### 3.2.3.3.3 Diffraction efficiency measurements using 2,48 mW total power

Figure 43 Diffraction efficiency at 632,8 nm for different exposure times.

Total light flux = $(I_{obj} + I_{ref})/A \approx (1,3 + 1,2)/1,33$ [mW/cm^2] $\approx 2,5$ [mW/cm^2].

Read out intensity I(i) = 1,2 [mW]

Reduced by reflection from front glass film I(i) ≈ 1,1 [mW]

Measured maximum diffraction efficiency η_{max}:

$$\eta_{max} = \frac{I_{diff}}{I_{read-out}} \approx \frac{6,5e^{-6}}{1,1e^{-3}} \times 100\% = 0,6\%$$

Discussion

Note that the diffraction efficiencies are estimates, and not absolute numbers. Results performed by other research groups [Downie and Smithey 1996] indicate a more smooth response function than our measured values. Therefore a suggestion were the most unlikely measurements have been removed, has also has been plotted. It is questionable that all these removed measured values are lower than the suggested curve. This could indicate that the emulsion has been partially saturated from earlier measurements. It has been double-checked, that before each measurement series the film has experienced a minimum of 30 seconds erase light. The problem was particularly noticeable for the stronger intensities. The "low" intensity (2,5 mW/cm^2) measurements turned out well. In comparison, Downie and Smithey [1996] have reported much higher diffraction efficiency, approximating 8% for specially hydrated D96N (OD 4.0) films, developed by their own bio-chemical laboratory. This is very

impressive. Hampp [2000] actually list that the maximum diffraction efficiency of Bacteriorhodopsin films to be 7%, but researchers have different opinions as well as results. Our film has a factory listed diffraction efficiency of 1-3%. Which is in agreement with our measurements, as the results indicate a higher diffraction efficiency using stronger recording intensities.

We also tried to measure diffraction efficiency using the yellow He-Ne laser at 594nm, but it was extremely difficult to measure the low diffraction intensities. The measured transmitted object beam was so weak that our equipment was unable to record it. This was very unfortunate. The BR film has a much higher O.D at the yellow wavelength as well as the yellow laser has less intensity than the red laser. A set-up using a red wavelength as a read-out beam was attempted. An important change had to be made, as the BR film is considered a thick holographic grating. The read-out beam had to illuminate the emulsion from a slightly larger angle than the yellow reference wave to fulfil the Bragg condition. Thick holograms are extremely sensitive to having a correct illumination angle when reconstructing a hologram at a different wavelength than it has been recorded. The problem was that the red read-out beam was expanded through the same lens as the yellow recording wavelength due to shortage of table space in front of the film. The angle proved too small for a qualified read-out as nothing could be measured by the wattmeter. This elucidated that the Bragg condition is crucial for a thick hologram like our BR film, please confer to section 2.1 to see how a thick grating was defined. The Bragg condition will be discussed in further detail a bit later, when recording holograms with the BR film was tested in section 4.2.

4 Bacteriorhodopsin holograms

4.1 Setup conditions

The main application of the BR film is to record images of small particles. To test the holographic properties of the Bacteriorhodopsin emulsion a lot of holograms of various objects were made. The exposure characteristics found for the diffraction experiments were good references for how much intensity and what exposure times to start with on the different set-ups. These parameters were then step-wise changed to yield optimal time and object to reference ratio, which resulted in the holograms with the greatest contrast and brightness. After making a hologram it would always be a trade-off between the intensity of the read-out beam versus the hologram relaxation time. A strong read-out beam produced a brighter virtual object, but the image was faster erased, hence resulting in a shorter time to record pictures of the virtual object. It was always difficult to properly photograph the holograms. The technique used to record the digitally recorded photographs will be explained first.

Prior to recording:
- The BR film holder was adjusted appropriately between the object and reference beam, resulting in a proper angle between beams
- The object beam was oriented at the chosen area on the object and the reference wave was illuminating where the film would be placed. Their intensities were adjusted to be between 10:1 and 2:1 (reference to object). This ratio was measured in [lux] (intensity per unit area) with an optical sensor inside the holder. The real illuminance experienced by the film could then be compared
- The digital camera was manually focused at the object surface through the BR film holder and ISO light sensitivity adjusted (explained in common camera instruction manual). ISO levels of 400, 800 and 1600 were used the most. The camera would be kept at a fixed position on the table.

To photograph the virtual image after a recording, the following procedure was used:
- The object illumination wave was blocked

or
- The recording laser was blocked and another read-out beam was illuminating the film from the appropriate Bragg angle

- The object was either removed or covered behind black paper
- Any reduction filter in the reference beam could be removed for maximum brightness in the virtual image (optional)
- Photographs of the virtual object were taken. The camera was adjusted at small angles to obtain better perspectives of the object. The ISO number could be changed if the object was too bright/dark

We set ourselves a schedule to make single exposure holograms, double exposure and then to try recording real-time holograms. The easiest part would be the single exposure hologram. We already knew this worked, as the film reconstructed the object wave as seen in the diffraction experiments. It would be more difficult to adjust the recording times between two successive holograms to make proper double

exposure. The first recorded hologram would fade away in time, as well as being erased by the second recording. The real-time recording would also require a weaker object intensity beam, since the illuminated object needed to be of equal brightness as the reconstructed virtual object. Single exposures were made first.

4.2 Holograms of a metal object

A flat, metal lens holder was chosen as the object, due to its good reflectance. The holder was spray painted white to increase the amount of diffuse reflected light. Most of the illuminating object beam would then reflect diffusively back to the film. The goal was to make double exposure holograms of the holder, and cover the flat surface with viewable black fringes (small movements). The first holograms was taken with a red He-Ne laser, but the brightness in the virtual images were very weak. The irradiance that reached the film was much less using the reflection from the surface of this object than the irradiance transmitted through a transparent object. The powerful but mode-hopping Nd-Yag laser was tested, although we would expect interference stripes resulting from it. Hopefully the holograms would be bright enough that two different sets of fringes with different curvatures could be separated. A red He-Ne laser would be used to read-out the recorded hologram. The film is less sensitive to this wavelength and the virtual image would then last longer. All the other equipment was the same as for the diffraction experiments, and the recording characteristics were

Laser:	Nd-Yag at 532nm
	Total power = 54,9mW
Object beam:	Illuminating the object, a circle of diameter = 2,1 cm (A ≈ 3,5cm^2)
	I_o = 31,7mW
	Measured irradiance in holder ≈ 417lux
Reference beam:	I_R = 1,93mW
(reduced)	Illuminating the film holder of diameter = 1,8cm (A ≈ 2,5cm^2)
	I_R/A = 0,76mW/cm^2
	Measured irradiance in holder ≈ 900lux
Ref. / Obj. beam:	2:1
Read-out laser	He-Ne 632,8nm (same as used in diffraction experiments)
	$I_{Read-out}$ = 0,28mW
Illuminating the film holder of diameter = 1,8cm (A ≈ 2,5cm^2)	
	I_R/A = 110μW/cm^2

The set-up is shown Figure 44. All trajectories are not shown, but will be briefly explained. The beam splitter (BS) split the incoming beam to one object and one reference wave. These were both reflected from a few mirrors to get a good angle at the small film plate and to hit the object at a good angle (if it came from behind the film plate, then more reflected light return in the film direction). Both beams were expanded through microscope objectives (MS) to increase the beam and remove noise. The red laser joined the green laser light at the dichroic mirror. This mirror reflects light at the green wavelength and transmits at all other (ideally). In this way the red light would follow the same path as the green recording source and illuminate the BR film from the same reference angle. This was not totally appropriate, as the Bragg condition for a grating implicates another angle for a different wavelength. Therefore the BR film would have to be turned, in order to see the hologram with the red light source. The Bragg condition for a transmission grating implies that the recorded fringes in the emulsion structure decide how large the read-out angle should

be for different wavelengths. To view a hologram at the same wavelength as the recorded light source, the angle has to be the same as the reference beam angle. This is never a problem. For all other wavelengths than the recording, the angle can be calculated using the distance between interference layers in the emulsion. These layers will have a distance d, given by the object and reference wave's angle to the normal of the emulsion:

$$d = \frac{\lambda}{\sin \theta_R + \sin \theta_O} \tag{4-1}$$

The angles and the distance between layers, for the current recordings were:

$$d = \frac{\lambda}{\sin 45° + \sin 22°} \approx \frac{532 * 10^{-9} m}{1,08} \approx 0,49 \mu m$$

For a read-out beam of 633 nm this results in an angle of:

$$\theta_{\text{Re} ad-out} = \sin^{-1}\left(\frac{\lambda}{2d}\right) \approx \sin^{-1}\left(\frac{633 * 10^{-9}}{2 * 0,49 * 10^{-6}}\right) \approx 40°$$

The read-out angle should therefore be 5° smaller than the recording reference wave. This angle is not an absolute value, and parts of the hologram can be viewed at other angles but they should not differ by more than a few degrees.

The red laser is plane-polarized, and the polarization direction was aligned to match the green recording laser for maximum diffraction from the hologram. The pinhole was removed for the reference beam microscope objective, due to aligning difficulties, which introduced some speckle. The pinhole was used for the object beam, and this actually removed the object illumination at the red wavelength, as this was not perfectly aligned. Note that the red read-out laser was only tested visually to satisfy the Bragg condition. The virtual object could be seen using it, but it proved to be easier to photograph the virtual image with the green laser. No photographs were taken using the red laser as a read-out. The green laser would record the holograms and the red served as a visual read-out.
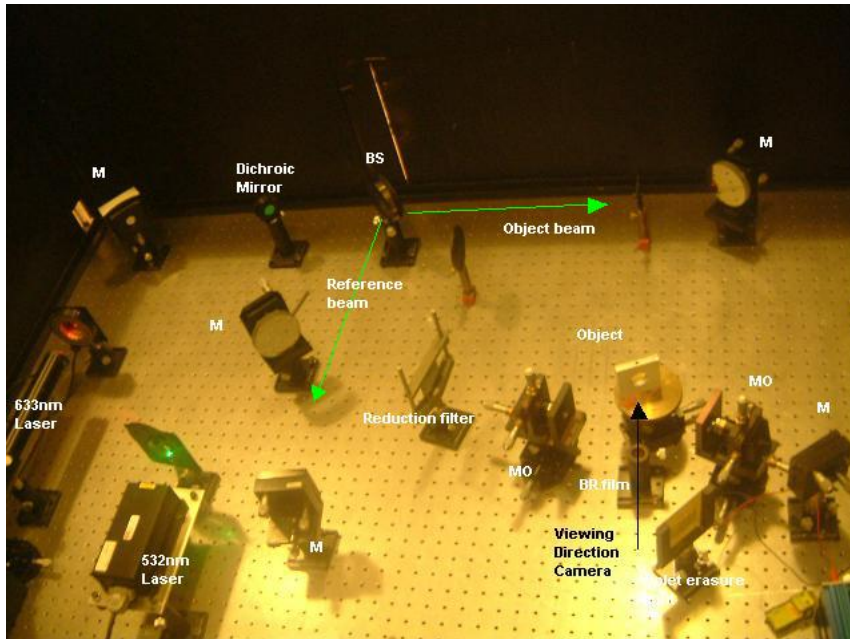
Figure 44 Set-up using a red read-out laser and a green write laser.

Discussion

15 seconds of exposure resulted in virtual objects with interference fringes in front of the virtual objects as shown in Figure 45. The metal object is also shown under white light conditions in Figure 53. The hologram has big dark lines in front of the object making it hard to see the contours. Only the most illuminated part of the object produced an image that could be properly photographed. Note that the centre hole in the metal can be recognized. Our eyes are extremely sensitive, and most of the virtual object could visually be identified in the live hologram. This hologram is a double (perhaps multi, depending on how many modes the laser have) exposure hologram. This hologram has been subject to one recording but with two wavelengths at the same time instead of one after another. At least, the hologram contained interference fringes.
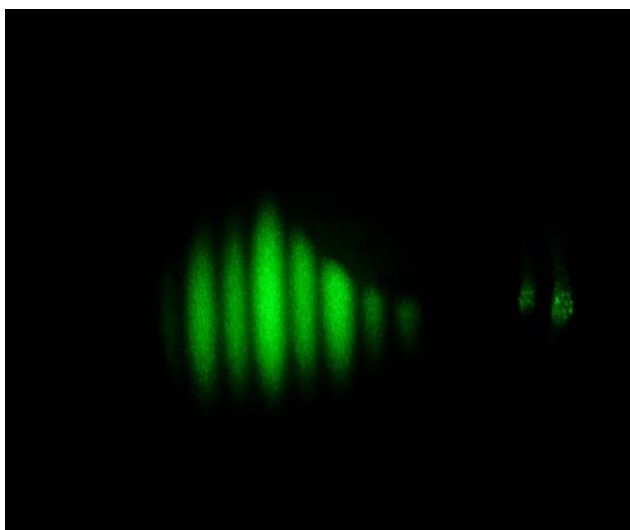

Figure 45 Hologram of a flat metal holder.

4.3   Holograms of a transparent object

The first hologram was made of a glass container with the index matching fluid and particles. Due to an inner diameter of ~3,0 cm the container was divided inside by a glass wall. This reduced the volume to about the half, diameter ~1,6 cm, which would be more similar to the inner tank diameter, which is either 2 cm or 1 cm. The set-up is shown in Figure 46 and two holograms are shown in Figure 47.
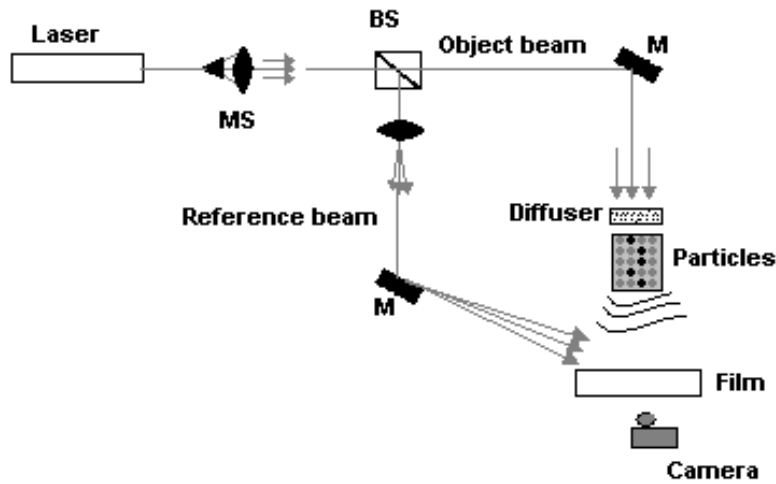

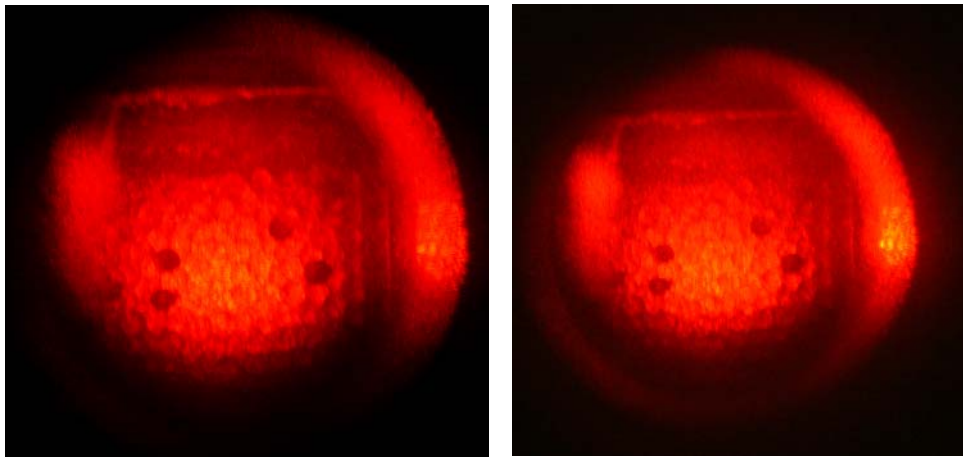**Figure 46 Set-up using the red laser, and object beam through the particles.**

Figure 47 Two single exposure holograms using the BR film and with 25 seconds exposure.
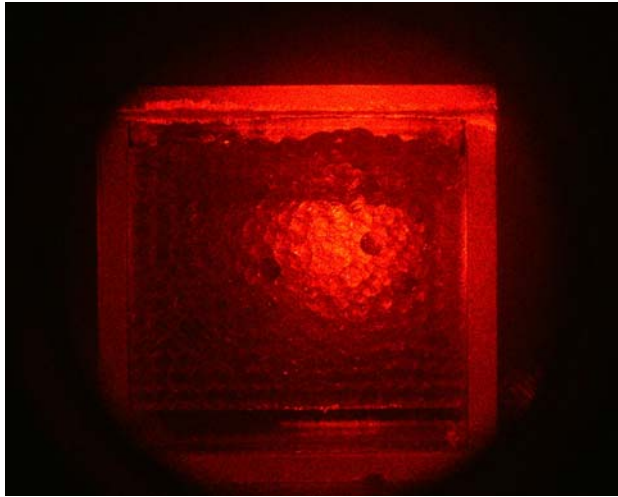
Figure 48 The object illuminated by the object beam without the BR film present.

<u>**Discussion**</u>
The black particles can be identified, but the other particles can also be seen. The image seemed very diffuse and the depth was not particularly good.

The glass container photographed using the object beam only, is shown in Figure 48, but from a slightly different angle. It can be seen that all particles refract light in numerous directions. The transparency of the particles in the index-matched fluid at 633 nm can therefore be questioned.

## 4.4 Recording two successive holograms

Double recordings were first tested using the glass container. The container was moved several hundred micrometers (and less) between takings, but the hologram did not produce any interference fringes across the glass surface, or these were too weak to be seen. The recording geometry used the glass container as a transparent object (object wave transmitting). The entire container would therefore move instead of just the particles inside. We suspected that the three glass walls contributed too much to the recording for resolvable interference fringes to be observed. To find out how to make two successive recordings in the BR film the same set-up using a less complex object was tried. The goal was to record two images. The movement between exposures needed to be large enough to show two separately recorded holograms (cm-range). A thin metal ring was positioned after two diffusers, and in front of the film. The thin ring would then be a nice tracer, and two different exposures could be compared (in order to find appropriate exposure times). The recording parameters were

Laser:	He-Ne 632,8nm (same as used in diffraction experiments)
Object beam:	Collimated light illuminating the diffusers
	Measured irradiance in holder $\approx$ 62lux
Reference beam:	I_R = 2,45mW
(reduced)	Illuminating the film holder of diameter = 1,9cm (A $\approx$ 2,8cm^2)
	I_R/A = 0,86mW/cm^2
	Measured irradiance in holder $\approx$ 500lux
Ref. / Obj. beam:	8:1

The most appropriate exposure times for two successive recorded holograms, proved to be about *20 seconds* for the first exposure, and *14 seconds* for the second. Between the two recordings the ring was moved approximately 1cm parallelly to the film. The object seen in white light conditions and with red recording light seen through the BR holder (no film) is shown in Figure 49. The two successive recordings produced a hologram that is shown in Figure 50.
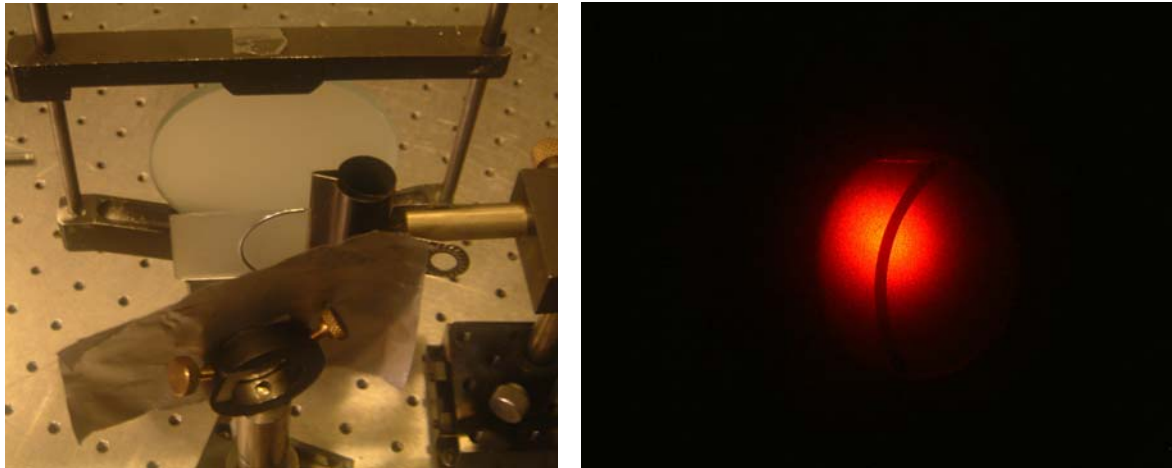
Figure 49 Left image show the two diffusers, the object and the BR film holder. An image of the object (no BR film) is shown to the right.
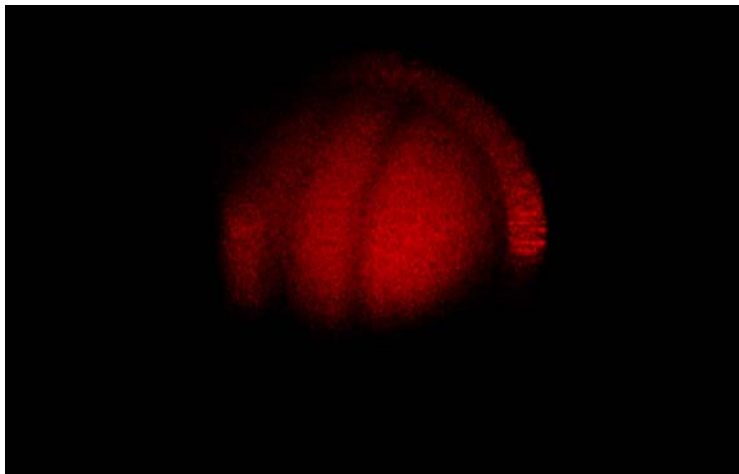
Figure 50 Double exposure hologram of a thin metal string using the BR film.

Discussion

The holograms show two metal rings at almost the same brightness. Tests of two equally long exposures (2*20 seconds) resulted in the last recorded metal ring being brighter than the first. A shorter second exposure than ~10 seconds produced a bright first image and a weak second image.

This was a nice example showing that it was possible to store a second hologram with the BR film without erasing the first image. Our next goal was to record double exposure holograms showing interference fringes.

4.5 Double exposure holograms

Using the strongest of our red He-Ne lasers (listed as a 30 mW, but lase at ~20 mW), the double exposure holograms required about 45 seconds for the first exposure and about 30 seconds for the second using the listed laser power below. A thin beam splitter was used, resulting in a strong object beam and a weak reference beam. This ratio was chosen to maintain the object illumination as strong as possible. If the object beam was reduced to keep the reference to object intensity ratio larger than 2:1, then the hologram's brightness always weakened. Hence the listed ratio was used as it was. The set-up was exactly the same as for the real-time holograms, in the following chapter. A figure of a double exposed hologram where the object has been moved 30 µm parallel to the film between exposures is shown in Figure 51.

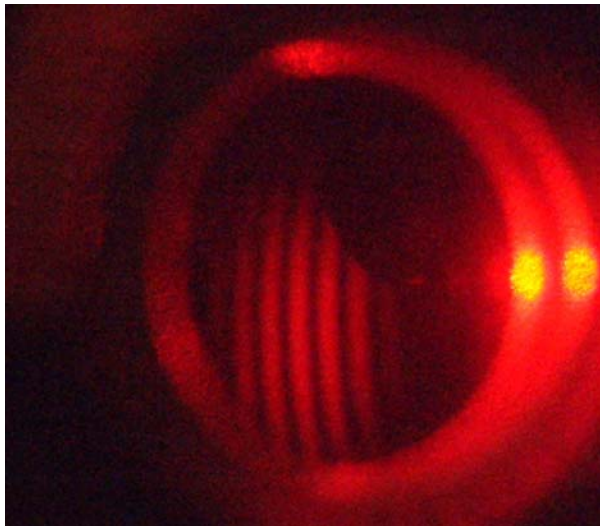|	
Laser:	He-Ne 632,8nm (same as used in diffraction experiments)
	Total power = 21,2mW
Object beam:	Illuminating the object, a circle of diameter = 2,9 cm (A ≈ 6,6cm^2)
	Measured irradiance in holder ≈ 43lux
Reference beam:	$I_R = 0,244$mW
	Illuminating the film holder of diameter = 3,5cm (A ≈9,6cm^2)
	$I_R/A = 25\mu W/cm^2$
	Measured irradiance in holder ≈ 35lux
Ref. / Obj. beam:	0,8:1

Figure 51 Double exposure hologram (45sec then 30sec) of an object that has moved 30um.

Discussion

The holograms were of good quality. Using different object movement between the two exposures, different separation distances were observed. The BR film worked well, and proved to be a much faster way to produce double exposure holograms than with silver halide films. The only problem encountered was the need for a strong laser. The metal holder holographed in this test was positioned very close to the film in order to maintain the object beam as strong as possible. Despite of this extremity, only a fraction of the object is observable, as seen in Figure 51. A stronger laser should have been applied to holograph the whole object.

4.6 Real-time holograms

The equipment for moving the object had a minimum read-out scale of 10 μm/line. Due to this limitation, the test translations were chosen to be directly out-of plane, as this would be the least sensitive direction (confer to section 2.4). Parallel movement proved too sensitive for translation above 50 μm. Surpassing this value the number of interference fringes and their separation distance were not possible to distinguish. That would limit the number of possible movements to 4-5. The out-of plane movement on the other hand proved to have a maximum translation distance of ~130 μm before the interference lines disappeared, for the approximately same set-up. The set-up is shown in Figure 52.
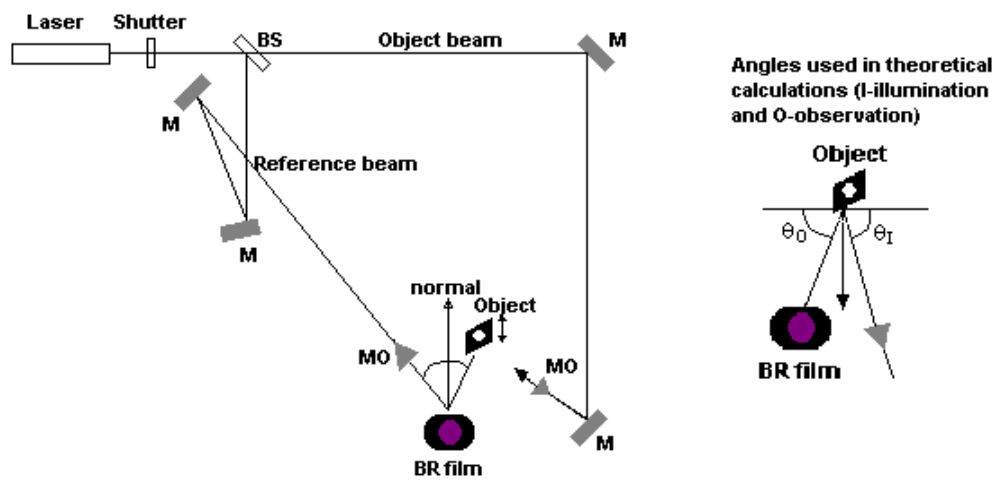
Figure 52 Set-up using the BR film in real-time holography.

The camera angle showing the object seen in white light (with no film) and the illuminated object is shown in Figure 53.

Figure 53 Object seen through BR film holder without film, in white light conditions, and with laser object illumination.

A single exposure of 45 seconds was recorded. The object beam was reduced to 0,13% and then continued to illuminate the object. By adjusting the micrometer screw

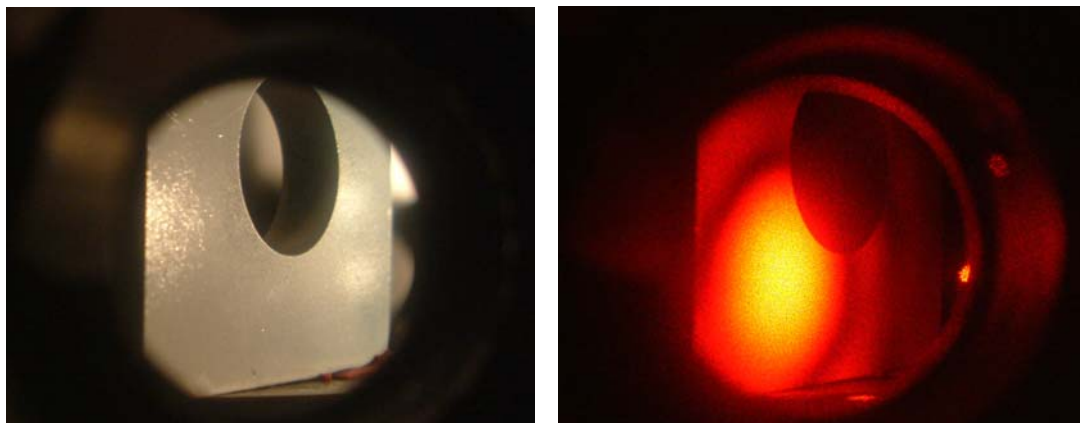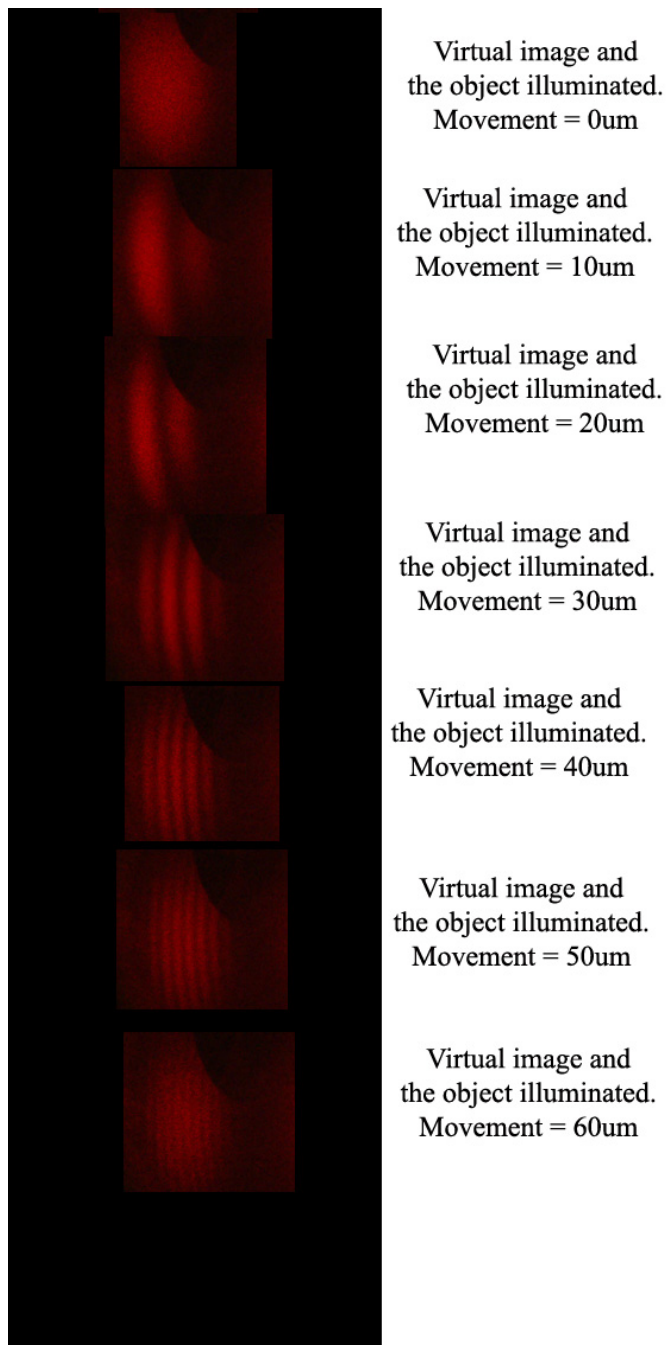interference patterns could instantly be seen. The interference fringes were photographed for translation between 0 to 60 μm. These pictures were cropped and joined in Adobe Photoshop, for presentational purposes, as seen in Figure 54.

Figure 54 Real-time holograms were different object translation show a different fringe separation distance.

Discussion

The fringe separation distance, decreases with larger translation as expected. This was in accordance with the interference experiments made earlier. The photographed fringes do not fully appear to be parts of concentric circles. This has two main reasons. If the "epicentre" of the fringes had been displaced a few centimetres, then the fringes might well appear almost straight for such a small area. Another cause is

the interferometric system sensitivity to parallel displacement. The system is almost ten times as sensitive to this displacement as to out-of plane changes as demonstrated in section 2.4.2.1. This could also explain the straightness of the fringes. The most interesting results in these holograms are the real-time features. By carefully adjusting the micrometer screw we could continuously observe the change in separation and size of the fringes.

To test the previous theory for double exposure holograms, the angles in Figure 52 were used. The geometrical parameters were

|	
Observation distance (camera)	23cm
Observation angle	$\theta_o \sim 68°$
Illumination distance (to object beam pinhole)	6,0cm
Illumination angle	$\theta_I \sim 55°$

4.6.1.1 Testing double exposure theory with real-time experiments

To see how the translation related to fringe separation, the theory established in section 2.4.3 was applied. The theoretical results did not match the measured values for out-of plane displacements made with Silver halide holograms, and was not expected to do here either. The in-plane measurement would probably match the chosen theory better, but this translation was inappropriate as mentioned earlier. A comparison of the theoretical and the measured values is listed in Table 9. The distance between interference fringes was measured on the basis on the fringe distance in the images captured and compared to the real-life diameter of the exposure area.

Out-of plane movement				
	Theory		Measured	
Displacement	D (fringe separation)	1/D (lines/mm)	D (fringe separation)	1/D (lines/mm)
20μm	5,01	0,20	8,00	0,13
30μm	3,34	0,30	4,90	0,20
40μm	2,50	0,40	3,50	0,29
50μm	2,00	0,50	2,50	0,40
60μm	1,67	0,60	2,00	0,50
70μm	1,43	0,70	1,50	0,67

Table 9 Comparison of experimental and theoretical out of plane translations.
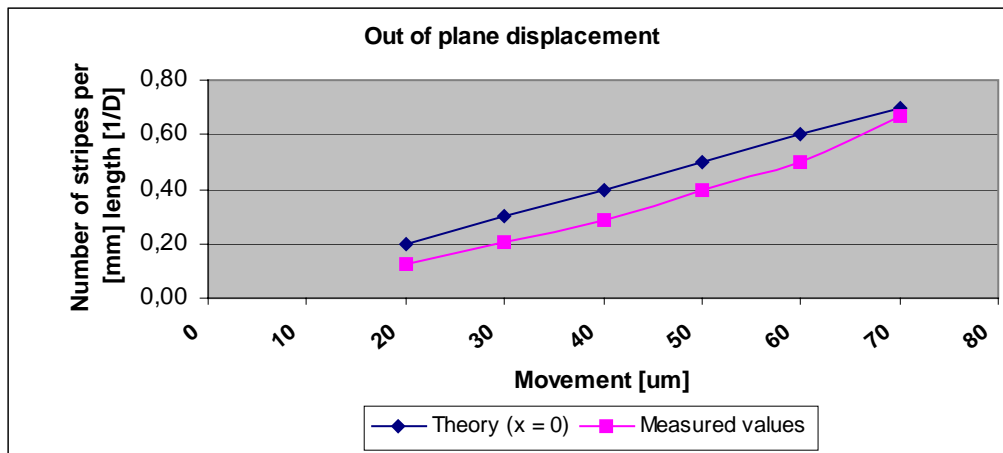
Figure 55 Comparison of measured and theoretical values for out of plane translation, using real-time holograms.

<u>Discussion</u>
As Figure 55 shows, there is correlation between measured and theoretical values. The same second order behaviour as seen in the experiments using silver halide films, appears to be present as the numbers of lines/mm continue to increase with larger displacements. The plotted theoretical values show a linear relation between translation and the number of fringes/mm. As in the case with silver halide experiments the reason for the mismatch between theoretical values and measurements is believed to be dependant on how the measurements are taken. In this case we have obviously measured at better locations at the object plane, thus keeping to approximately same fringe order through the measurements. The experimental results almost match the predictions made by our linear theory.

The separation distance is dependent on the observation distance *O*. This explains why the used translations for the real-time experiments are shorter (max 130 μm) than for the same movements in the double exposure experiments performed earlier (several 100 μm). The angles also change the possible resolvable translation range. The centre of fringes in these real-time holograms, were calculated to be displaced approximately ~ 2,6 cm from the centre of the images (same calculations as earlier), and explains why these centres could not be seen. The fringes across the virtual images in Figure 54 show slightly curved fringes as expected for perpendicular translation to the film.

4.7 Real-time experiments on transparent objects
The holography experiments have involved few transparent objects resembling a diffuse medium. As the refractive index of the fluid would be close to that of the glass particles, our final object would be a semi-transparent, but scattering medium. The transmitted light would be scattered according to Mie's scattering theory, which applies for particles larger than one tenth of a wavelength, and light may be out of phase from different trajectories through the medium. The transmitting object wave will therefore be partly incoherent, which reduces the interferogram's (two interfering holograms') contrast. There will be additional interference noise in the reconstructed holograms due to the out-of-phase light of the object beam. This project will focus on experimental work with holography, and therefore not go into detail of the scattering

processes. It can be mentioned that Mie's theory predicts light scattering strongly peaked in the forward direction. More information on this theory can be found in Born and Wolf [1999]. Different objects were made to simulate the expected effects. A few diffusers and three samples of acrylic Plexiglas were acquired. The diffusers were chosen due to their similar behavior to a turbid media, while Plexiglas is transparent for visible light and is easy to work with. One of the key interests was how much structure or degree of transparency there needed to be on the surface of an object in order to visualize interference patterns on a strong background illumination, and how well a diffuser worked in interferograms. Holographers tend to use a diffuser in front of or behind their objects when making holograms of transparent objects [Haussman and Lauterborn, 1980]. As diffusers (depending on type) make the transmitted light less coherent, and also partly depolarizes it, its influence on our real-time experiments would be interesting. The objects ranged from an almost transparent object (Plexiglas with large circles, no.1), to a more disruptive element of 2 diffusers put closely together. The specifications for the diffusers used in the following experiments are most likely the ground glass type from Edmund Optics, as the dimensions match to their product, 'NT45-651'. These filters "offer an even diffusion across the surface. The scattering is a compromise of low scatter loss and medium diffusion" [http://www.edmundoptics.com, 07.06.04].

4.7.1 Set-up

Both reference and object illumination was collimated. Path lengths of the two waves were adjusted to be equal within ±1cm. The object wave hit perpendicular to the film plane, while the reference wave had an inclination of ~ 68° to the plane. All objects were moved parallel to the film plane (resulting in vertical fringes), with a resolution of 10 μm. The distance from film to the object was 15,0 cm, while the extra diffuser was 7,5 cm further away. All hologram recordings were performed with approximately 2:1, reference to object beam intensity, measured in the film holder position. We photographed the interferograms through a polarization filter, whenever this improved the fringe contrast. A digital camera has been applied to record the following experiments. Manual focus has been the only way to visualize the interference pattern in front of the object surface, as auto-focus will focus at the BR film instead. Various ISO sensitivities (ranging from ISO 160 at 6M pixels to ISO 1600 at 1M pixels) have been selected to best match each hologram's intensity. No images have been edited in photo editors.

4.7.2 Transparent objects

The different objects under testing was:

1. Object is a ground glass diffuser. The thickness is 1,6 mm. The glass is most likely of the "Soda Lime" type, with one diffuse surface, which arises from two orthogonal sandblast passes of a 220-grit type to ensure even diffusion [http://www.Edmundoptics.com, 06.07.04].
2. Objects are two diffusers (2*1,6 mm, same type as no.1). Two diffusers are fitted closely together to increase the thickness of the overall diffusing element.
3. Plexiglas (3,0 mm thick), no.1. Large circular carvings (d ~ 8,5 mm) of slightly different sizes and random positions, on one side of the material. This

served as the object with the least surface structure, and hence the least diffraction.

4. Plexiglas (3,0 mm thick), no.2. Small circular carvings (d = 3,0 mm) at random locations, on one side of the material.
5. Plexiglas (3,0 mm thick), no.3. White dull surface at one side of the glass. Polished with sandpaper (fine, P 600 grade) in all directions. The surface of this object resembles that of a weak diffuser, but instead of a point grid (sandblasted diffusers) this grid will be of engraved stripes.

A collection of results is show in Table 10 below.

| No.	Object	Extra Diffuser	Visible fringes	Fringe contrast	Max. Observable movement [μm] **
1	*Diffuser*	Yes	None*	-	-
		No	Yes	Very good	*200(+)*
2	*2*Diffuser*	Yes	None	-	-
		No	Yes	Good	*150-200*
3	*Plexiglas no.1 (large circles)*	Yes	None*	-	-
		No	None	Too strong background ill.	-
4	*Plexiglas no.2 (3mm circles)*	Yes	None*	-	-
		No	Yes	Poor (strong background ill.)	-
5	*Plexiglas no.3 (dull surface)*	Yes	Yes	Not good	*40*
		No	Yes	Good	*200*

Table 10 Comparison of fringe results using different diffusing objects.

* Reducing the distance between object and diffuser to less than 1cm, it became possible to observe weak fringes.
****** Observation distance is 21 cm.

Comments
The term "maximum observable movement" is used to describe the situation when the fringes either are too close to be distinguished or the contrast of the fringes is too low. All objects have been holographed in good quality, as shown in Figure 56 below. Note that these holograms are recorded with the extra diffuser in front, as this improves the field of view (a larger area is illuminated) and removes the strong direct beam intensity providing more homogenous illumination. The overall focus in these tests is solely on the quality of the interference pattern of one recorded hologram interfering with the live object wave, so these holograms will not be further discussed.
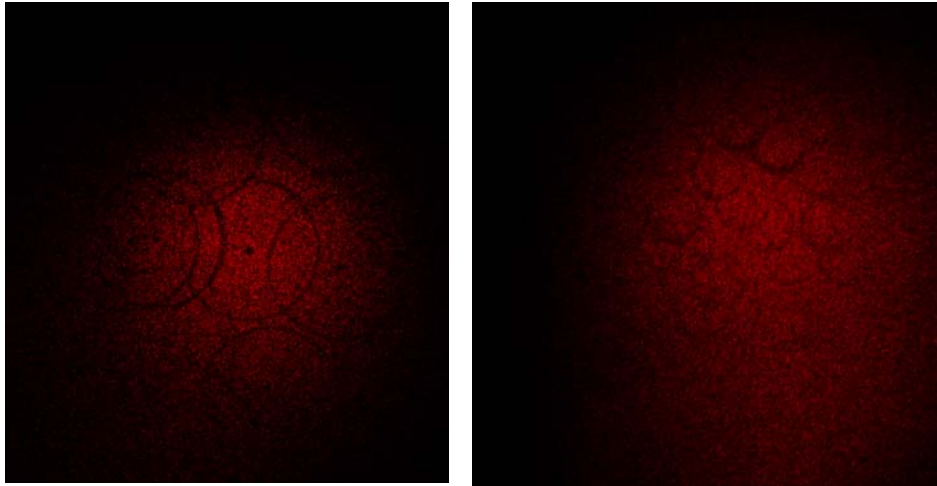
Figure 56 The left image shows a hologram of object no.3 (large circles), while image to the right shows object no.4 (3mm circles).

Discussion

The tests reveal that a moving object does not work well with an additional diffuser in fixed position in front of it. In this case no interferogram could be observed when a diffuser was the moving object. The "roughly" polished Plexiglas was the only object that resulted in resolvable fringes with a diffuser in front, but the fringes were hard to focus on and could only be tracked for a short distance before they became too weak. The diffuser in front of the object was damaging the quality of the interferogram. This is a consequence of the reduced amount of coherent light reaching the object, due to the omnidirectional scattering from the sandblasted surface structure of the ground glass diffuser. The weaker the fringe pattern, the harder it becomes to separate the fringes, as they get closer together (longer displacement). The ground glass diffracts the incident light as a random grid (point grid) and partially changes the phase of the coherent light. It also depolarizes the incident light, which also reduces interference, as there will be less polarized light to make the hologram. Observations indicated that larger distances than ~1 cm between the object and the fixed diffuser completely removed the possibility of observing interference fringes. This would imply that the ground glass has been sandblasted to a non-plane surface, as remaining flat surfaces would let un-diffracted parts of the incident plane wave (still coherent) through its surface. To check what the surface diffuser structure looked like, a few images were recorded. Images of the diffuser and object no.5 are shown in Figure 57 and Figure 58. These show a much less uniform surface than expected.
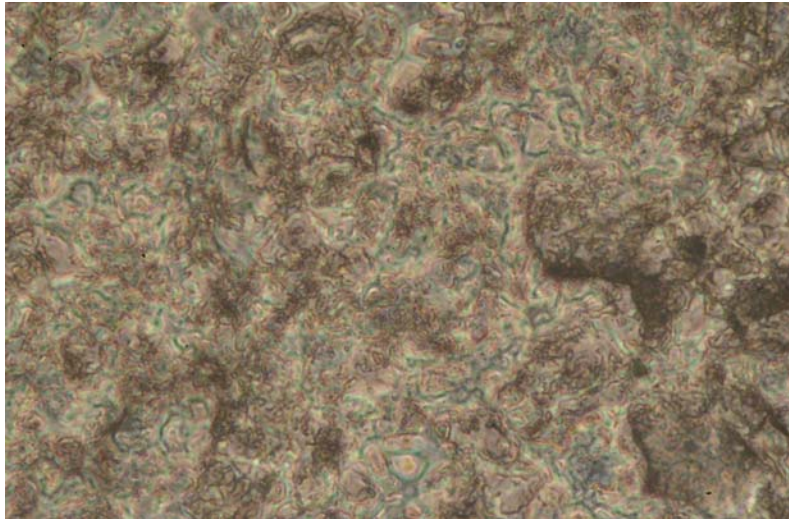
Figure 57 Ground glass diffuser surface, magnified at x400.
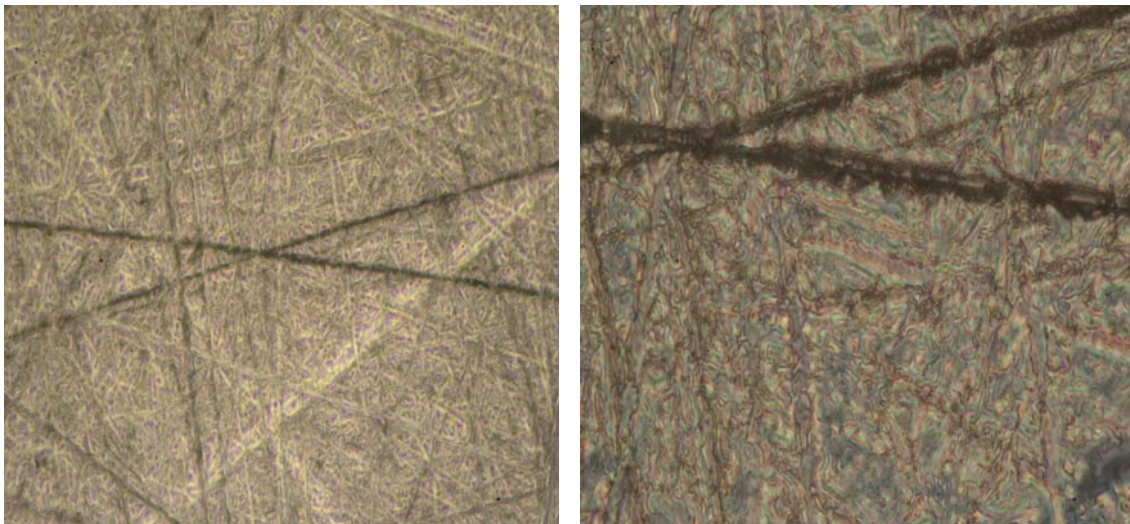
Figure 58 Both images show the surface of the polished object no.5. To the left it is magnified x100 and the right image show a magnification of 400 times.

Note that these images do not show the depth of the surface structure. It is believed that the diffuser surface has greater variations in depth than the Plexiglas, as it diffracts much more light.

The partly coherent transmitted light through a diffuser will be aspherical, implying that the coherent light reaching the object is dependent on the distance between the diffuser and the object. Two closely positioned diffusers working as the object can be tracked as it moves (minimum separation distance), but a single diffuser will result in better contrast. This can be seen in the obtained images shown in Figure 59.
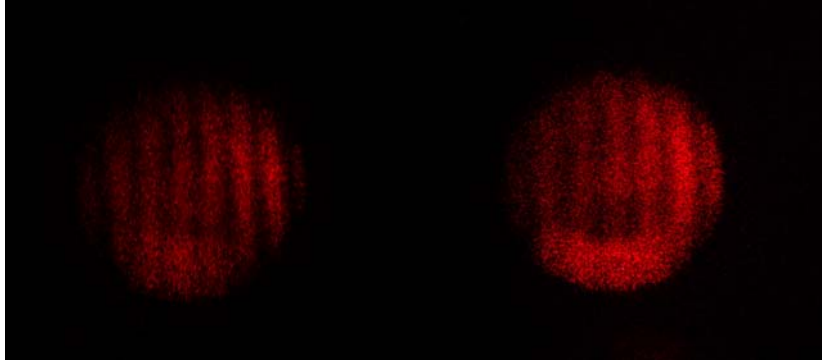
Figure 59 Left image show one diffuser, object no.1, with 50um translation. Right image show two diffusers (closely aligned, both moving), object no.2, with 50um translation.

4.7.2.1   Plexiglas objects

Using the two thin Plexiglas objects with circular engravement it was a problem of not having enough diffraction to actually observe an interference pattern. It seemed like the surface structure of these objects interacted too weakly with the object beam. The strong background illumination therefore made the surface of the object and also the fringes in front of its surface too weak to be seen. With a diffuser in front, it was the diffuser we observed instead of the object, and without a diffuser we had a hard time focusing at the weak fringes in front of the strong illumination from the pinhole (Gaussian profile with strong center intensity). The image obtained with the 3mm circles (it has the most structure of the two), without a diffuser is shown in Figure 60, while the object with larger circles could not be photographed with or without a diffuser. Of the Plexiglas objects it was the polished one that worked the best (no.5). This had observable fringes both with and without a diffuser in front as seen in Figure 61.
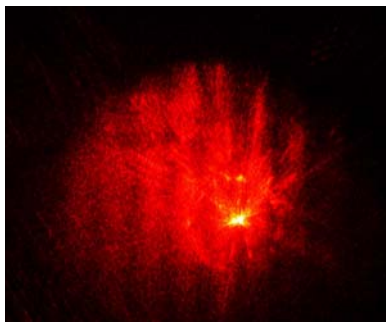
Figure 60 Object no.4 (small circles) without diffuser in front, moved 30um parallel to the film.
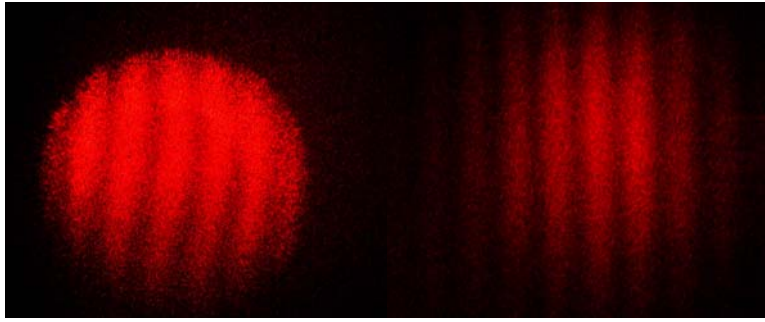
Figure 61 Left image shows the Plexiglas with dull polished surface, object no.5, without a diffuser in front, 30um translation. Right image is with a diffuser in front, 10um translation.

Using only object no.1 (a diffuser), a simple synopsis was made to show how the interference pattern looks for a transparent object, moving in the four horizontal directions. This overview is shown in Figure 62.

Figure 62 Overview of different horizontal translations. Left and right images are translation parallel to the film, while the other two are perpendicular movement. No diffuser has been applied in front of these recorded interferograms.

Discussion

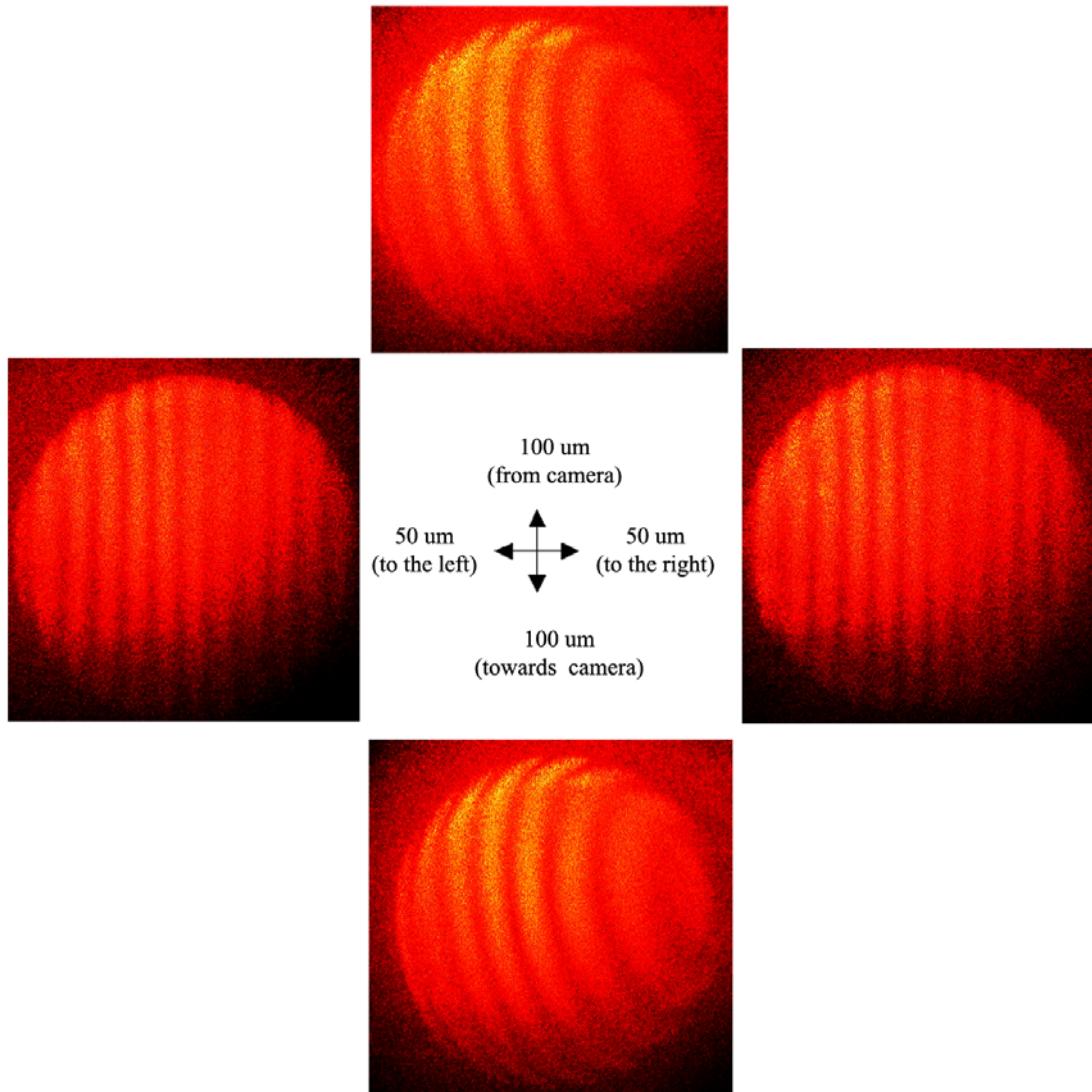These tests indicate that the amount of diffraction from the particles suspended in the index-matched fluid will determine whether a diffuser should be used or not. The preferred option will be not to use a diffuser in front of the tank. This is obvious, due to the less coherent object beam and increased noise in the holograms. If the index matching is too accurate, it may be problematic to observe the fringe pattern without a diffuser, as the background illumination might be too strong. Inside the tank the particles will lay beside each other, creating several "layers" in the depth, and all these layers will cause some diffraction. This will be a worse scenario than having a thin diffracting layer on the surface of a diffuser or a Plexiglas. This should imply a more difficult job identifying the position of the interference pattern.

5 Holography experiments on the tank system

5.1 Tank parameters

A closed-loop system consisting of three connected tanks and a chemical pump was assembled, as sketched in Figure 63. The basic principle is to use the upper tank with a large surface area to provide continuous flow at an almost equal flow ratio. The chemical pump could have maintained a continuous flow, but we were worried that it would introduce vibrations that would affect the holographic experiments. The upper tank is positioned approximately 3,5 meter higher than the lower reservoir. Teflon coated pipes connect these two tanks to an intermediate inspection tank with glass walls. By opening one or more ball valves after the inspection tank, gravity will press the fluid through the inspection area and affect the particles resting inside. The experiment would stop when the upper reservoir tank is nearly depleted to prevent gas bubbles from entering the flow (yields more turbulence). The chemical pump would be applied to fill the upper reservoir.
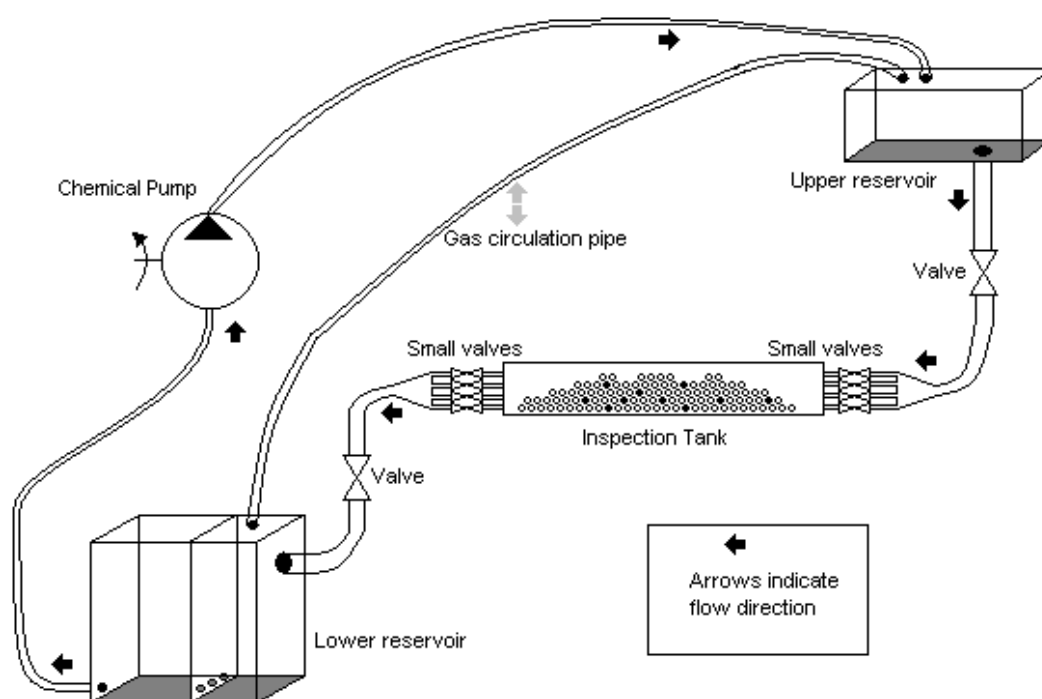

Figure 63 Sketch of our tank system.

We would experiment with a reduced flow in the closed-loop system. The system had proved not to be airtight when these experiments were performed. This limited the amount of time in which tests could be carried out due to increased crystallization and gas leakage. The gas leakage, although small, made it impossible to use the 10 l of Cyclohexanon solvent. Cyclohexanon is the most dangerous solvent of the two fluids. To use it in the tanks when these proved not to be airtight would be a serious health risk, and the experiments could only have been performed within a few days before all the fluid had to be removed. It was therefore decided only to use the 20 l of Benzaldehyde, as this allowed us to do experiments for several weeks before crystallization would become a problem. This represented an index matching of 1,51 for the glass particles to 1,54 of the solvent. This would give rise to more diffraction

from the particles. The yellow laser would not be used. It has too weak intensity to record holograms with the BR film. It was tested in the following set-up, without producing holograms.

A lot of time and effort was put in to make the system as airtight as it eventually became. The tanks had been built of glass in order to observe the fluid levels and special considerations had to be taken in choosing adequate pipes and silicone to bind it all together. The solvent had impressed us with its capabilities of resolving most of our early solutions, hence demanding a lot more work to be done than anticipated. The skilled people in the workshop here at the Department of Physics and Technology executed this work with guidance from the student studying Process Technology. Of the two available glass sections containing the particles, the one with 2cm in inner width was chosen. The reason for choosing the largest inner diameter was to improve the results for the student who would study the upper layer with a high-speed video camera. A larger inner width implies a larger diffractive particle mass. Ten particles would then lie next to each other between the glass walls of the inspection tank. The inspection tank, upper and lower fluid tanks and the pipes with ball valves are displayed in the Figure 64 and Figure 65.
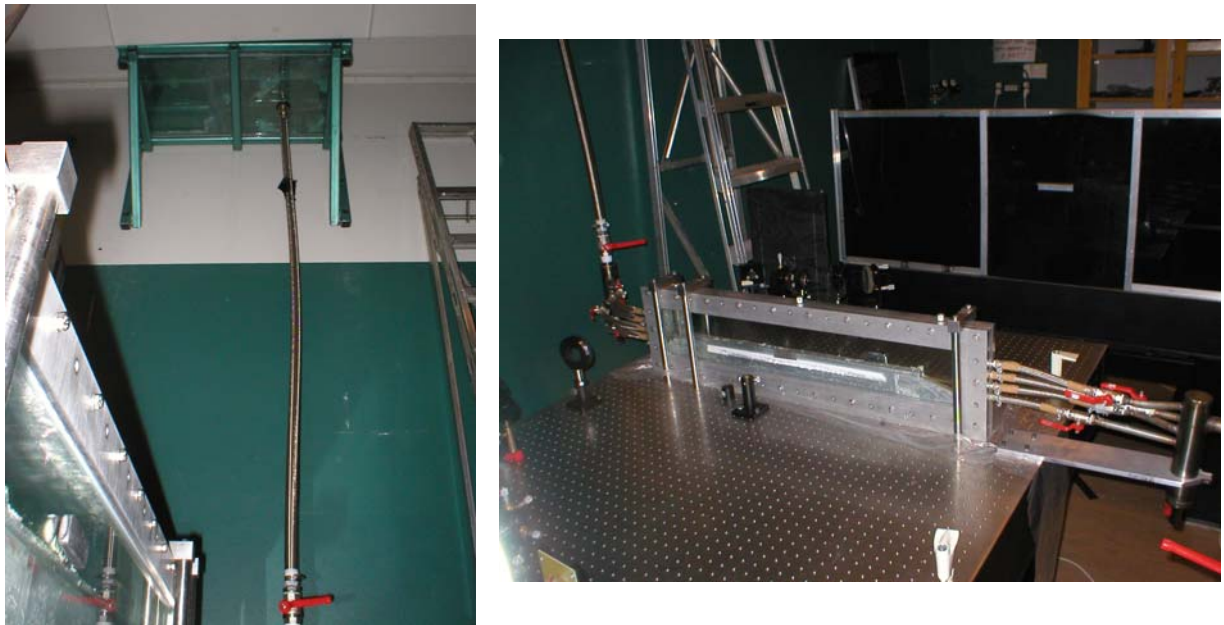
Figure 64 Two pictures of the tank system. The left show the upper tank which provides the pressure. The picture to the right shows the inspection tank mounted on the optical table. Note the four ball valves at the outlets of the inspection tank. One of these is used in the later experiments.
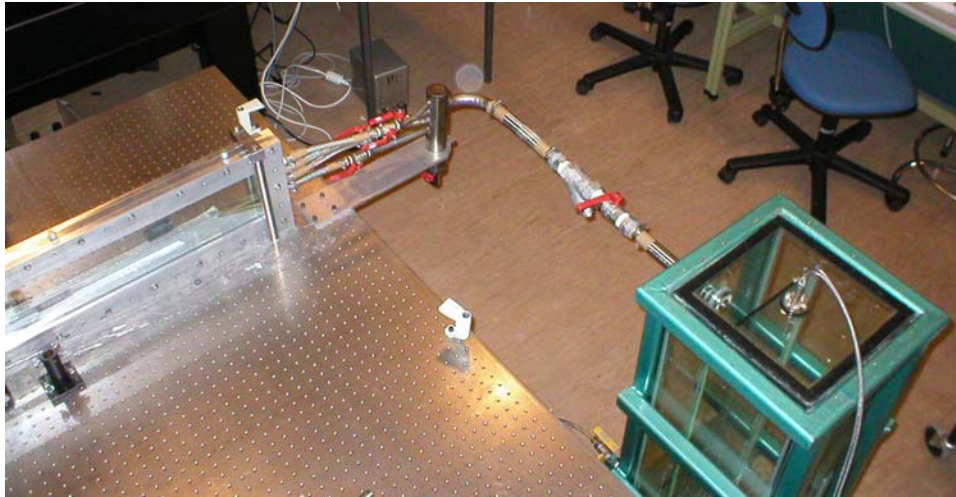
Figure 65 The inspection tank and the lower reservoir tank. The fluid was pumped back to the upper reservoir after each real-time test.

5.1.1 Flow conditions

The inspection tank has been supplied with numerous ball valves to control the inlet and outlet. To provide a less turbulent flow profile inside the inspection tank, the pipeline from the upper tank goes into four smaller pipes, each with its own ball valve. A metal bar with a mesh of 2 mm holes is positioned straight after the inspection inlet to further remove turbulent fluid behavior. The outlet from the inspection tank also has four flow pipes with valves. These valves will be the only way to adjust the flow rate. An electrical pump designed for chemical purposes has been provided by Delta Pumpefabrikk. We used it to pump the fluid from the lower tank back to the upper reservoir tank after each test run. At the present time no method has been implemented for flow rate read-out. These values will therefore be estimates, based on measuring the difference in tank levels during a time interval. This poses no problem for the holography experiments, but we lack exact reference information of the conditions we have collected holographic information about. The project should include equipment for measuring the exact flow rate at a later stage if qualitative information is desired. Only one of the small ball valves will be used for the holography experiments. The flow rate will range from closed valve to full open. A robust estimate for the flow through the tank with a complete open valve is;

Inner *cross section* of the inspection tank is approximately,
$$\mathbf{A_1} = 6,9 \text{ cm} * 2\text{cm} = 13,8 \text{ cm}^2$$
Lower tank area is,
$$\mathbf{A_2} = 29,0 \text{ cm} * 29,5\text{cm} = 855,5 \text{ cm}^2$$
Change in tank volume is,
$$\mathbf{\Delta V} = 855,5 \text{ cm}^2 * (6,3 \text{ cm} - 0,3 \text{ cm}) = 5133,0 \text{ cm}^3$$
A <u>measured</u> estimate of *volume flow*,
$$\mathbf{\Delta V/t} \sim 5133,0 \text{ cm}^3 / 19,5 \text{ s} \approx 263,2 \text{ cm}^3/\text{s}$$
An estimate for the maximum *speed of fluid* through tank
$$\mathbf{v} \sim 263,2 \text{ cm}^3/\text{s} / 13,8 \text{ cm}^2 \approx 19,1 \text{ cm/s}$$
An estimate for the maximum *flow*,
$$\mathbf{F} \sim 263 \text{ cm}^3/\text{s} * 60 \text{ s/min} / 1000 \text{ l/cm}^3 \approx 15,8 \text{ l/min}$$

A real-time holography set-up, shown in Figure 68, would be designed to illuminate through the partly transparent objects in the inspection tank. By recording one hologram of a selection of particles, minute changes in these particle's positions would hopefully be revealed by the second continuous, weak exposure during the flow. These changes would be recorded with a digital video camera. In all experiments the violet diode lamp would be used for erasure purposes, although this is not shown in the set-up. The results of the experiments would be somewhat limited due to the equipment used. This will be further outlined in the discussion section.

5.1.2 Video camera specifications

The maximum resolvable layer movement is partly limited by the camera speed. Earlier experiments with simpler and better objects (diffusers etc.) have shown that one cannot expect to observe more than ~ 200 μm of parallel translation before the interference pattern stops being visible and fringes cannot be separated (depending on setup and observation distance). This can be regarded as an upper limit since the tank would contain ten particles in width, each a source of light diffraction. The camera speed and resolution further define the scale of displacements that can be achieved.

5.1.2.1 Shutter speed

The shutter speed decides how fast the particles can move, while the resolution determines how well the interference pattern can be analyzed. It requires a fast camera or a slow movement to capture a few pictures while the displacement still is in the 0 - 200 μm region. Due to the extremely small resolvable displacement also vibrations might be measured. If one requires 5 frames or more within the total movement (<0,2 mm) to estimate the speed or direction of the mass, a simple formula to describe the system can be:

$$\text{Max. resolvable mass speed} = \frac{\text{shutter speed [frames/s]} * \text{max. observable movement [m]}}{\text{needed frames (per total observable movement) [frames]}} \quad (5\text{-}1)$$

An example using 30 frames per second (fps), with 5 frames during the movement and 200 μm maximum displacement yields:

$$\text{Max. resolvable mass speed} = \frac{30\,[\text{frames/s}] * 200 * 10^{-6}\,[\text{m}]}{5\,[\text{frames}]} = 1,2\left[\frac{mm}{s}\right]$$

A digital video camera for home entertainment normally has 25 fps. Clearly a faster frame rate would be appreciated. The particles under investigation will never travel faster than the fluid, but to achieve sand dune transportation the particles might require a strong flow. The particles must overcome friction and gravity to slip into the flow. Nevertheless, the resolvable speed, which lies in the [mm/s] region, indicates that a slow fluid acceleration should be used. As this may pose a problem due to the robust valve system, a faster camera than the regular 25 fps was wanted. It should also be noted that if there exist lower particle layers that move while the top layer is in a sand-dune transportation regime, it would not necessarily be a linear movement. A short motion pulse would be hard to detect and to analyze with our real-time set-up.

5.1.2.2   Camera resolution

Quality of the analysis depends on the camera resolution. The shutter speed and the resolution is a trade-off. In contrast to using a standard video camera, various types that are directly connected to a computer can support faster frame rates and better resolution. These are without a hard drive and store all recorded information on the pc. Whether the connection is a USB or firewire, depends solely on the video camera manufacturer. Most scientific video cameras support only one of these connections. Although the USB 2.0 standard has caught up with the firewire transmission rate (>400 Mbps, theoretical limit [http://www.macspeedzone.com, 18.06.04]), most scientific cameras use firewire connections. High-speed digital cameras (~1000 fps) offer an incredible amount of images with good resolution, but require good lighting conditions. We were permitted to borrow a high-speed digital video camera from the Process Technology Section at our department, but before it could be tested it was stolen. A webcam turned out to be the best available option, as the project did not have an alternative to the high-speed camera. The resolution was very low at the maximum shutter speed, but the webcam was very easy to use and had a maximum shutter speed at 60 fps. The specifications was:

Philips USB (1.0) PC-camera	TOUcam Pro
Model	PCVC740K
Maximum shutter speed	60fps at 320*240 (SIF)
Maximum resolution (video)	30fps at 640*480 (VGA)
Sensor	CCD
Required illumination	<1 lux (only for slow frame rates / still image)

If the hologram is of poor quality then the video resolution may not do much of a difference, but hopefully this would not be the case. The angles of the two beams to the normal of the film (reference angle ~ 51°, object angle ~ 0°), imply a hologram resolution of ~1300 lines/mm (confer to section 4.2), which should be good enough for our purposes.
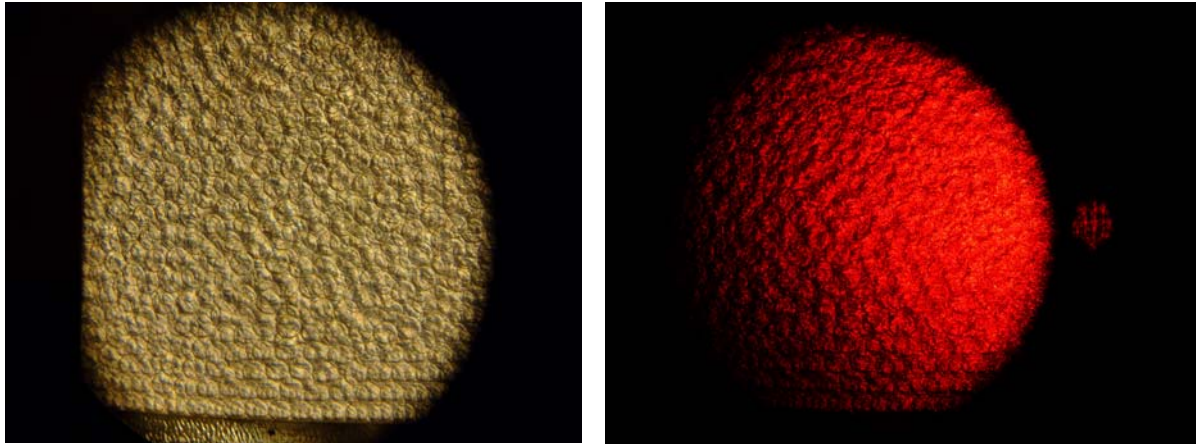

5.2   Video sequences

Two video settings (60 fps and 30 fps) were qualitatively tested using the set-up shown in Figure 68. These were the two fastest frame rates possible. Slower frame rates did not provide better resolution (VGA is the best this webcam can do). Videos are hard to display in an illustrative manner in a printed media, but the following sections will try to shed light on what the videos revealed. Applying a diffuser in front of the particle mass produced no results, as the real-time images showed no interference at all. It was therefore not used in any of the following experiments. A polarizer was used in front of the video camera in all recordings. It was positioned to have the same polarization direction as the laser and helped removing depolarized light. The depolarized light would otherwise be seen as background noise.


5.2.1   Sensitivity of optical table and tank system

Recorded holograms of the particles at rest had good quality. The object under white light condition and illuminated by a reduced object beam is shown in Figure 66. A hologram of a mass of relaxed particles is shown in Figure 67.

Figure 66 The beads and area under observation in the video sequences.The black beads was inserted in the particle mass after these pictures were taken. The image to the left show the particles illuminated by white light and the right image with laser illumination. Both are imaged through the circular BR film holder without the film.
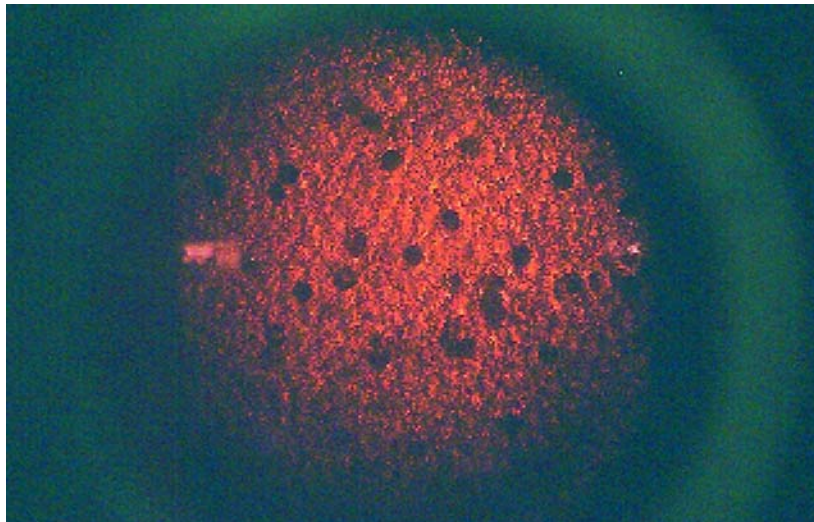
Figure 67 A scanned image from the Philips webcam. The black particles can clearly be seen among the normal transparent glass beads. The hologram is imaged through the film holder.

The recorded real-time image demonstrated an extreme sensitivity to external influence. A simple tap of a finger on the optical table caused the image to jump around and causing parts or the whole object to disappear. This twinkling appear if the path length of the object beam illuminating the live particle mass have changed after the hologram has been recorded. The optical instruments and or the observation tank and its mechanical instability cause the small path length difference. The effect seems to be increased by the rigid pipes connected to the tank, as the blinking took several seconds to die out. The flow pipes, shown in Figure 64 and Figure 65 are likely to keep the table in vibration when it is first touched. In all real-time tests the set-up proved to be affected by external influence. A few images from a video showing the change in the real-time interference pattern when the small ball valve is opened are showed in the following section.

5.2.2 Ball valve turned from shut to complete open

This test was performed to check if the opening of a ball valve would affect the holographic system. There would be <u>no flow</u> in the closed loop system, as one of the two main valves was closed. The small valve was turned to a complete open in 30 seconds, with a video frame rate of 60 fps. A selection of images from these videos has been displayed in Figure 69 through Figure 71. The equipment and parameters used in all the real-time experiments were:

Laser: He-Ne at 632,8 nm

<u>Reference</u> beam: Measured irradiance in holder: $\approx$ 151 lux

                            Measured intensity at microscope objective: $\approx$ 596 µW

                            Intensity at the BR emulsion, subtracting surface losses:

$$I_R \approx 596\mu W * \underbrace{0,96^2}_{Col\lim ator} * \underbrace{\frac{0,700}{0,843}}_{Mirror} * \underbrace{\frac{0,514}{0,700}}_{Mirror} * \underbrace{0,96}_{filmfront} \approx 322\mu W$$

                            Illuminating the film holder of diameter: $\approx$ 2,5 cm (A $\approx$ 4,9 cm^2)

                            I/A: $\approx$ 66 µW/cm^2

                            Reference beam angle to the normal of film: $\theta_{ref} \approx 54°$

<u>Object</u> beam: Measured irradiance in holder: $\approx$ 107 lux

                              Estimated I/A: $\approx$ 46 µW/cm^2

Object beam angle to the normal of film: $\theta_{obj} \approx 0°$

Ref./Obj. irradiance: 1,5 : 1

Plano-convex lens: Focal length ~ 19 cm (unknown product)

Holographic Film: Bacteriorodopsin Film (MIB)

Exposure time: ~ 15 sec

Erasure time: ~ 30 sec
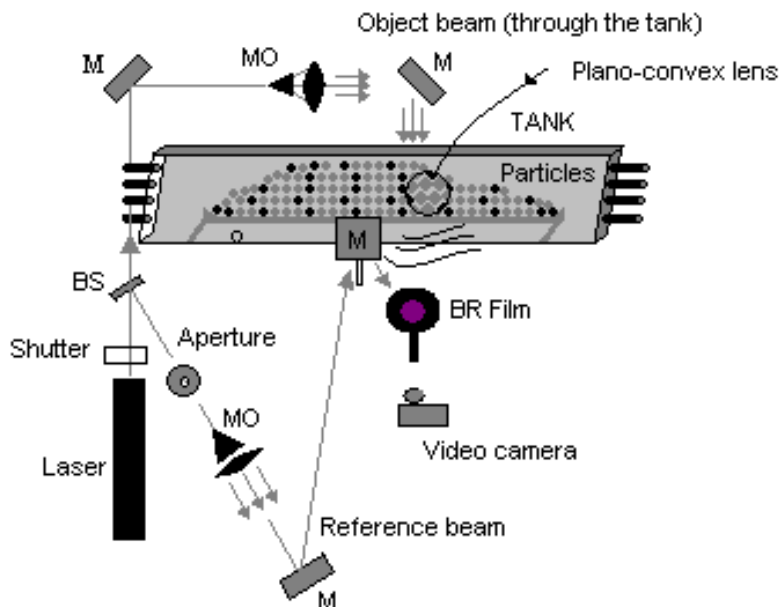
The real-time set-up was as shown in Figure 68.

Figure 68 Set-up used in real-time experiments with particles in an index matched fluid flow.

Comments to the set-up

It is important to note that this set-up produces a <u>transmission hologram</u> of the particles as both object and reference wave illuminates the BR film from the same side. All previous recordings with the BR film have also been transmission holograms (confer with Figure 25, Figure 38, Figure 44 etc.). Reflection holograms can not be adequately produced due to the high optical density of the film and the low intensity lasers available for the project. Reflection set-ups were tested but produced no viewable holograms. This lack of holographic image is due to the small amount of interference recorded in the emulsion. The reason that we wanted to make reflection holograms instead of transmission holograms is that the former recording setup would have made it possible to position the film much closer to the particles. The reference wave would have hit the film from the same side as the video camera. Our video camera is without a zooming feature and all our videos will therefore be at some distance from the particles under investigation. Figure 68 illustrates that we use one plano-convex lens in front of the particles under investigation. Although the lens magnifies the particle area, we would not take advantage of using more than one. Only one lens will be used due to available space between film and the inspection tank and to not reduce the viewing angle.

After the first recorded hologram, the object beam was reduced by gray filters to ~0,8 % and then continued to illuminate the particle area. This reduction made the virtual object equally bright to the "live" illuminated object. This enhances the contrast of the interference fringes.
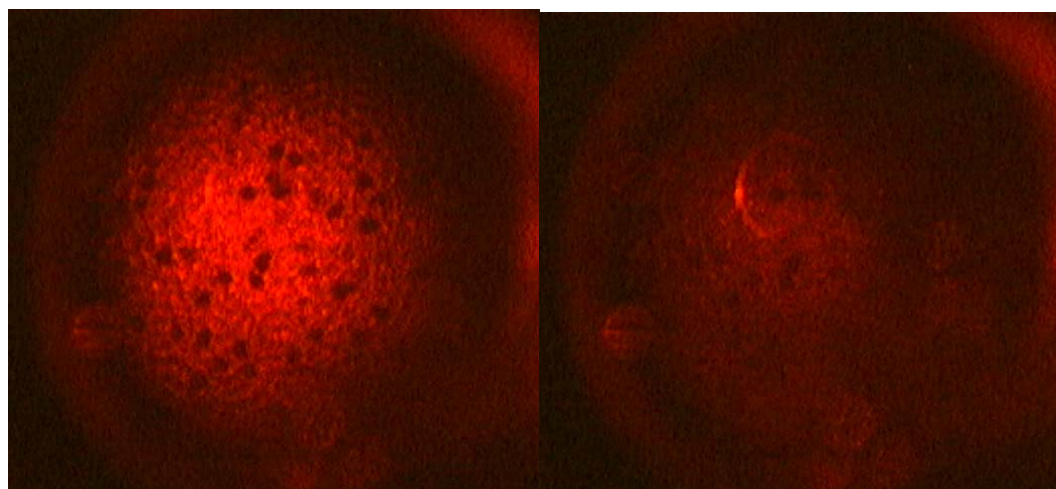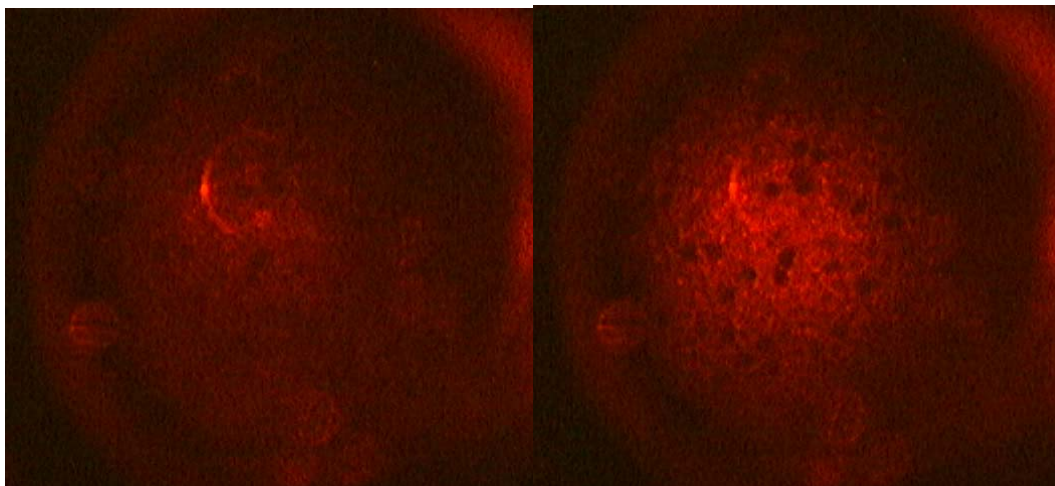

Figure 69 Left image is the interferogram at 4,38 seconds, right image is after 7,68sec.
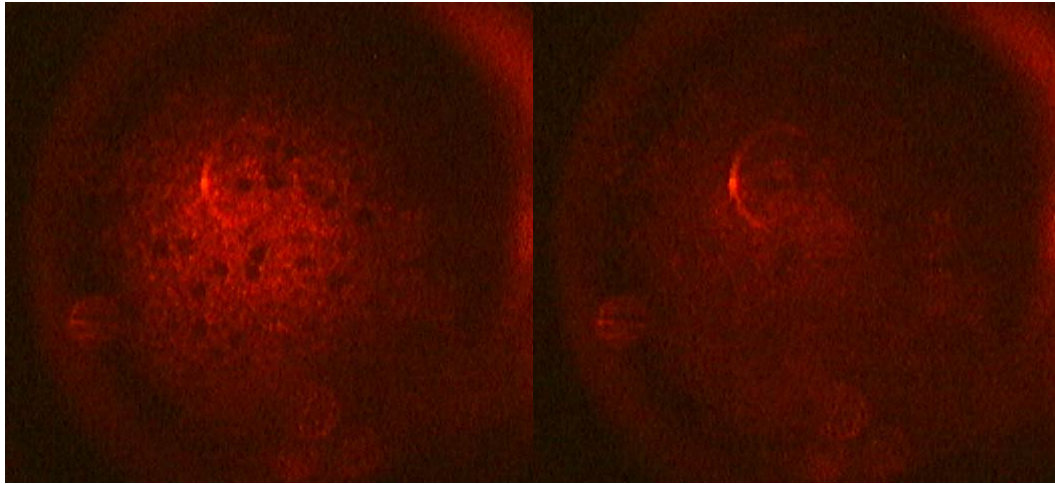
Figure 70 Left image is the interferogram at 11,05 seconds, right image is at 11,07sec.

Figure 71   Left image is the interferogram at 11,57 seconds, right image is at 11,58 sec.

Discussion

These images have been chosen to illustrate how the objects in the real-time system disappeared and re-appeared during the process of opening the ball valve. The effects are similar to those we observed from setting the table slightly in motion by touching it. A tilt appears to be introduced to the tank system by applying a force to the valve handle. The tank may have experienced a small displacement, which would also displace the particle mass inside the tank. Both a displacement of the glass walls and the particle displacement will produce a phase shift in the live object wave.

During the first few seconds of the video the particles appeared very bright, as seen in left image in Figure 69. No blinking appeared until the valve was gently turned open. This turning was continued approximately for the next 30 seconds until the valve was completely open. The blinking started immediately when touching the valve. What can be seen is an increasing amount of twinkling as a stronger force is applied to overcome valve friction and start the turning. The real time image change intensity very rapidly. Notice how the particles change in brightness from not being present to being a bright object in just 0,01 seconds as shown in Figure 71.

The "blinking" of the real time image indicated that the live object wave had experienced a phase shift. This phase shift difference must be half a wavelength to

fully subtract the object information from the recorded hologram in the BR film, but a less phase difference will produce a weak image instead of a full cancellation. Notice the image of the circular metal film holder reflected in the glass wall of the tank in Figure 70 (right image). This reflection will also be recorded in the original hologram. The change in optical path length for this reflection will be different than for the particles. Therefore a combination of the live reflection and the recorded reflection is displayed although the rest of the particles have disappeared.

The mentioned phase shift arises from an optical path length difference. If this path length difference is either plus or minus half a wavelength, which implies a 180° phase difference, a black image will appear. The waves will then perfectly cancel out. 0 ° phase difference yield the brightest image as the waves add.

The system sensitivity to the opening of the ball valve was unfortunate. This would introduce a large amount of noise to the later experiments. Phase changes were expected to provide useful information of particles that have changed their positions. To avoid this valve-introduced noise in later experiments, the valve would be turned slower than in these experiments, although this was subject to individual performance. This precaution never removed the image noise resulting from the opening of the ball valve.

5.2.3 Flow experiments

The real-time holographic set-up worked as it was designed to do. The system was however very sensitive to external influence. Our optical equipment is constructed to be extremely stable if it is left to settle. The table is a TMC model hovering on compressed Nitrogen gas to avoid any kind of vibrations from the ground. All optical components are quality Melles Griot or Edmund Optics products. The problem with our tank system is that we are applying mechanical vibrations and torque directly to the object under investigation, which is attached to the optical table. As the upper tank is fastened to the wall and the lower tank has not been fully isolated from the cement floor our optical set-up can pick up vibrations in the house. The flow itself will also add vibrations. It was shown in the previous section that the opening of one ball valve affects the real-time results. This was the most severe problem. We did not try to redesign the tank system to avoid these problems. This had to do with available time and money.

5.2.3.1   Image acquisition from the video sequences

The following sections will show a number of images extracted from the captured video sequences with flow in the tank system. The quality of these images is debatable. They have not been edited in any photo editor, although this approach has been tested. Adobe Photoshop support subtracting, multiplying, adding, differencing, excluding two images and many more functions. The resulting images were either not improved or just slightly better than the original images. Hence the originals are used in this thesis. They were extracted from the .*avi* video format provided by the Philips Webcam to .*bmp* format using *VirtualDub 1.3d*, free video software.

The objective in the interferometric set-up was to find and track interference patterns in the object scene. The acquired images showed a lot of interference between the virtual and the live object. The aforementioned blinking, affected the video information, but special interference fringes appeared during the flow. These could be identified when investigating the film sequences in a video editor, but proved difficult to identify from extracted images. Our eye is a very sensitive tool and is extremely good at detecting a brightness change of an object in a video sequence. According to [http://hyperphysics.phy-astr.gsu.edu/hbase/vision/rodcone.html, 07.09.04] it is the rods in the human eye that are responsible for our dark vision. These photoreceptors are situated mostly in the eye's peripheral areas. It is also very interesting to note that they "employ a sensitive photopigment called rhodopsin", similar to the applied real time film. Our visual resolution is better with the eye's cones, mostly situated in the fovea centralis, but the rods are far better motion sensors as they are much more light sensitive. It is the sensitivity of the rods that make the human eye so good at detecting brightness variations in a video sequence. We have more problems identifying a frozen fringe in a low resolution picture. The dark moving fringes were often large, covering the entire view. As the edges were indefinite the exact position of one fringe was hard to specify. The fringes moved in the upward direction in the sequences as the flow increased, but they also had a slightly wavelike up and down movement. The following pictures have been marked with a white partition and an arrow to indicate were we know a dark fringe movement was present.

5.2.3.1.1 30 fps image sequence

The left image in Figure 72 is a bright image from one video recording using 30fps and VGA resolution, while the next three pictures are captured some time later showing an interference fringe. The time of each picture is listed to get an idea of the speed of the fringe movement. The valve was slowly opened after approximately 5 seconds from the start of the video. It was fully open after approximately 55 seconds.
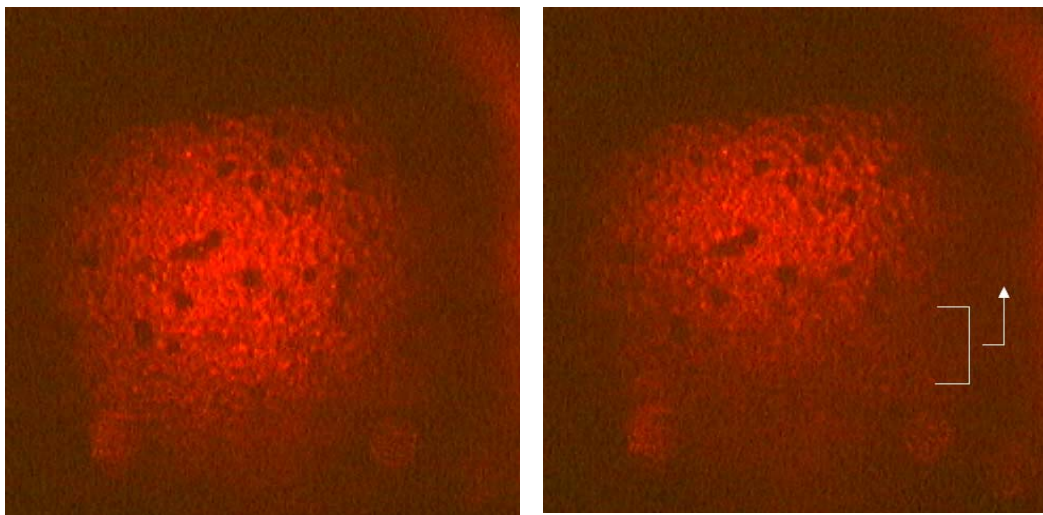
**Figure 72 Two pictures from a 30 fps video sequence. The left image is an early picture at 9,032 seconds which show no fringes, while the picture to the right show a dark fringe moving up from below. The right picture is taken after 32,4 seconds from the start of the video.**
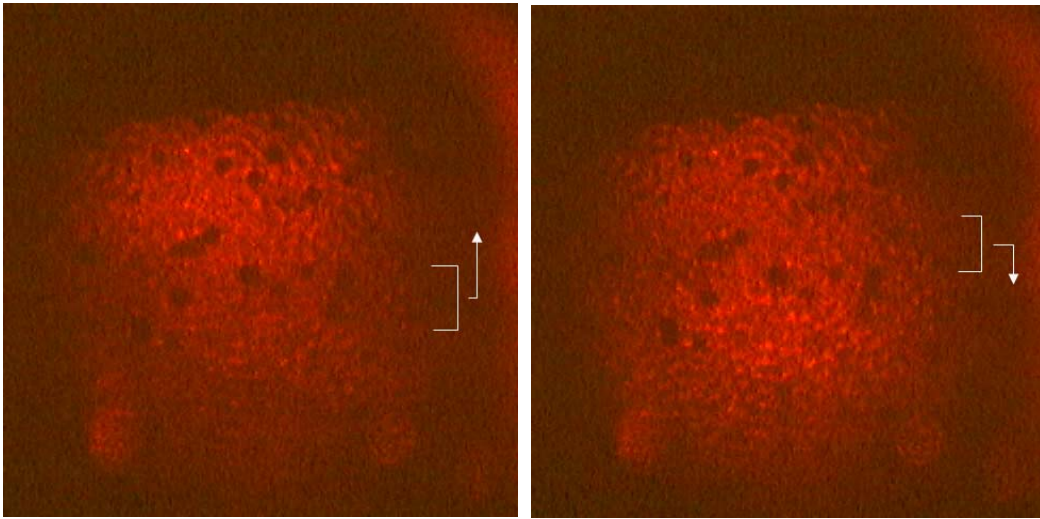
Figure 73 Fringe movement during opening of a small ball valve. Left picture is taken after 32,433 s while the picture to the right is taken after 32,466 s. As marked in the image, the fringe is moving upwards and then turning back down.

5.2.3.1.2   60 fps image sequence

The 60 frames per second setting requires a 320*160 pixels resolution. The first image in Figure 74 shows a bright real-time image where the two object waves have a constructive interference, which makes the object appear bright. All other images are captured successively and show how the interference fringe at the surface of the object is shifted in position. Note that these pictures do not come in evenly sampled time intervals. They have been chosen to best display a fringe pattern that moved slightly up and down within a few seconds.
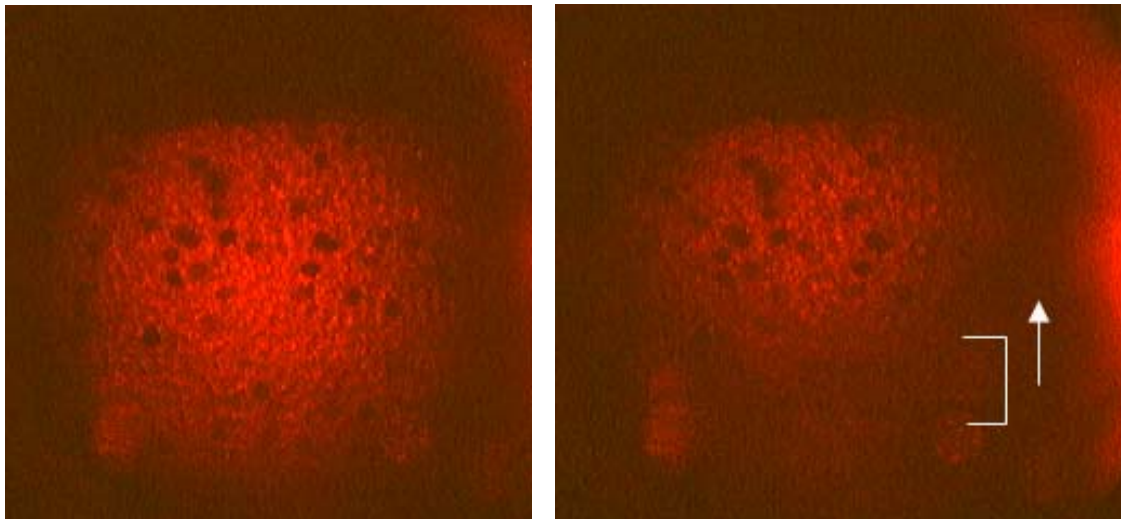
Figure 74 The picture to the right is a bright image before the flow has started at 3,687s. The picture to the right shows an upward moving fringe at 24,334 seconds.
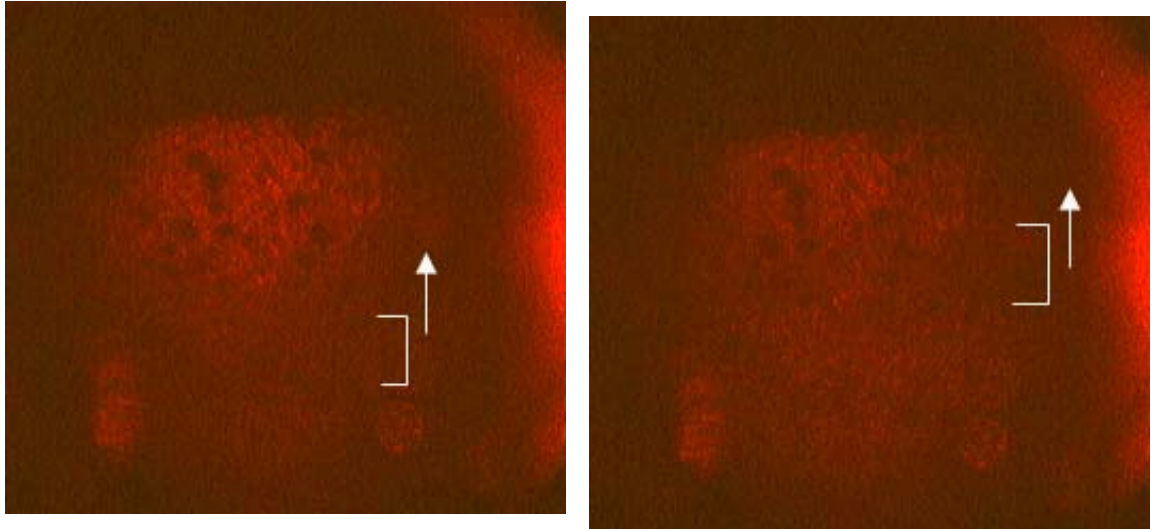
Figure 75 The left picture shows the particles at 24,350 s, and the right picture at 24,384 s. Both images indicate an upward moving fringe.
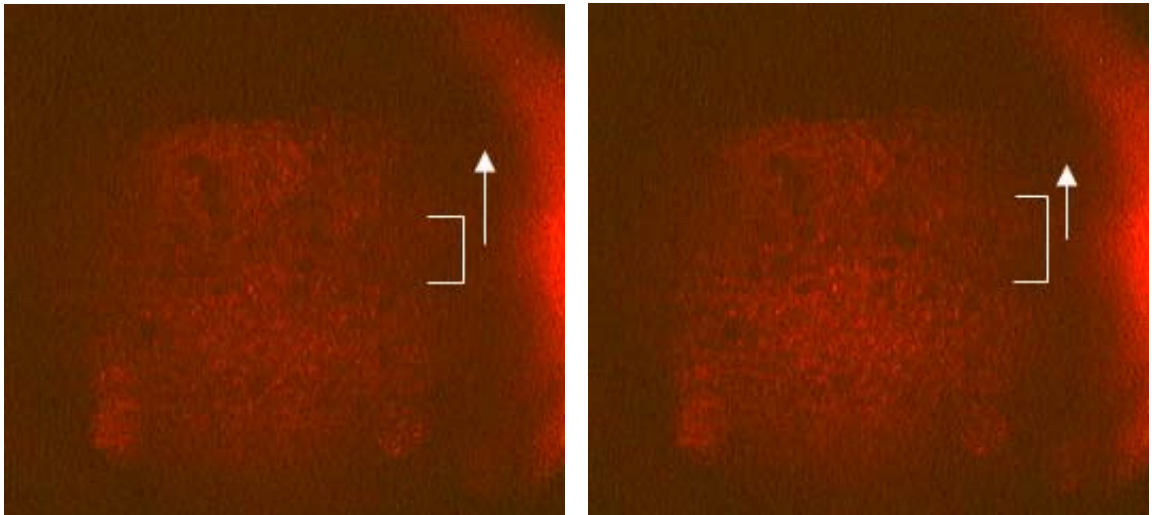
Figure 76 Left image show the fringe at 24,417 s and the right image at 25,284 s.

Figure 77 Left image shows the fringe at 26,484 s and the right image at 26,767 s.

Discussion

It is understood that judging solely from the accuracy of these pictures, the fringe localization can be questioned. These pictures have been compared to a fringe movement in the video sequence. The objective for using real-time holog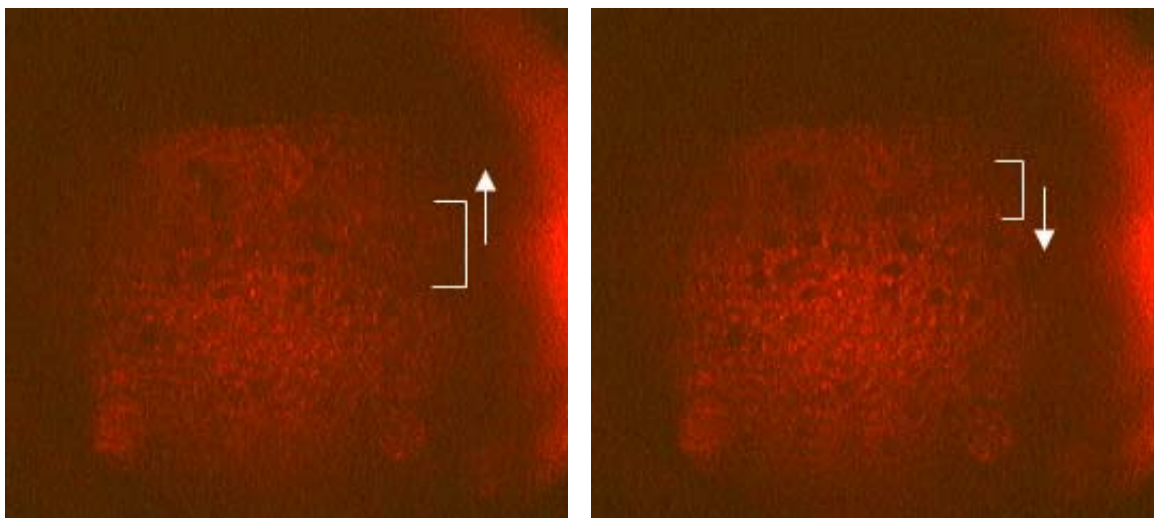raphy was to discover whether there was a particle motion underneath the upper moving sand dune transportation. The problem in all real-time experiments was however that the interference between the live object and the virtual object stopped several seconds before the sand dune transportation begun. This will be further discussed in the next section.

5.3 Evaluation of the results

The most severe problem in the real-time experiments is not shown in any of the previous pictures. The problem can be illustrated with the two pictures in Figure 78. They are without any observable fringe pattern. We can observe particles that have started to move on the top. The optical path length of the illuminated object has changed too much to observe interference fringes, before the particles in the upper layer have started to slip into the flow. When the sand dune conditions are met and the upper beads are moving the holographic system is out of its limits. The interference between the live illuminated object and the virtual object came to an end several seconds before the Benzaldehyde flow was strong enough to move particles in the upper layers. The observable interference patterns ended five to fifteen seconds before the flow was strong enough, depending on how fast the valve was turned open. The valve was approximately ¾ open when the patterns ended. Our main objective was to see how the lower layers were affected during sand dune transportation. This goal was therefore never reached. We did not have the option to move the film closer to the particles. A smaller area under investigation could have revealed more specific information about the nature of the changes that were taking place before the observable interference ended. The reference wave has to hit the film from the same side as the object wave in a transmission set-up, as explained in section 5.2.2, and we were short of a stronger laser to make reflection holograms. Two pictures from the 30 fps video sequence used are shown in Figure 78 to illustrate the particle movement in the upper layer and the lack of fringe pattern in the lower layers.
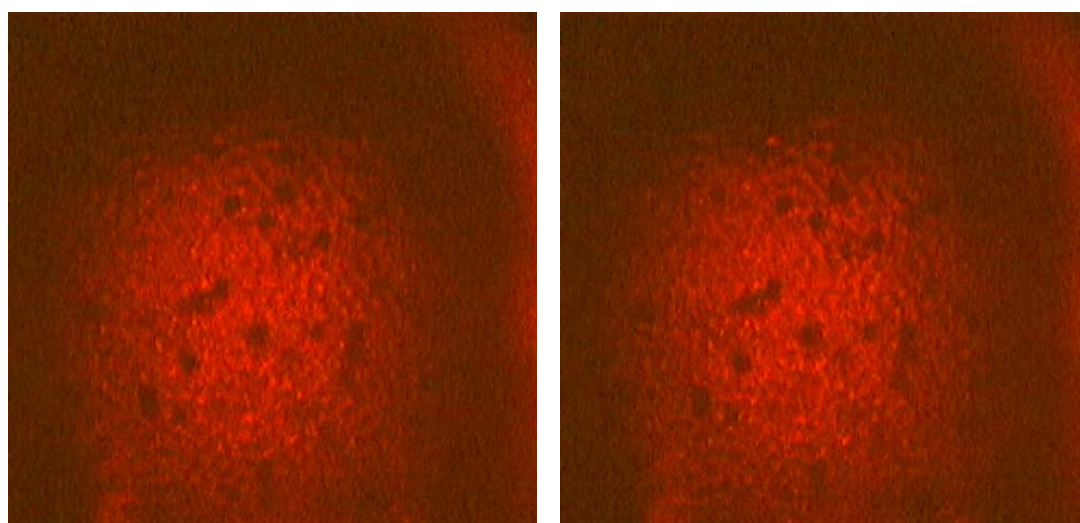
Figure 78 Two pictures from a 30 fps video sequence showing particle transportation at the top layer. The left picture is at 49,533 s and the left picture is at 49,566 s after the start of the video.

The fringe pattern ended at approximately 44 s, while the particles started slipping into the flow at approximately 49 s from the start.

The change in optical path length and thus the disappearance of interference patterns could be the result of the following causes:

- The flow has moved the particle mass too fast for our system to pick it up. This could be due to a strong variation of flow rate (pulse) or a too strong flow rate.
- The change in pressure inside the inspection tank drops when the flow is turned open. This could cause the glass walls of the tank to be compressed or the metal bar that the particles rest on top, to bend and result in the particles being forced to complex movements.
- Vibrations from the flow or torque from the opening of the valve handle have displaced the tank system.
- The virtual object has decreased in intensity and thus removed the possibility of an observable interference pattern. The BR molecules in the film have thermally returned to the ground state and the continuous exposure of the live object has recorded extra noise.

Our real-time holographic technique has showed that it is a method to investigate small displacements, preferably linear movements. In our flow experiments we were hoping to see linear particle mass movement in the horizontal direction resulting in vertical fringes beneath the moving particle layers. Such interference patterns were not observed. We observed horizontal fringes moving in the vertical direction. The horizontal fringes in the video sequences are detected before the particles on the top have started to move. The directions of these fringes indicate a very small change in the optical path length in the vertical direction. We are of the opinion that several of the above arguments affected the real-time system. The interference pattern is likely to disappear due to a combination of changed particle positions and the virtual image fading away. Please refer to section 3.1.2 on how the BR film returns to the M-state. The amount of back-conversion is dependent on both the intensity of the reference wave and the thermal RTR of the film. After 44 seconds a lot of information of the virtual object is lost from thermally back-conversion alone.

The observed horizontal fringe patterns provide useful information about the position of the particle mass. It tells us that there is no horizontal movement up to the point where the interference patterns disappear. Any additional displacement in the horizontal direction would have caused another direction of the fringe pattern. We do not know what happens after 44 seconds in the 30 fps video sequence, but as long as there are the same observable fringes in the horizontal direction we know for certain that nothing has moved along the direction of the flow.

The observed fringes apparently move closer together in the upward direction. This is not determined by the direction of the displacements, but the holographic set-up. This was visually confirmed using the BR film to do observations of a moving ground glass. The fringe distance however, inform us of how much the optical path length has changed. The videos showed that the fringes got closer and closer together as the valve was turned open. This indicates that the change in path length increased with a

stronger flow. The fringes were moving around too much to qualitatively present a number for the optical path difference.

For the purpose of small translations, real time holography is probably one of the most accurate and non-invasive techniques available. As derived in section 2.4.3, a horizontal change in particle position results in a vertical fringe pattern. It is also shown that a displacement in the vertical direction results in horizontal fringes. Experiments with this type of displacement have not been tested in our laboratory, as we do not possess the necessary equipment for µm translation in the vertical direction. In addition to vertical displacement a rotation around the horizontal plane (around the *y*-axis in Figure 15) also results in a vertical fringe pattern [Ostrovsky et al. 1990]. It is not likely that our inspection tank experiences a rotation during the flow experiments, as we did not observe any vertical fringes during the ball valve tests. It is unlikely that the flow introduced a torque to and hence rotated the inspection tank, although we do not exclude anything.

After these tests had been carried out we had a second look at the construction of the disassembled inspection tank. The glass walls were only suspended on one side by 0,5-1 mm of silicone to the outer two frames. The other side of each glass wall faces the inside of the tank and the particles rest against these sides. The outer metal frames are fastened with bolts towards a center metal frame, disjoined by a rubber strip to secure the system from leakage. A pressure change inside the tank could therefore alter the separation distance between the walls. The glass walls are partly "free" to move. This could support a theory of the walls being compressed as the flow increase. A change in distance between the glass walls could provoke a random particle consolidation inside the tank and remove the possibility of real-time interference. An increasing flow rate could also gradually change the position and the inclination of the walls. This would change the optical path length of the object wave through the inspection tank.

The image sequences captured on film during these tests show one perspective of the real-time image. Instead of just using one perspective we could have applied several video cameras to improve our information of the changes at the object plane. Images from many different angles could have been recorded and correlated in a later analysis. For our feasibility study one recording angle was enough to test if the holography approach was applicable to the problem.

6 Conclusion

The experiments carried out during this thesis work have familiarized us to holography and many of its applications. The study of optical holography has been expanded to comprise holographic interferometry. Digital holography has also been investigated. This is a promising technique, but due to the limited time available it was not further pursued in this project.

The main objective has been to visualize particle movement in an index-matched fluid. With this motivation the project originally suggested the use of double-exposure holography. Instead of using this technique together with silver halide holographic films we decided to go for a more dynamic approach. The use of real-time holography allowed us to continuously investigate an object, compared to a double exposure hologram, which only contains information of two discrete states. Real-time holography has never been tested at the Department of Physics and Technology before, and introduced the challenge of finding a suitable holographic recording medium.

The chosen Bacteriorhodopsin film has proven to be a much more sophisticated holographic film than our silver halide films. Silver halide films have been used at our department during the last decades and require processing in a dark room. The BR film has made our optical work easier and a lot more effective. It had not been used at the department before and needed characterization prior to its use in holographic set-ups. A lamp emitting in the violet part of the visible spectrum of light to erase recorded holograms in the holographic emulsion has been designed. The only encountered problem using the BR film has been the need for a strong laser. Without a powerful laser we could not exploit the maximum diffraction efficiency the film offered, but we could still make transmission holograms of good quality.

We experienced substantial problems with the building of airtight tanks and pipes that were resistant to the Benzaldehyde and the Cyclohexanon solvents. The final system proved to endure the chemicals but it did not become completely airtight. Due to health risks involved with handling of the Cyclohexanon solvent we only applied Benzaldehyde in the tank system. The index matching property of our fluid was therefore slightly worsened, reducing our perception depth and increasing scattering of light in the medium.

The inspection tank mounted on the optical table was likely to introduce vibrations through the pipes and had mechanical instabilities. Especially, controlling the flow was an issue. Opening the ball valve affected the optical table and was not optimal for a holographic system. We further acknowledge that the glass walls should have been fastened directly to the outer metal frames, instead of supporting them in silicone. Due to problems with Benzaldehyde crystallization and leakage we did not have adequately experimental time available to redesign the inspection tank to remove this potential problem.

Visualizing particles in an index matched fluid to reveal movement in the lower layers during sand dune transportation was not successful. It is not even obvious that any such motion exist. The holographic information stopped before the sand dune transportation begun. It is our opinion that this was caused by a change in particle

positions and a displacement of the glass walls. If the particle displacements occurred in a random manner, due to consolidation, it would have been very hard to detect the change by holographic methods. To visualize such a chaotic displacement we would have needed to focus at a few particles and visualized them as an isolated system. This would require a stronger laser and a video camera with better resolution and zoom.

If the lower particle mass under investigation had moved as a layer along the direction of flow, we believe that our holographic system would have detected it. The flow system was too mechanically coarse to qualitatively apply in a holographic system. We did not manage to bridge the gap between the crude flow system and the holographic system sensitive to displacement at the wavelength range.

References

Abrahamson Nils (1981). The Making and Evaluation of Holograms.

Adam M., Kreis T. and Juptner W. (1999). Particle measurement with digital holography. Proceedings Spie, p.3823.

Biedermann K. (1977). Holographic Recording Materials. Topics in applied Physics Vol.20 (p.23).

Blom Kjartan (2002). Experimental methods in color holography. Master thesis at Physics Inzstitute, Bergen University.

Board on Army Science and Technology (2001). Opportunities in Biotechnology for Future Army Applications. Electronically published by The National Academies Press (NAP) at [http://www.nap.edu/books/0309075556/html/] 2004-04-14.

Born M. and Wolf E. (1999). Principles of Optics.

Bouevitch O. and Lewis A. (1995). Autocorrelating femtosecond pulses with thin Bacteriorhodopsin films. Optics Communications, 116, pp.170-174.

Downie J. D. and Smithey Daniel T. (1996). Measurements of holographic properties of Bacteriorhodopsin films. Applied Optics, Vol.35 (29), pp.5780-5789.

Dubois F., Joannes L., Dupont O., Dewandel J.L. and Logros J.C. (1999). An integrated optical set-up for fluid-physics experiments under microgravity conditions. Meas. Sci. technology, 10, pp. 934-945.

Hampp Norbert (2000). Bacteriorhodopsin as a Photochromic Retinal Protein for Optical Memories. Chem. Rev., 100, pp.1755-1776.

Hariaharan P. (1996). Optical Holography. Principles, techniques and applications. Sec Edition (p.15).

Haussman G. and Lauterborn W. (1980). Determination of size and position of fast moving gas bubbles in liquids by digital 3-D image processing of hologram reconstruction. Applied Optics, Vol.19 (20), pp.3529-3535.

Hecht Norman L (1972). Investigation of holographic interferometry for displacement measurements. Ph.D. Thesis, Alfred University, Alfred, NY.

Hecht Norman L., Minardi J. E., Lewis D. and Fusek R. L. (1973). Quantitative theory for predicting fringe pattern formation in holographic interferometry. Applied Optics, Vol.12 (11), pp.2665-2676.

Hossack Will (2003). Physics 4/5 Modern Optics, Topic 9 "Holographic Interferometry". Applied Optics Group at the Department of Physics and Astronomy, University of Edinburgh. [http://www.ph.ed.ac.uk/~wjh/teaching/mo/, 20.04.04]

Jaising H. Y. (1998). Experimental Methods in Holographic Interferometry. Master thesis at the Department of Physics and Technology, Bergen University.

Kasap S.O. (2001). Optoelectronics and Photonics. Principles and Practices.

Kebbel V., Hartman H-J. and Juptner W. (2001). Application of digital holographic microscopy for inspection of micro-optical components. Proceedings Spie, 4398, pp.189-98.

Konrad M.A., Yaroslavski L.P. and Merzlyakov N.S. (1972). Computer synthesis of transparency holograms. Sov. Phys.-Tech Phys., 17, pp.329-32.

Lie Roger (in preparation). Master thesis at the Department of Physics and Technology, Bergen University.

Lin L. H. and Beauchamp L. H. (1970). Write-read-erase in situ optical memory using thermoplastic holograms. Applied Optics, 9, pp. 2088-2092.

Meyerhofer D. (1977). Holographic Recording Materials Topics in applied Physics Vol.20 (p.75).

Osten W., Seebacher S., Baumbach T. and Juptner W. (2001). Absolute shape control of microcomponents using digital holography and multiwavelength contouring. Proceedings Spie, 4275, pp.71-84.

Ostrovsky, Y.I., Schchepinov V.P. and Yakovlev V.V. (1990). Holographic Interferometry in Experimental Mechanics. Springer Series in Optical Sciences Vol.60 (fig.1.5).

Rivkin M. and Shreiber I. (1999). Model for dune formation and propagation in tubes. Two-phase Flow Modelling and Experimentation 1999, Celata, G.P.I, Di Marco, P., and Shah, R.H. (eds), Edizioni ETS, Pisa.

Schnars and Juptner (1994a). Digital recording and reconstruction of holograms in interferometry and shearography. Applied Optics, 33, pp. 4373-4377.

Schnars and Juptner (1994b). Direct phase determination in hologram interferometry with use of digitally recorded holograms. Journal of Opt Soc. Am A., 11, pp.2011-2015.

Schnars Ulf and Juptner Werner P.O. (2002). Digital recording and numerical reconstruction of holograms. Meas. Sci. Technol., 13, pp.85-101.

Seitz A. and Hampp N. (2000). Kinetic Optimization of Bacteriorhodopsin Films for Holographic Interferometry. J. Phys. Chem. B, 104, pp.7183-7192.

Singstad I. (1996). Klassisk Holografisk teknikk. Scientific/Technical Report Nr. 1996-12 ISSN 0803-2696.

Skarman B. (1994). Digital holography in flow visualization. <u>Final Report for ESAESTEC</u>. Purchase order 32.11.1994, 142722.

Smith H.M. (1977). <u>Holographic Recording Materials.</u> Topics in Applied Physics Vol. 20 (p.3).

Urbach J. C. (1977). <u>Holographic Recording Materials</u>. Topics in Applied Physics Vol.20 (p.179)

Van Deelen, W. & Nisenson, P. (1969). Mirror blank testing using real time holographic interferometry. <u>Applied Optics</u>, 8, pp. 951-955.
Weast R. C. (1985). CRC handbook of chemistry and physics. 66th edition.

Wolperdinger M. (2004). Correspondence with MIB dated 10.02.04.

URL's:
[http://otrc.tamu.edu/Pages/seismicrisk.htm, 18.08.04]
[http://www.chemfinder.cambridgesoft.com, 03.04]
[http://www.edmundoptics.com, 07.06.2004]
[http://www.etgtech.com/products.htm, 01.01.04]
[http://www.hololight.net/medical.html, 22.04.04]
[http://www.holophile.com/about.htm, 20.04.04]
[http://www.holophile.com/history.htm, 18.04.04]
[http://www.holoworld.com/holo/quest6.html, 18.04.04]
[http://www.hyperphysics.phy-astr.gsu.edu/hbase/vision/colcon.html#c1, 10.02.04]
[http://www.ipt.ntnu.no/~jsg/studenter/prosjekt/1995/henriksen.txt, 21.08.04]
[http://www.macspeedzone.com/archive/5.0/usbcomparison.html, 18.06.04]
[http://www.ph.ed.ac.uk/~wjh/teaching/mo/slides/holo-interferometry/holo-inter.pdf, 20.04.04]
[http://www.photo.net/learn/optics/lensTutorial, by David Jacobson, 02.01.04]
[http://www.rf.no, 27.02.04]
[http://www.slavich.com, 20.04.04]
[http://www.steinbichler.de, 09.01.04]
[http://www.torgersenbil.no/Xenon.pdf, 11.02.04]
[http://www.ulb.ac.be/polytech/mrc/Instruments_Design/FSL_en.html, 10.01.04]
[http://www.undergroundinfo.com/uceditorialarchive/June04/june04particles.pdf, 21.08.04]
[http://home.earthlink.net/~digitalholography/, 11.09.04]